2014

Dual Benefits of Adding Damper Bars in PMSMs for Electrified Vehicles: Improved Machine Dynamics and Simplified Integrated Charging

Xiaomin Lu
University of Windsor

DUAL BENEFITS OF ADDING DAMPER BARS IN PMSMs FOR ELECTRIFIED VEHICLES: IMPROVED MACHINE DYNAMICS AND SIMPLIFIED INTEGRATED CHARGING

by

Xiaomin Lu

A Dissertation
Submitted to the Faculty of Graduate Studies
through the Department of Electrical & Computer Engineering
in Partial Fulfillment of the Requirements for
the Degree of Doctor of Philosophy
at the University of Windsor

Windsor, Ontario, Canada

2014

Dual Benefits of Adding Damper Bars in PMSMs for Electrified Vehicles: Improved Machine Dynamics and Simplified Integrated Charging

by

Xiaomin Lu

APPROVED BY:

_____

J. Jatskevich, External Examiner
University of British Columbia

_____

R. Barron
Department of Mathematics and Statistics

_____

M. Sid-Ahmed
Department of Electrical and Computer Engineering

_____

K. Tepe
Department of Electrical and Computer Engineering

_____

K. Mukherjee, Special Committee Member/Guide
Indian Institute of Engineering Science and Technology, Shibpur, India

_____

N. Kar, Advisor
Department of Electrical and Computer Engineering

July 21st, 2014

DECLARATION OF PREVIOUS PUBLICATIONS

This dissertation includes selected sections of eleven original papers that have been published/submitted for publication in peer reviewed journals and international conferences, as follows:

Dissertation Chapter	Publication title/full citation	Publication status
Chapter 1	N. C. Kar, K.L.V. Iyer, A. Labak, **X. Lu**, C. Lai, A. Balamurali, B. Esteban, and M. Sid-Ahmed, "Courting and Sparking: Wooing Consumers' Interest in the EV Market" *IEEE Electrification Magazine*, vol. 1, pp. 21-31, 2013.	*Published*
Chapter 1	Y. Li, **X. Lu**, and N. C. Kar, "Rule-based Control Strategy with Novel Parameters Optimization Using NSGA-II for Power Split PHEV Operation Cost Minimization," *IEEE Transactions on Vehicular Technology,* 2014.	*Accepted for Publication*
Chapter 2	**X. Lu**, K. L. V. Iyer, K. Mukherjee and N. C. Kar, "A Novel Two-axis Theory based Approach towards Determination of Magnetizing Characteristics of Line Start Permanent Magnet Machine and its Effects on Stability and Starting Performance," *IEEE Transaction on Magnetics*, vol. 49, pp.4733-4737, 2013.	*Published*
Chapter 2	K. L. V. Iyer, **X. Lu**, K. Mukherjee, and N. C. Kar, "Novel Two-Axis Theory based Approach towards Parameter Determination of Line-Start Permanent Magnet Synchronous Machines," *IEEE Transactions on Magnetics*, vol.48, pp. 4208-4211, 2012.	*Published*

Chapter 2	K. Mukherjee, K. L. V. Iyer, **X. Lu**, and N. C. Kar, "A Novel and Fundamental Approach Toward Field and Damper Circuit Parameter Determination of Synchronous Machine," *IEEE Transactions of Industry Applications*, vol. 49, pp. 2097-2105, 2013.	*Published*
Chapter 2	K. Mukherjee, K. L. V. Iyer, **X. Lu**, and N. C. Kar, "A Novel and Fundamental Approach towards Field and Damper Circuit Parameter Determination of Synchronous Machine," in proceedings of *IEEE International Conference on Electric Machines* (ICEM), 2012, France.	*Published*
Chapter 2	Xiaomin Lu; Iyer, K.L.V.; Kar, N.C., "Mathematical modeling and comprehensive analysis of induction assisted permanent magnet synchronous AC motor," *Electric Drives Production Conference (EDPC), 2011 1st International* , vol., no., pp.147,152, 28-29 Sept. 2011	*Published*
Chapter 3	**X. Lu**, K. L. V. Iyer, K. Mukherjee, K. Ramkumar and N. C. Kar, "Investigation of Permanent Magnet Motor Drives Incorporating Damper Bars for Electrified Vehicles" submitted to *IEEE Transactions on Industrial Electronics*, May 2014.	*Submitted*
Chapter 4	**X. Lu**, K. L. V. Iyer, K. Mukherjee, and N. C. Kar, "A Dual Purpose Triangular Neural Network Based Module for Monitoring and Protection in Bi-directional Off-board Level-3 Charging of EV/PHEV," *IEEE Transactions on Smart Grid*, vol.3, pp.1670-1678, 2012.	*Published*
Chapter 4	**X. Lu**, K. L. V. Iyer, K. Mukherjee and N. C. Kar, "Development of a Bi-directional Off-board Level-3 Quick Charging Station for Electric Bus," in proceedings of *IEEE Transportation Electrification Conference and Expo*, 2012, USA.	*Published*

Chapter 4	**X. Lu**, K. L. V. Iyer, K. Mukherjee, and N. C. Kar, "Design and Testing of a Multi-port Sustainable DC Fast Charging Station for EV/PHEV", *IEEE Transactions on Smart Grid*, February 2014.	Submitted

I certify that I have obtained a written permission from the copyright owners to include the above published materials in my dissertation. I certify that the above material describes work completed during my registration as graduate student at the University of Windsor. I certify for the materials that I am one of the co-authors, only sections with my contribution is included.

I certify that, to the best of my knowledge, my dissertation does not infringe upon anyone's copyright nor violate any proprietary rights and that any ideas, techniques, quotations, or any other material from the work of other people included in my dissertation, published or otherwise, are fully acknowledged in accordance with the standard referencing practices. Furthermore, to the extent that I have included copyrighted material that surpasses the bounds of fair dealing within the meaning of the Canada Copyright Act, I certify that I have obtained a written permission from the copyright owner(s) to include such material(s) in my dissertation and have included copies of such copyright clearances to my appendix.

I declare that this is a true copy of my dissertation, including any final revisions, as approved by my dissertation committee and the Graduate Studies office, and that this dissertation has not been submitted for a higher degree to any other University or Institution.

ABSTRACT

Recently, due to rising environmental concerns and predicted future shortages of fossil fuels, there is a movement towards electrification of the transportation industry. A vast majority of the current research uses permanent magnet synchronous machines as the main traction motor in the drivetrain. This work proposes to add a special damper to a conventional permanent magnet synchronous machine to further improve the suitability of this machine for electrified vehicles.

Firstly, an equivalent circuit model is developed to simulate the operation of a conventional PMSM with a damper. A synchronous loading test is proposed to determine the synchronous reactance of the machine. A modified blocked rotor test is used to find the damper parameters assuming that the rotor cage construction is known. Also a single-phase AC test that can be used to determine the damper parameters without prior knowledge of the rotor construction is proposed and presented as an alternative to the blocked rotor test.

Thereafter, the models of a 50 kW traction motor and the same machine with damper bars are developed and simulated. The performance of both machines are compared and evaluated. The damper parameters are selected based on the dynamic and steady state performances. It is also shown that the machine with a damper has faster response to a three-phase short circuit fault.

In addition, this study also looks into integrated charging which utilizes the existing drivetrain components for vehicle to grid and grid to vehicle operation. The damper is shown to be effective in mitigating the saliency condition caused by the buried magnets of IPMSM at stand-still condition. As a result, the machine windings can be used as line inductors for integrated charging.

ACKNOWLEDGEMENTS

I would like to thank my advisor, Dr. Narayan Kar, for accepting me in his program four years ago and providing me full support with kindness, generosity and patience since then. He is the one who guided me into the area of electric machines which I derived great passion upon. He is also the one who taught me how to be a research leader instead of just a student. Thanks to Dr. Kar, I was able to evolve from an immature newly graduated bachelor into a researcher and a leader.

My sincere thanks to Dr. Kaushik Mukherjee, who has guided me in a supervisory role throughout my Ph.D. research. His technical expertise is of great importance to the formulation and development of my work. He helped me through the most difficult time of my study. I am also grateful to him for allowing me to conduct research in his laboratory in India.

I would like to express my gratitude towards Dr. Juri Jatskevich, Dr. Ronald Barron, Dr. Maher Sid-Ahmed and Dr. Kemal Tepe for agreeing to serve on my committee, attending my seminars and defense, and providing valuable suggestions so that I can improve the quality of this dissertation.

I would also like to extend my thanks to Mr. Varaha Iyer for contributing technically towards the findings and assisting me in completing experiments, Mr. Matthew Hurajt and Miss Shruthi Mukundan for proofreading and formatting my dissertation, Miss Himavarsha, and Miss Chunyan Lai for helping me in dissertation formatting.

Last but not least, I would like to thank my family for the unconditional love, support and encouragement.

TABLE OF CONTENTS

DECLARATION OF PREVIOUS PUBLICATIONS ..... **iii**

ABSTRACT ..... **vi**

ACKNOWLEDGEMENTS ..... **vii**

LIST OF TABLES ..... **xi**

LIST OF FIGURES ..... **xii**

NOMENCLATURE ..... **xvi**

Chapter 1 Introduction and Literature Review **1**

1.1 Overview 1

1.2 Electric Machines for EV Application 4

1.2.1 Basic PMSM Configurations 6

1.2.2 Literature Review of PMSM Design for EV Application 8

1.3 Electric Vehicle Charging Infrastructure 10

1.3.1 Introduction to Integrated Charging 11

1.3.2 Literature Review of Integrated Charging for EVs 13

1.4 Motivation for this Dissertation 14

1.5 Dissertation Objective 16

1.6 Dissertation Layout 17

Chapter 2 Equivalent Circuit Modeling **18**

2.1 Introduction 18

2.2 Equivalent Circuit Modeling based on Reference Frame Theory 18

2.2.1 Winding Inductances and Voltage Equations for PMSMs in the abc Frame 19

2.2.2 Fundamentals of Reference Frame Theory 21

2.2.3 dq Equivalent Circuit Model for PMSMs 25

2.2.4 dq Equivalent Circuit Model for Induction Machines 27

2.2.5 Dynamic Model for a PMSM with Damper Bars 29

2.3 Parameter Determination of a PMSM with a Damper 31
2.3.1 DC Test 31
2.3.2 Open Circuit Test 33
2.3.3 Synchronous Speed Loading Test 34
2.3.4 Blocked Rotor Test 39
2.3.5 Single-phase AC Test 41
2.4 Model Verification under Steady State and Free Acceleration Conditions 46
2.5 Performance Prediction and Analysis of a LSPMSM through Numerical Investigations 48
2.6 Study of the Magnetization Characteristics of a LSPMSM 50
2.7 Conclusions 51

Chapter 3 Dynamic and Steady State Performance 52
3.1 Introduction 52
3.2 Motor Drives in Electric Vehicles 53
3.3 Case Study for Illustrating Repeated Overmodulation Operation Periods in an IPMSM Drive 54
3.4 IPMSM Drives for EV Application 55
3.4.1 Modeling of a Three-phase Voltage Source Inverter 55
3.4.2 Experimental Implementation of a Square Wave Inverter Driven LSPMSM 57
3.5 Comparative Analysis of Dynamic and Steady State Performance 59
3.5.1 Investigation of the Effects of Damper Parameters in Dynamic and Steady State Performance 61
3.5.2 Investigation of Dynamic Response with Change in Load Angle 65
3.5.3 Short Circuit Response 67
3.6 Conclusion 68

Chapter 4 Three-phase Integrated Charging 69
4.1 Introduction 69
4.2 Investigation of a Single-phase On-board Battery Charger for an Electric Vehicle 69
4.3 Integrated Charger Using Traction Components 73
4.4 Real-time Control Strategy of the Integrated Charger Converter 77
4.4.1 Bidirectional DC-DC Converter 77
4.4.2 Bidirectional DC-AC/AC-DC Converter 85
4.5 Real-time Simulation of the Three-phase Bidirectional Charger 93
4.6 Conclusion 98

Chapter 5 Conclusions and Suggested Future Work 99
5.1 Conclusions 99
5.2 Suggested Future Work 100

BIBLIOGRAPHY 102

APPENDICES 108
Appendix A Nameplate Rating of the Machines with Damper under Test 108
Appendix B Electrical and Mechanical Characteristics of the EV Studied 109
Appendix C Case Study of the Traction Motor for Toyota Prius 110
Appendix D Machine Equivalent Circuit Parameters 111
Appendix E Permissions for Using Publication 112

VITA AUCTORIS 120

LIST OF TABLES

TABLE 2-1. EXPERIMENT TEST DATA OF DC TEST ON MACHINE I & II.....32

TABLE 2-2. EXPERIMENT TEST DATA OF DC TEST ON MACHINE I AND II.....34

TABLE 2-3. EXPERIMENTAL RESULTS TO OBTAIN D- AND Q-AXIS SYNCHRONOUS INDUCTANCE AT 60 HZ SUPPLY FREQUENCY.....39

TABLE 2-4. EXPERIMENTAL DATA OBTAINED FROM BLOCKED ROTOR TEST ON MACHINE I 40

TABLE 2-5. EXPERIMENTAL RESULTS OBTAINED FROM SINGLE-PHASE AC TEST OF MACHINE II 45

TABLE 3-1. SAMPLE STEADY STATE AND DYNAMIC PERFORMANCE OF THE EXISTING AND PROPOSED MACHINES (STATOR RESISTANCE TO DAMPER RESISTANCE RATIO – 3:2, STATOR LEAKAGE INDUCTANCE TO DAMPER LEAKAGE INDUCTANCE RATIO – 1:1).....60

TABLE 3-2. SAMPLE STEADY STATE AND DYNAMIC PERFORMANCE DATA OF THE PROPOSED MACHINE WITH A DAMPER KEEPING STATOR TO DAMPER RESISTANCE RATIO OF 1:1 AND VARYING THE STATOR TO DAMPER LEAKAGE INDUCTANCE RATIO 60

TABLE 3-3. SAMPLE STEADY STATE AND DYNAMIC PERFORMANCE DATA OF THE PROPOSED MACHINE WITH A DAMPER KEEPING STATOR TO DAMPER LEAKAGE INDUCTANCE RATIO OF 1:5 AND VARYING THE STATOR TO DAMPER RESISTANCE RATIO 60

TABLE A-1. NAMEPLATE RATINGS OF MACHINE I (LSPMSM) 108

TABLE A-2. NAMEPLATE RATINGS OF THE WOUND-FIELD ROTOR SYNCHRONOUS MACHINE WITH DAMPER..... 108

TABLE B-1. VEHICLE OVERALL AND MAJOR POWER COMPONENTS RATINGS 109

TABLE C-1. MECHANICAL AND ELECTRICAL DATA FROM THE PRIUS PERFORMANCE-MAPPING TEST 110

TABLE D-1. PARAMETERS OF THE TOYOTA PRIUS IPMSM WITH DESIGNED DAMPER. 111

LIST OF FIGURES

Figure 1-1. Main drivetrain components and power flow of a pure electric vehicle. 2

Figure 1-2. Main drivetrain components and power flow of hybrid electric vehicles. (a) Series hybrid. (b) Parallel hybrid. (c) Series-parallel hybrid. (d) Complex hybrid. 4

Figure 1-3. Cross-sections of the various traction motor technologies. (a) PMSM. (b) Induction motor. (c) Axial flux SRM. 7

Figure 1-4. PMSM rotor configuration. (a) Surface mount. (b) Interior buried. 7

Figure 1-5. Block diagram of a three-phase battery charger topology and traction motor drive. .12

Figure 1-6. Construction of different machines. (a) Induction machine. (b) PMSM. (c) IPMSM with symmetric damper. 15

Figure 2-1. Schematic of a two-pole, three-phase PMSM with illustration of its conventions. ...20

Figure 2-2. Illustration of the angular relationships for reference frame theory. 21

Figure 2-3. Reference frame conversion. (a) *abc* to arbitrary reference frame. (b) Arbitrary reference frame to *abc*.....22

Figure 2-4. *d*- and *q*-axis equivalent circuit model of a PMSM in the rotor reference frame. (a) *d*-axis. (b) *q*-axis. 26

Figure 2-5. Two-pole, three-phase, wye-connected symmetrical induction machine. 27

Figure 2-6. *d*- and *q*-axis equivalent circuit model of a squirrel cage IM in the rotor reference frame. (a) *d*-axis. (b) *q*-axis. 29

Figure 2-7. Winding schematics of a three-phase PMSM with a damper demonstrating the winding positions, electrical rotor position and the *dq* rotor reference frame. 30

Figure 2-8. *d*-axis and *q*-axis equivalent circuit model of a PMSM with a damper in the rotor reference frame. (a) *d*-axis. (b) *q*-axis. 31

Figure 2-9. Laboratory machines with a damper for parameter estimation experimentation. (a) Machine I: line-start PMSM. (b) Machine II: synchronous machine with a damper. 32

Figure 2-10. Schematic block diagram of the experimental setup for open circuit test. 33

Figure 2-11. Measurement of rotor mechanical speed versus terminal voltage of Machine I and Machine II.....34

Figure 2-12. Schematic block diagram of the experimental setup for synchronous speed loading test.....35

Figure 2-13. Measured voltage, current and position sensor output waveforms captured on an oscilloscope under a specific load at steady state.....35

Figure 2-14. Phasor diagram of a salient pole PMSM. (a) Lagging power factor $\theta>\delta$. (b) Lagging power factor $\theta<\delta$. (c) Leading power factor. 38

Figure 2-15. Measure stator voltage of phase *a* and phase *b*, and current through phase *a*. (a) *d*-axis aligned with *a*, (b) *q*-axis aligned with *a*. 46

Figure 2-16. Calculated and measured stator current waveforms during steady state condition of the machine. 47

Figure 2-17. Calculated and measured stator current waveforms during starting (dynamic) condition of the machine. (a) Calculated. (b) Measured. 47

Figure 2-18. Calculated torque components. (a) Electromagnetic torque. (b) Torque from 'Synchronous' motor action. (c) Torque from 'Induction' motor action. 49

Figure 2-19. Calculated performance of the stator currents (two-axes components) and damper currents (two-axes components. (a) Stator currents. (b) Damper currents. 49

Figure 2-20. Calculated torque, speed and current waveforms from to start to synchronization near rated conditions of the machine with and without incorporating saturation in the machine models. 51

Figure 3-1. Diagram of electric components of an HEV powertrain. 54

Figure 3-2. Laboratory PMSM driven by rotor-position synchronized square wave inverter. 57

Figure 3-3. Calculated and experimental voltage and current waveforms of the LSPMSM driven by a square wave inverter. (a) Calculated: —v_{ab}, —i_a. (b) Experimental: — v_{ab}, — i_a. 58

Figure 3-4. Current waveforms of the machines investigated driven by a square wave inverter with rotor position feedback at a load angle of 40°. (a) Original on-board EV motor. (b) On-board EV motor with a damper parameters corresponding to Table II. 61

Figure 3-5. Current waveform of the finalized EV motor with a damper having a stator to damper resistance ratio of 1:1 and stator to damper leakage inductance ratio of 1:5. 62

Figure 3-6. Calculated stator current of the original PMSM without a damper and proposed PMSM with a damper under a sudden increase in load angle. (a) Without damper. (b) With damper. 63

Figure 3-7. Calculated developed electromagnetic torque of the original PMSM without a damper and proposed PMSM with a damper under a sudden increase in load angle. (a) Without damper. (b) With damper. 64

Figure 3-8. Calculated developed speed of the original PMSM without a damper and proposed PMSM with a damper under a sudden increase in load angle. 64

Figure 3-9. Calculated stator phase current of the original PMSM and proposed PMSM with a damper under a sudden decrease in load angle. (a) Without damper. (b) With damper. 66

Figure 3-10. Calculated developed electromagnetic torque of the original PMSM and proposed PMSM with a damper under a sudden decrease in load angle. (a) Without damper. (b) With damper. 66

Figure 3-11. Calculated speed of the original PMSM and proposed PMSM with a damper under a sudden decrease in load angle. 67

Figure 3-12. Response of machine phase current during a three-phase symmetrical short circuit fault. 67

Figure 4-1. The in-house electric vehicle with a single-phase battery charger under consideration in the experimental investigations. 70

Figure 4-2. Grid current and voltage waveforms for the single-phase battery charger under consideration. (a) Low charging current. (b) High charging current. 71

Figure 4-3. Measured THD and the harmonic spectrum of the current waveform. (a) Low charging current. (b) High charging current. 72

Figure 4-4. Overall block diagram of the three-phase bi-directional charger. 73

Figure 4-5. Stator voltage and current of an IPMSM at stand-still condition. (a) Terminal phase voltage. (b) Terminal current when $\theta_r = 0°$. (b) Terminal current when $\theta_r = 60°$. (c) Terminal current when $\theta_r = 90°$. 74

Figure 4-6. The rms value of the induced current in *abc* phases with respect to rotor position θ_r for a given line voltage of 15 V. 75

Figure 4-7. Equivalent circuit of an IPMSM with a damper under blocked rotor condition. 75

Figure 4-8. Per phase equivalent circuit of an IPMSM with a special damper.. 75

Figure 4-9. Stator voltage and current of an IPMSM with a special damper at stand-still condition. (a) Terminal phase voltage. (b) Terminal current when $\theta r = 0°$. (c) Terminal current when $\theta r = 60°$. (d) Terminal current when $\theta r = 90°$. 76

Figure 4-10. Converter frequency response. (a) Gain plot of DC-DC converter at different battery charging power in dB. (b) Phase plot of DC-DC converter I at different output power, i.e. phase angle in degrees. 80

Figure 4-11. Converter frequency response. (a) Gain plot of DC-DC converter at battery discharging power in dB. (b) Phase plot of DC-DC converter I at varying output power, i.e. phase angle in degrees. 81

Figure 4-12. Current regulator system small-signal model of the DC-DC converter in the battery side. 81

Figure 4-13. DC-DC converter response during G2V operation at different power level. 82

Figure 4-14. DC-DC converter response during V2G operation at different power levels. 83

Figure 4-15. The *s*-domain block diagram of the decoupled current control loop for the three-phase battery charger. (a) *d*-axis. (b) *q*-axis. 88

Figure 4-16. The *s*-domain block diagram of the outer DC link voltage control loop for the three-phase battery charger. 88

Figure 4-17. The reduced *s*-domain block diagram of the outer DC link voltage control loop for the three-phase battery charger for Figure 4-16. 88

Figure 4-18. Overall block diagram showing the comprehensive control technique. 90

Figure 4-19. Calculated results illustrating the performance of the developed high performance level 3 bi-directional battery charger. (a) DC link voltage and current waveforms (b) *d*- and *q*-axis grid currents (c) Grid phase voltage and phase current.....90

Figure 4-20. Machine terminal voltage and current during integrated charging, (a) Terminal phase rms voltage. (b) Per phase current when θ_r=0°. (c) Per phase current when θ_r=45°. 92

Figure 4-21. Measured lead-acid battery characteristics using the charger on-board the battery electric vehicle. (a) Battery voltage. (b) rms values of AC and DC currents. (c) The battery current characteristics that are used to replicate the reference current for the developed charging system.....94

Figure 4-22. (a) Measured current and voltage waveforms during charging under grid only mode. Multiplication factors: DC link voltage (100V/Unit), Grid current (17A/Unit), Grid voltage (100V/Unit), Battery reference current (40A/Unit). (b) Near unity power factor achieved.....95

Figure 4-23. (a) Measured current and voltage waveforms under vehicle to grid condition. Multiplication factors: DC link voltage (100V/Unit), Grid current (28A/Unit), Grid voltage (100V/Unit), Solar PV reference current (20A/Unit). (b) Near unity power factor achieved. 96

NOMENCLATURE

L_{asas}, L_{bsbs}, L_{cscs}	: self inductances of phase *a*, *b*, *c*
L_{ls}	: stator leakage inductance
L_A, L_B	: saliency-independent and saliency-dependent inductances
θ_r	: electrical rotor angular position
L_{asbs}, L_{ascs}, L_{bscs}	: mutual inductances between phases
λ_{as}, λ_{bs}, λ_{cs}	: flux linkage in phase *a*, *b*, *c*
λ_0'	: flux linkage developed by the magnets referred to the stator side
i_{as}, i_{bs}, i_{cs}	: stator *a*, *b*, *c* phase current
v_{as}, v_{bs}, v_{cs}	: stator *a*, *b*, *c* phase voltage
r_s	: stator resistance
d_rq_r	: direct and quadrature axis in rotor reference frame
dq	: generalized direct and quadrature axis
θ	: electrical angular position of rotor of reference frame dq
θ_{r0}, θ_0	: initial angular position of reference frame d_rq_r and dq
ω_r, ω	: electrical angular speed of reference frame d_rq_r and dq
f_a,f_b,f_c	: voltage, current or flux quantity in *abc* frame
f_d,f_q	: voltage, current or flux quantity in dq frame
θ_s	: time phase of the a defined signal f
ω_s	: electrical angular frequency of a defined signal f
$M^{abc\text{-}dq}$	: transformation matrix from *abc* frame to dq frame
$M^{dq\text{-}abc}$	: transformation matrix from dq frame to *abc* frame
λ_{ds}, λ_{qs}	: *d*- and *q*-axis flux linkages
i_{ds}, i_{qs}	: *d*- and *q*-axis currents
L_{md}, L_{mq}	: *d*- and *q*-axis magnetizing inductances
L_{ds}, L_{qs}	: *d*- and *q*-axis synchronous inductances
v_{ds}, v_{qs}	: *d*- and *q*-axis voltages
p	: differential operator d/dt

T_e	: electromagnetic torque
P	: number of poles
L_{arar}, L_{brbr}, L_{crcr}	: rotor self inductances of phase *a*, *b*, *c*
L_{arbr}, L_{brcr}, L_{arcr}	: mutual inductances between rotor phases
L_{asbr}, L_{bscr}, L_{ascr}	: mutual inductances between stator and rotor phases
i_{ar}, i_{br}, i_{cr}	: rotor *abc* phase current
λ_{ar}, λ_{br}, λ_{cr}	: flux linkage in rotor phase *a*, *b*, *c*
λ_{dr}', λ_{qr}'	: *d*- and *q*-axis rotor flux linkage referred to the stator side
i_{dr}', i_{qr}'	: *d*- and *q*-axis rotor current referred to the stator side
v_{ar}', v_{br}', v_{cr}'	: rotor *abc* phase voltage referred to the stator side
r_r'	: rotor resistance referred to the stator side
L_m	: magnetizing inductance of non-salient machine
L_s, L_r'	: stator and rotor synchronous inductance referred to the stator side
r_{kd}', r_{kq}'	: *d*- and *q*-axis damper resistance the referred to the stator side
L_{kd}', L_{kq}'	: *d*- and *q*-axis damper inductance referred to the stator side
L_{lkd}', L_{lkq}'	: *d*- and *q*-axis damper leakage inductance referred to the stator side
V_{DC}, I_{DC}	: measured DC voltage and current of the DC test
$\hat{V}_{ab}$	: peak value of the line *ab* voltage.
n_m	: mechanical revolutions per minute of the rotor
I_{ph}	: measured phase current on synchronous speed loading test
V_t	: measured terminal voltage on synchronous speed loading test
X_{ds}, X_{qs}	: *d*- and *q*-axis stator synchronous reactance
E	: induced emf generated by the magnet flux
δ	: load angle
θ	: power factor angle
β	: phase angle between *b* phase voltage and *a* phase current
T_{epm}	: torque component arising from the synchronous motor action
$T_{edamper}$	: torque component arising from the induction motor action
S_a, S_b, S_c	: boolean variable representing the switching logic of leg 1, 2, 3

v_{an}, v_{bn}, v_{cn} : inverter *abc* phase voltage

V_{dc} : inverter DC link voltage

v_{ab}, v_{bc}, v_{ca} : inverter *ab*, *bc*, *ca* line voltage

Z_{eq} : equivalent impedance of the magnetizing branch and damper

G_1, G_2 : transfer function representing charging and discharging operation

$\tilde{\ }$: small AC disturbance of the battery current

$\tilde{\ }$: small AC disturbance of the duty ratio during charging

R_1 : conceptual output resistor representing load effect of battery

L_1, C_1 : filter inductor and capacitor of the DC-DC converter

R_{C1}, R_{L1} : internal resistances of the filter inductor and capacitor

$\tilde{\ }$: small AC disturbance of the duty ratio during discharging

R_2 : conceptual output resistor on the grid side

C_2 : total capacitance at the DC link

r_{C2} : total ESR at the DC link

v_{sd}, v_{sq} : *d*- and *q*-axis components of utility voltage

i_{std}, i_{stq} : *d*- and *q*-axis components of the grid converter current

V_{cond}, v_{conq} : *d*- and *q*-axis components of the AC side terminal voltage of VSC

v'_{cond}, v'_{conq} : *d*- and *q*-axis VSC voltage without cross coupling terms

R_s, L_s : per phase resistance and inductance of the AC choke

i_{load} : current flowing out of the capacitor to the battery

v_{dc}, i_{dc} : instantaneous DC link voltage and current of the VSC

V_{bus} : magnitude of the grid voltage space vector

K_{pd}, K_{id} : proportional and integral gain of the *d*-axis current controller

K_{pq}, K_{iq} : proportional and integral gain of the *q*-axis current controller

K_{pdc}, K_{idc} : proportional and integral gain of the DC link voltage controller

i_{ds}^*, i_{qs}^* : *d*- and *q*-axis reference current

Chapter 1

Introduction and Literature Review

1.1 Overview

With increasing environmental deterioration, the need to control the greenhouse gases emission has become prominent. According to a report [1] by International Energy Agency, the worldwide CO_2 emission from fuel combustion has increased from 14 billion tons in 1971 to 31 billion tons in 2011, 22% of which is accounted by transportation. In addition, the growing demand and limited reserves of fossil-fuel in the world have driven the Organization of the Petroleum Exporting Countries (OPEC) Reference Basket price to rise from an average of $23.1/b in 2001 to $105.8/b in 2013. The road transportation sector shares over 50% of the oil demand [2]. As a result, achieving sustainable transportation has emerged as a vital mission. Electrified vehicles (EVs) is considered one of the most promising solutions to increase energy security and reduce emissions of greenhouse gases and other pollutants [3].

The main electrical components of a pure battery electric vehicle (BEV) are shown in **Figure 1-1**. A battery pack is connected to an electric machine through a power electronic based drive system. The drive system controls the electric machine which acts as a motor or generator (MG) depending whether the vehicle is driving or breaking. The electric machine is mechanically coupled to the transmission, which is in turn connected to the wheels. In order to recharge the battery pack, a BEV is generally equipped with an on-board single-phase battery charger.

Hybrid electric vehicles (HEVs) and plug-in hybrid electric vehicles (PHEVs) are proposed to serve as a compromise for the environmental pollution problem and the limited range capability of BEVs [4]. HEVs are classified into four kinds: 1) series hybrid; 2) parallel hybrid; 3) series-parallel hybrid and 4) complex hybrid [5].

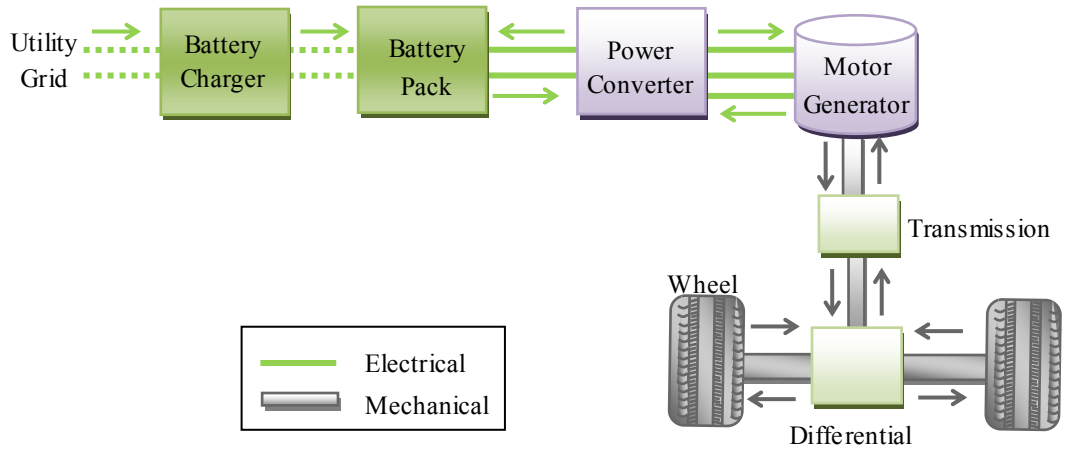

Figure 1-1. Main drivetrain components and power flow of a pure electric vehicle.

The series architecture as shown in Figure 1-2(a) is the simplest kind for HEV. Only the driving motor/generator is connected to the wheel. The internal combust engine (ICE) is coupled with a generator. The mechanical output of the ICE is converted to electricity which is either used to charge the battery or to provide electric power directly for the driving motor. Because of this simple structure of the mechanical linkage, the location of engine and motor is flexible. However, the series hybrid configuration requires three propulsion devices: an ICE, an electric motor and one additional generator, which adds weight and cost [6]. Moreover, the traction motor must be sized for maximum sustained power because it is the sole propelling source for the vehicle [5, 7].

On the other hand, parallel hybrid, as shown in Figure 1-2(b) allows both the ICE and electric motor to deliver power in parallel to drive the wheels. The ICE and electric motor are generally coupled to the drive shaft of the wheels via two clutches, and as a result, they can deliver propulsion power independently or simultaneously [5]. The electric motor can also be used as a generator to charge the battery by regenerative braking or by using the excess power created by the engine. With an extra mechanical linkage and complexity in energy management, parallel hybrid overcomes the disadvantages of a series hybrid [5, 8, 9].

The series-parallel hybrid configuration, shown in Figure 1-2(c) incorporates the features of both series and parallel HEVs [4]. In this configuration, two mechanical power sources are connected to the driveline. One is the combination of the ICE and generator while the

other is the main electric motor. Determined by the power management system, the two power paths provide propulsion power to the vehicle simultaneously and independently. Series-parallel hybrid is relatively more complicated and costly, but able to achieve excellent dynamic performance and extended driving range.

The key difference between a series-parallel hybrid and complex hybrid system shown in Figure 1-2(d) is the bidirectional power flow of a secondary motor. This bidirectional power flow can allow for versatile operating modes, specifically a three propulsion power operating mode which cannot be offered by the series-parallel hybrid. This topology increases the overall dynamic performance of the vehicle. Similar to the series-parallel HEV, the complex hybrid suffers from higher complexity and cost [5].

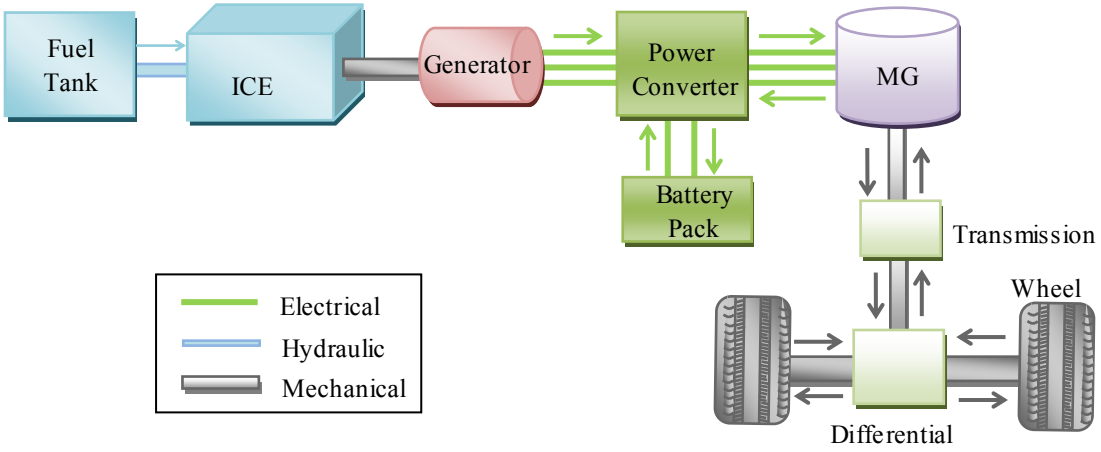

(a)

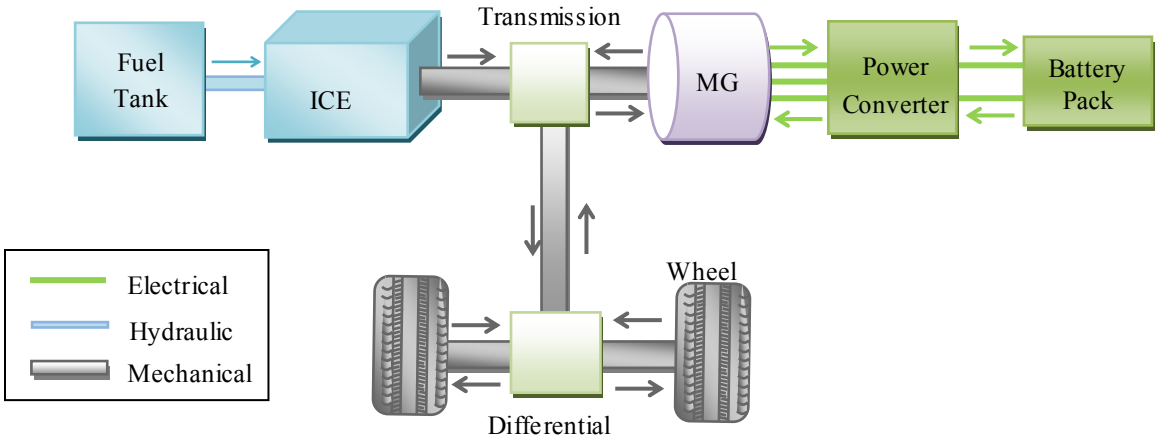

(b)

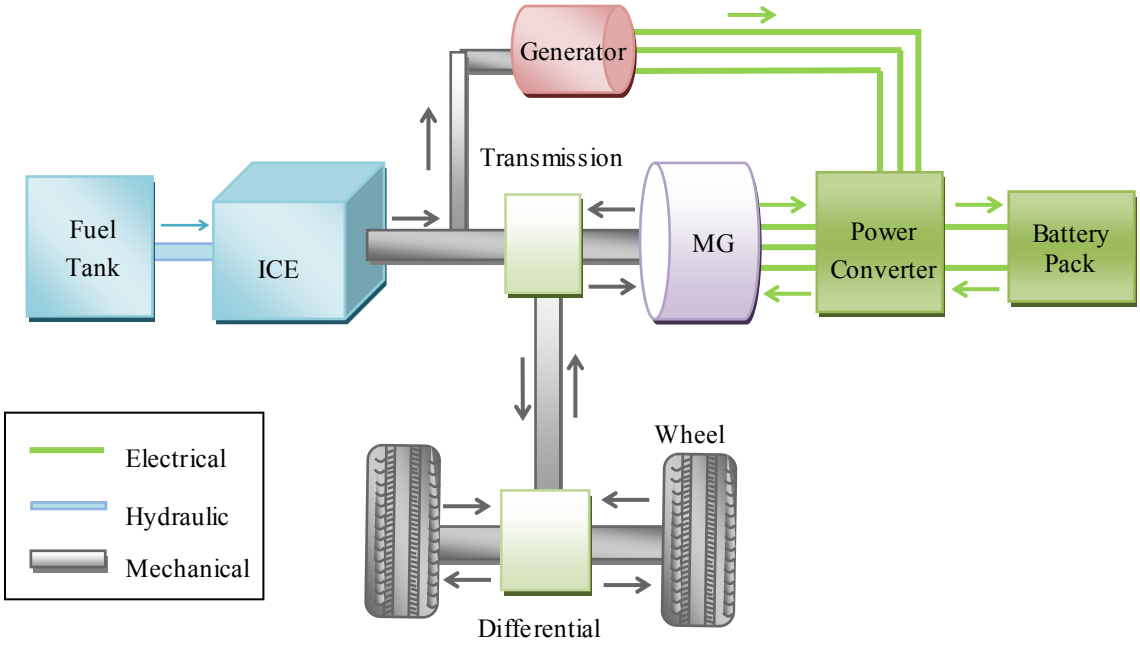

(c)

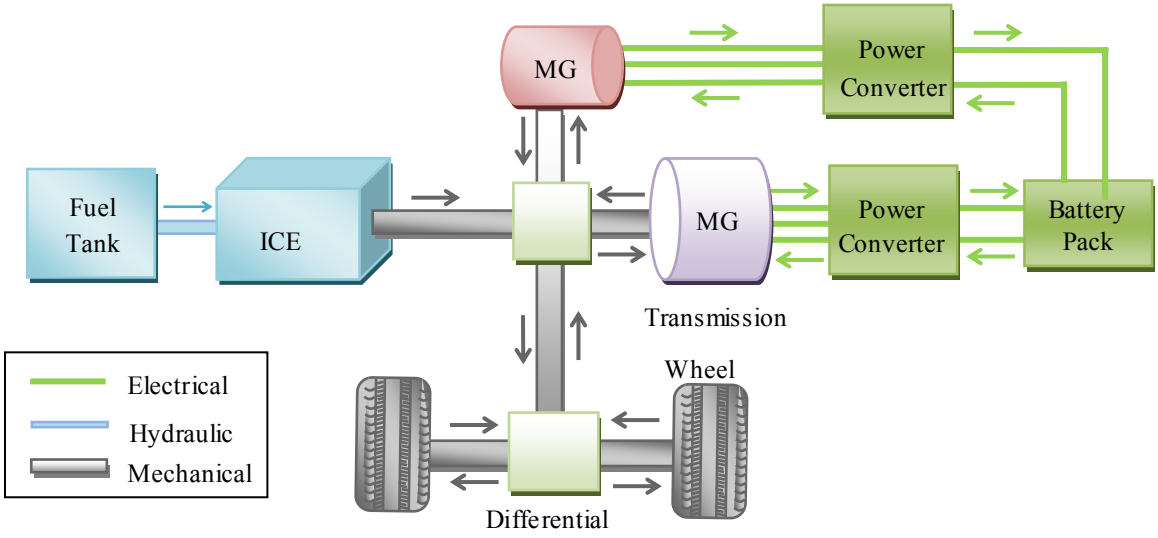

(d)

Figure 1-2. Main drivetrain components and power flow of hybrid electric vehicles. (a) Series hybrid. (b) Parallel hybrid. (c) Series-parallel hybrid. (d) Complex hybrid.

1.2 Electric Machines for EV Application

Regardless of the architecture, the main propulsion force for an EV is the electric machine. It is of great importance to tailor the performance of electric machines for electric vehicle application. Conventionally, electric machines used for various

applications such as manufacturing, machining, conveyors etc. operate in a small range of speed and torque with reasonable efficiency. Requirements for EV application are comparatively more stringent [8-10], and include:

- high instant power and high power density;
- wide speed range and a constant power operating range of 3-4 times the base speed;
- fast torque response;
- high efficiency over wide ranges of speed and torque for both motoring and regenerating;
- high reliability and robustness for various vehicle operating conditions;
- intermittent overload capability, typically twice the rated torque for short durations, typically for 15-20 seconds;
- compact, light weight and reasonable cost.

There are three major types of electric machines that are considered suitable for EV applications: 1) permanent magnet synchronous machines (PMSMs); 2) induction machines (IMs); and 3) switched reluctance machines (SRMs) [11]. The cross-section of these traction motors are presented in Figure 1-3.

The development of PMSMs in 1950s was advocated by the availability of modern permanent magnets (PMs) with considerable energy density and the advent of transistor based power electronic devices [12]. In addition to being brushless and having no mechanical commutator, in a PMSM, the magnetic field is excited by permanent magnets. Hence, the overall weight and volume can be significantly reduced for a given output power, leading to higher power density. There is ideally no current in the rotor of a PMSM and therefore its efficiency is higher compared to an induction machine. It is also easier for the heat to dissipate in a PMSM, since most of the power losses are concentrated in the stator. Because of the lower electromechanical time constant of the rotor, the rotor acceleration at a given input power can be increased [5]. However, the manufacture of PMSMs heavily depends on rare-earth materials which are limited and only available in some countries, as a result, the price of these motors is comparatively higher than other types.

Despite the limited access and high cost of permanent magnets, most of the existing electrified vehicles use PMSMs as traction motor. Due to the high efficiency and energy density, PMSMs are still the most favorable options when it comes to EVs [13]. Most of the existing BEVs and HEVs such as Ford Focus [14], Nissan Leaf [15] and Toyota Prius [16] etc. use PMSMs as the main electric propulsion and generation unit. There is a significant amount of work that has been published on the design in both the rotor and stator, aiming to further improve the performance of PMSMs.

1.2.1 Basic PMSM Configurations

PMSMs can be broadly categorized into two groups based on their rotor construction and stator windings [17]. Based on the position of PMs in the rotor, PMSMs can be classified as surface PMSMs (SPMSMs) with the magnets mounted on the surface of the iron rotor core, Figure 1-4(a), or interior PMSMs (IPMSMs) with the magnets buried inside the rotor core, Figure 1-4(b). The characteristics of SPMSMs and IPMSMs have been compared at a given vehicle specification and inverter size [12, 18, 19]:

- SPMSMs have shorter end connections and shorter overall length and are easier to manufacture;
- IPMSMs have excellent overload capability throughout their speed range;
- Losses increase for both motors at high speed, particularly the extra joule losses in SPMSMs and the slot harmonic losses in IPMSMs;
- SPMSMs are mechanically less robust than IPMSMs, and not ideal for high speed operation;
- The quadrature and direct axis inductances for SPMSMs are equal, while for IPMSMs the quadrature axis inductance is larger than direct axis inductance.

The stator windings of PMSMs may be either concentrated (i.e., non-overlapping, surrounding individual teeth) or distributed (i.e., overlapping, spanning multiple teeth). In concentrated type of windings, all the winding coil turns have the same coil axis and are wound together in series to form one multi-turn coil. In distributed types of windings, the axis of a coil in one set of slots is different from the axis of a coil in the adjacent set of slots and all the winding turns are arranged in several full-pitch or fractional-pitch coils.

These coils are then housed in the slots spread around the air-gap periphery to form a phase winding [20]. The characteristics of distributed windings and concentrated windings can be summarized [17, 21]:

- Distributed windings make the waveform of the induced electromotive force (EMF) more sinusoidal in nature, i.e. magnitude of harmonic components is smaller, hence less torque ripple manifests in the machine;
- Due to the larger number of conductors per slot in concentrated winding machines, heat dissipation is poor and therefore they have lower demagnetization tolerance than distributed windings;
- Since concentrated windings are wound on individual teeth, their mutual inductance between phases are smaller than those of distributed windings;
- Concentrated winding machines have shorter end coils, and therefore lower copper loss than a distributed winding machine.

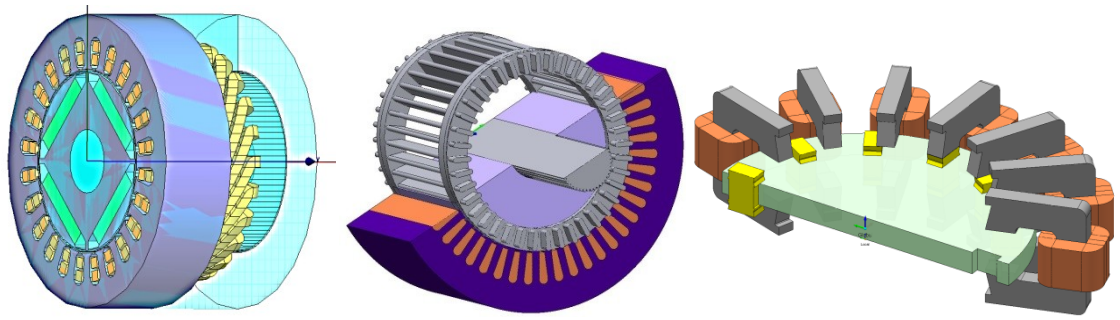

(a) (b) (c)

Figure 1-3. Cross-sections of the various traction motor technologies. (a) PMSM. (b) Induction motor. (c) Axial flux SRM.

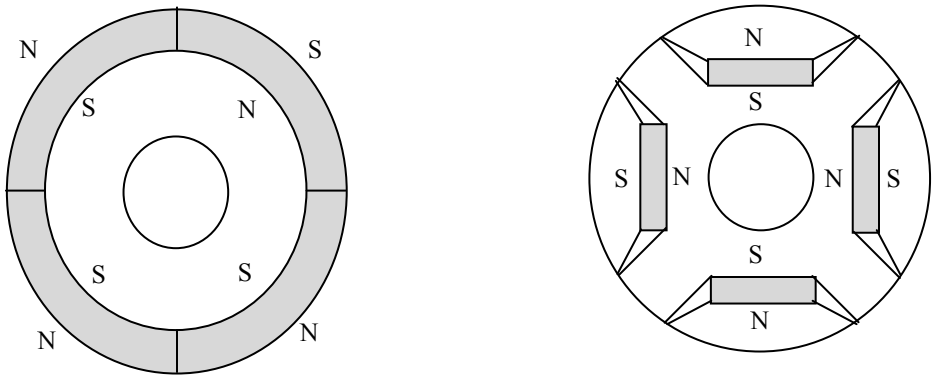

(a) (b)

Figure 1-4. PMSM rotor configuration. (a) Surface mount. (b) Interior buried.

1.2.2 Literature Review of PMSM Design for EV Application

In order to meet the requirements of electric vehicles, innovative designs of PMSMs have been proposed and evaluated based on efficiency, reliability, power density and cost. There is a considerable amount of literature that is present in this topic.

Rahman *et al* [22] presented a design of a hybrid permanent magnet hysteresis synchronous motor where the magnets were inserted into the slots at the inner surface of the hysteresis ring. In this design, the negative effect of the magnet braking torque of a conventional PM motor is ideally compensated by the high eddy current and hysteresis torques during the initial run-up period. The machine combines the advantageous performance features of both conventional hysteresis motors and the PM motors.

A study of the design of multi-layer IPMSMs by Honda *et al* [23], compares the performance of one, two, three, six and ten permanent magnet layers in the rotor. It is seen from simulations and experiments that the two-layer rotor is the best in terms of maximizing the utilization of both reluctance torque and magnet torque. Nerg *et al* [24] illustrated the design process of direct-driven PMSMs for a full electric sports car. The rotor of the machine has two PM layers embedded inside the rotor laminations, thus resulting in inverse saliency so as to take advantage of the additional reluctance torque.

A permanent magnet machine with a doubly fed doubly salient stator that has an extra flux path in shunt with each PM pole amplifies the effect of flux weakening for constant power operation. This proposed topology by Chau *et al* [25] is shown to reduce both PM material and field winding magneto motive force (MMF) significantly and offer a distinct advantage of wide constant power operation range (four times the base speed), which is important for EV application.

In order to increase the speed range of the machine, Stumberger *et al* [26] presented an IPMSM rotor design with magnet segments and Dutta *et al* [27] further analyzed the suitability of a segmented magnet IPMSM for EV application. It is shown that the segmented magnet rotor structure is effective in reducing the iron loss in the machine and eventually yields higher efficiency. Moreover, the machine shows an extremely wide constant-power speed range which exceeds 5:1.

The idea of utilizing a multiphase IPMSM for HEV was first suggested by Parsa *et al* [28]. A PM machine with four poles and five phases with fractional slots was designed and developed. The machine is shown to remain operational under loss of up to two phases without any additional hardware connections and is considered more reliable for vehicles. Also, due to the winding distribution and the greater number of phases, the machine has low torque pulsation. Further, Zheng *et al* [29] investigated the fault toleration ability of a five-phase PMSM with 40-slot/42-pole scheme for in-wheel application. Based on the application of an auxiliary winding to reduce torque fluctuation caused by cogging toque, a method was introduced by Abbaszadeh *et al* [30].

The efficiency and torque depend heavily on the split ratio of the outer stator and inner stator. By optimizing the split ratio, the output torque of the motor can be high enough for in-wheel application. An analytical method to optimize the split ratio and maximize output torque was first brought out by Pang *et al* [31]. Feng *et al* [32] extended the method and applied it to a double-stator PMSM for in-wheel drive to improve the efficiency of the HEV drivetrain.

Arakawa *et al* [33] proposed an axial gap IPMSM motor with leakage poles piercing the rotor in the axial direction. Since *q*-axis flux can easily pass through the leakage poles in the axial direction, the proposed motor can make effective use of reluctance torque. In comparison with the motor in the third-generation Toyota Prius, the proposed motor provides twice the maximum torque and more than 1.95 times the torque density of the reference motor while retaining the same size. In addition, the motor manifests sufficient durability against irreversible demagnetization of the permanent magnets and the stress caused by rotating the rotor.

A compound-structure PMSM which is composed of a stator with fractional slots and a double-rotor as traction motor for HEVs was optimized by Liu *et al* [34]. The slot openings and pole-arc embraces are optimized to decrease torque fluctuation. Moreover, the magnetic coupling between the stator and the double-rotor can be negligible, and therefore enables the independent control of the two members.

For high performance PM machines for HEVs, an alternative rotor design was explored by Dorrell *et al* [35]. Ferrite magnet rotor design was considered instead of a rare-earth approach. The initial design suffered demagnetization under high load. It was found that this issue can be mitigated by further embedding the magnets in the rotor to protect them, and therefore is considered a cost-effective solution.

1.3 Electric Vehicle Charging Infrastructure

As EVs enter the stage of commercialization, various issues should be considered for the EV charging infrastructure. This includes: availability of charging stations; convenience of payment for charging; standardization of EV batteries and charging power; regulation of clean and safe charging; impacts on power utilities [5]. Charging devices can be categorized into three levels based on the charging voltage and current [36, 37].

- Level 1 AC (120 V, 15 A or 20 A) is the lowest common voltage level found in both residential and commercial buildings. The rated charging power of a level 1 charger is 1.8-2.4 kW and it takes 12-16 hours to fully charge the Tesla Roadster EV and 3 hours for Toyota Prius plug-in;

- Level 2 AC (Greater than 125 V or greater than 20 A) charging generally requires a 208V-240 V single-phase supply and a typical current of 40 A up to 60 A. The power of level 2 charging is up to 14.4 kW. Tesla Roadster takes around 6-8 hours and Toyota Prius Plug-in takes around 2 hours to charge using level 2;

- Level 3 DC Fast Charging (208, 480 or 600 V AC) using three-phase AC power over 14.4 kW, are able to provide the fastest charging time. They typically are off-board chargers to provide the AC to DC conversion. The vehicle's on-board battery management system (BMS) controls the off-board charger to deliver DC directly to the battery. With level 3 charging, it is expected that these vehicles will be charged within 15-30 minutes to approximately 80% of the battery capacity.

Level 1 and level 2 charging are predicted to be the most commonly adopted schemes for EVs in the future because of their convenience and low-cost [37]. However because of the low power rating, long charging time is required. Also, as the number of EVs

increases, more power will be required from the grid. As level 1 and level 2 require single-phase power, severe unbalanced loading will be imposed in the utility grid. Level 3 charging provides high power and hence significantly reduces the charging time. But because of the large size and weight, it is normally off-board and not available residentially. Therefore, a three-phase integrated charger, using available electric drivetrain hardware, mainly the electric motor and the inverter, for the charging circuit, was proposed to avoid the problems of additional charger weight, space, and cost [38].

1.3.1 Introduction to Integrated Charging

Figure 1-5(a) illustrates the schematic block diagram of a three-phase level 3 charger which consists of power electronic converters and line inductors. During the battery charging mode, the three-phase AC-DC converter essentially acts as a high performance rectifier with near-unity power factor. A boosted constant DC link voltage of more than the peak of the utility input line-to-line voltage for this rectifier can be maintained by properly controlling the power electronics switches of the rectifier. A DC-DC converter in between this rectifier and the battery of the vehicle is required for battery charging control based on command generated by BMS. A current or voltage control strategy is employed to adjust the current injected into the battery so as to charge the battery at an acceptable rate. To make the rectifier act as a boost AC-DC converter and minimize the harmonic components injected by high frequency switching, line inductors are connected in series with the converters.

The traction motor drive system configuration is shown in Figure 1-5(b). During motoring, the DC-DC converter will be responsible for maintaining a constant DC link at the input of the AC-DC converter, which operates as an inverter for motor drive application. During regenerating mode, the power flow goes from the machine to battery.

It can be seen that the power electronic components for a three-phase battery charger and an AC motor drive system are basically the same. Therefore, the drive system can be used for charging with additional contactors for mode switching. Because of the bidirectional nature of the traction system, both grid to vehicle (G2V) charging and vehicle to grid (V2G) discharging can be implemented. Moreover, the line inductors can

be replaced by machine windings with various configurations. As a result, the additional components for on-board three-phase charger materials are simply relays/contactors. And for the grid side, only a three-phase outlet is needed. However, there are certain issues that need to be considered for integrated charging [38, 39]:

- unwanted torque developed in the motor during charging;
- low order harmonic content in the current from the grid;
- mandatory unity power factor operation;
- the optimized design and sizing of the motor and power electronic converters;
- complicated control strategy due to saliency in IPMSMs;
- isolation between the charger and the grid.

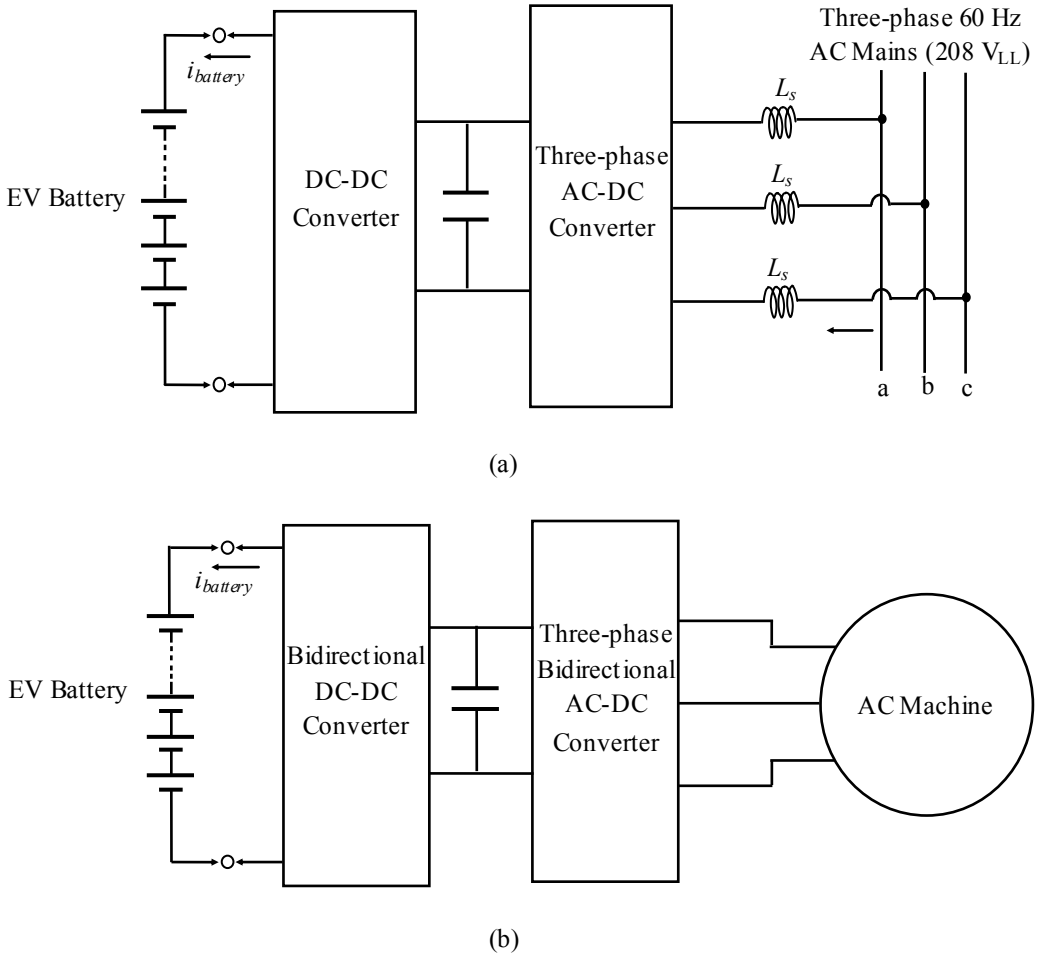

Figure 1-5. Block diagram of a three-phase battery charger topology and traction motor drive.

1.3.2 Literature Review of Integrated Charging for EVs

Different types of integrated chargers have been reported to solve the aforementioned challenges by using additional hardware or innovative control algorithms.

Rippel [40] designed and patented a single integrated traction inverter and battery charger apparatus. The design integrates the components of a three-phase inverter with an AC-DC converter in a manner which recognizes that an input capacitor and certain components of a three-phase bridge inverter are capable of performing dual functions. Therefore, some of the components are eliminated allowing reduction of cost, weight and space required by the integrated inverter/charger apparatus.

A single-phase/three-phase combined battery recharge and motor drive system employs a conventional voltage source inverter and a poly-phase motor which may be reconnected to operate in a battery recharge mode. This design was proposed and patented by Cocconi [41]. During charging time, the motor is used as a set of inductors in series with the inverter to ensure unity power factor operation towards the utility/grid side. The system is currently in use in the car industry [42]. A similar integrated drive/charger system with an induction motor is reported for a fork lift truck [43].

A single-phase integrated battery charger that utilizes the existing hardware of a four-wheel drive electric vehicle was introduced by Ki *et al* [44]. Two pairs of inverters and motor windings are configured as a single-phase boost rectifier to generate DC power in the DC link capacitor, while the other two pairs of inverters and motors are configured and operated as a full bridge DC-DC converter to charge the battery. The developed prototype can operate at constant voltage and constant current charging mode at unity power factor with only one mechanical transfer switch added to the drivetrain. Tang *et al* [45, 46] and Su *et al* [47, 48] described and prototyped a 14 kW single-phase on-board integrated charger for PHEVs connected in a similar manner. The proposed charger uses the main traction motor, auxiliary motor and associated power electronics systems of an HEV to construct the charger circuit.

In a three-phase traction/fast-battery-charger drive which composes two three-phase PWM boost converters and a buck-boost chopper, each phase of the AC grid is connected

to two parallel boost converters. This connection analyzed by Bruyere *et al* [49], Sousa *et al* [50-52], Lacroix *et al* [39] and Sandulescu *et al* [53] is realized through the midpoint of each winding of the electric machine. In the case of balanced current in each half windings of a given phase, the rotating magnetic field components at the stator level are eliminated and therefore no electromagnetic torque is developed during charging operation.

Haghbin *et al* [54, 55] and Subotic *et al* [56] constructed a single/three-phase integrated battery charger based on a split-phase/six-phase machine and six-leg inverter. For a single-phase AC source, the neutral of each winding is connected to the power source, and each phase is connected to the midpoint of the inverter. For a three-phase source, the same phases of each winding are connected in series or in parallel and connected to each phase of the AC source. With voltage oriented control, the developed torque of the machine at stand-still during charging can be maintain as zero.

The stator windings can be reconfigured by relay based switching devices to constitute a special grid connected generator for charging. This rotary generator (machine with re-configured windings) provides an isolated three-phase power source for the inverter to make a three-phase boost battery charger. This high-power integrated charger with isolation was proposed by Haghbin *et al* [38, 57-59].

1.4 Motivation for this Dissertation

In this study, an interior permanent magnet synchronous machine with damper bars is proposed to: 1) improve the dynamic performance in the high speed region and system response during short circuit faults. 2) Mitigate the unbalanced effect caused by buried magnets in the machine and facilitate integrated charging for EVs.

The idea behind this study originated from conventional synchronous machines with dampers for providing self-starting capability and improving stability. A line-start PMSM (LSPMSM) is an example of PMSM with a damper cage. However, the damper in a LSPMSM is primarily for direct online starting and secondarily to help maintain transient stability. In this study a special damper is proposed to be added into a IPMSM so that the machine can be used for EV propulsion and integrated charging.

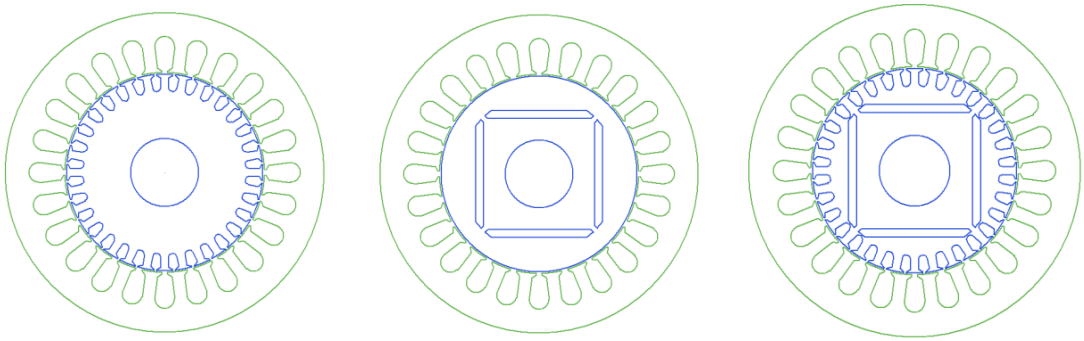

(a) (b) (c)

Figure 1-6. Construction of different machines. (a) Induction machine. (b) PMSM. (c) IPMSM with symmetric damper.

Figure 1-6 shows the structure of three machines, (a) an induction machine, (b) a PMSM and (c) a LSPMSM with a symmetric damper. PM machines, (b) or (c), generally have a significantly higher efficiency than IMs due to their negligible rotor losses at normal synchronous speed operation. The use of permanent magnets not only allows these machines to maintain a synchronous speed in loaded conditions, but also provides greater torque and power density than their equivalent induction motors.

The addition of the damper in machine (c) offers advantages over PMSMs without them. The damper lowers the equivalent reluctance of rotor, thus offering improved transient response during dynamic conditions. In [60], two interior-magnet synchronous machines with and without dampers were designed and it was found that the damper bars improved the stability and increased the maximum output and efficiency.

Also the machine with damper windings operates to suppress the transient oscillations with no external feedback. The feedback comes internally through the induced EMF due to the slip speed in the cage windings, whereas in the inverter-controlled PM drives, the controller has to be initiated by an external signal or feedback variable to counter the oscillation. Hence the inverter-controlled drive's dependence on an external feedback loop compromises reliability. EVs require reliable operation regardless of the accuracy in torque or position control and the PMSM with damper windings is considered an intelligent choice for this application [12]. It is also shown in [61] that adding damper bars on the outer surfaces of the machine is effective to reduce the danger of PM demagnetization due to a short circuit fault.

Unlike a LSPMSM with a conventional squirrel cage, the proposed machine has special selected damper with high leakage on the axis oriented to the magnet to mitigate the saliency of the rotor at stand-still condition. This characteristic is beneficial for integrated charging.

The proposed strategy takes advantage of existing IM and PMSM technology, and therefore, requires relatively low manufacturing costs. However, the additional aluminum cage increases the material cost, size and weight of the machine. If a 2010 Prius motor is considered, which weighs 13.0 kg with a rotor diameter of 8 cm [62]; the additional damper will increase the weight by about 5%. Also an additional cost of the machine will be incurred by adding the damper. But this cost can be compensated since no additional components for a three-phase charger is required. This study does not claim that the proposed structure is the most cost effective solution. Instead, it tries to investigate the scientific merits and suitability of such rotor construction for EV application.

1.5 Dissertation Objective

The objective of this dissertation is to investigate performance of IPMSM with damper for EV traction and charging applications. More specifically, these objectives include the following:

- Develop a dynamic model for an interior permanent magnet machine with shorted damper bars that can evaluate machine dynamic and steady-state performance characteristics such as flux linkage, torque, speed etc.
- Propose parameter determination methods to find out the equivalent circuit of the IPMSM with damper. Verify the determined parameters and developed model through simulation and experiment results.
- Experimental test of the traction machine characteristics and charging profile of a laboratory EV and HEV.
- Investigate the effect of dampers in IPMSM considering dynamic performance in high speed operation and response to short circuit condition.
- Establish bi-directional fast charging for both V2G and G2V. Evaluate the role of damper in IPMSM for three-phase integrated charging

1.6 Dissertation Layout

Chapter One provides a brief introduction of the architecture and major components of EVs. The classification of PM machines is illustrated and the current research on improving the performance of the machines is summarized. Furthermore, the charging strategy and charger topology BEVs and PHEVs is introduced. A thorough study of the EV drivetrain architecture and traction motor requirements as published in [4, 11].

Chapter Two gives a detailed illustration of the equivalent circuit modeling of a PMSM with a damper [63]. A synchronous speed loading test method with measured load angle is proposed to determine the *d*- and *q*-axis synchronous reactance. For a known cage construction, a blocked rotor test is used to find the stator leakage inductance and damper parameters [64, 65]. In addition, a single-phase AC test is proposed to determine damper parameters without previous knowledge of the damper structure based on the author's previous work in synchronous machine presented in [66, 67].

Chapter Three establishes the need for machines with high dynamic performance through case study of HEVs. It is shown that under high speed conditions, the inverter operates at a 180 degree conduction mode. An IPMSM used as a traction motor and the proposed machine with damper of the same power ratings are simulated and results are analyzed. Both machines are also subjected to a short circuit test and subsequent analysis.

Chapter Four studies an in-vehicle single-phase charger and proposes a three-phase high power fast charging strategy using the existing EV drivetrain components. The significance of the damper in compensating the unbalanced condition caused by buried magnets at standstill is demonstrated through theoretical analyses and simulations. Real-time simulation of the system is presented to demonstrate the operation of the proposed DC fast charging system [68, 69].

Chapter Five concludes this dissertation with a summary of the work presented in previous chapters, identifying the new technical contributions that provide the basis for this PhD research project. A proposal is presented for the future work to extend this research topic.

Chapter 2

Equivalent Circuit Modeling

2.1 Introduction

In order to study machine behaviour, models that can express the relation between machine flux, voltage, current, speed, torque etc. need to be developed. Models based on finite element analysis (FEA) can directly determine the flux patterns and machine characteristics in great details, however the process is computationally intensive and time consuming. Magnetic circuit models (MCMs) have also been proposed to represent the machines, as they require less computation time compared to FEA models. However, since differential equations are written for each individual slot in the machine, MCMs generally have high order and are considered too complicated for motor controller design. Therefore this work develops and uses simplistic equivalent circuit models based on the principle of electromechanical energy conversion, magnetically coupled circuits theory and reference frame theory for general performance analysis and motor drive design. The model is proved to be simple and effective in representing the relation between key variables in a machine.

2.2 Equivalent Circuit Modeling based on Reference Frame Theory

In developing equations for a PMSM with damper bars, the following assumptions are made [70]:

- The armature and field MMFs are sinusoidally distributed in space;
- Magnetic hysteresis is negligible;
- Magnetic saturation effects are negligible.

2.2.1 Winding Inductances and Voltage Equations for PMSMs in the abc Frame

As proved in [71], the self inductances of stator *abc* phases and the mutual inductances between phases can be written as:

$$\left.\begin{aligned} L_{asas} &= L_{ls} + L_A - L_B \cos 2\theta_r \\ L_{bsbs} &= L_{ls} + L_A - L_B \cos 2\left(\theta_r - \frac{2\pi}{3}\right) \\ L_{cscs} &= L_{ls} + L_A - L_B \cos 2\left(\theta_r + \frac{2\pi}{3}\right) \end{aligned}\right\} \tag{2.1}$$

$$\left.\begin{aligned} L_{asbs} = L_{bsas} &= -\frac{1}{2}L_A - L_B \cos 2\left(\theta_r - \frac{\pi}{3}\right) \\ L_{ascs} = L_{csas} &= -\frac{1}{2}L_A - L_B \cos 2\left(\theta_r + \frac{\pi}{3}\right) \\ L_{bscs} = L_{csbs} &= -\frac{1}{2}L_A - L_B \cos 2\left(\theta_r + \pi\right) \end{aligned}\right\} \tag{2.2}$$

where L_{ls} is the per-phase stator leakage inductance, L_A and L_B are respectively the saliency-independent and saliency-dependent inductances of the synchronous machine [71]. These terms are constant and are determined by the dimensional and magnetic properties of the machine [71]. For machines such as a squirrel-cage induction machine, a cylindrical rotor synchronous machine and a surface-mounted PMSM, $L_B = 0$.

In this study, counter-clockwise rotation is considered as positive. The angular electrical speed of the rotor is denoted by ω_r. The axis along the magnet is defined as direct axis (d_r axis). The axis along the electrically quadrature (or perpendicular) to the magnet axis is called the quadrature axis (q_r axis). θ_r denotes the rotor angular position which is the angle between q_r axis and stator *a* phase. An illustration of this convention is shown in Figure 2-1. The relation between stator currents and flux linkage for PMSM can be expressed as:

$$\left.\begin{aligned}
\lambda_{as} &= L_{asas} i_{as} + L_{asbs} i_{bs} + L_{ascs} i_{cs} + \lambda_0' \sin\theta_r \\
\lambda_{bs} &= L_{bsas} i_{as} + L_{bsbs} i_{bs} + L_{bscs} i_{cs} + \lambda_0' \sin\left(\theta_r - \frac{2\pi}{3}\right) \\
\lambda_{cs} &= L_{csas} i_{as} + L_{csbs} i_{bs} + L_{cscs} i_{cs} + \lambda_0' \sin\left(\theta_r + \frac{2\pi}{3}\right)
\end{aligned}\right\} \tag{2.3}$$

where i_{as}, i_{bs} and i_{cs} are the stator phase currents and λ_0' is the peak or aligned value of the flux linkage established by permanent magnets referred to the stator.

Based on principles of electric circuits and electromechanical energy conversion, the voltage equations for the machine are:

$$\left.\begin{aligned}
v_{as} &= r_s i_{as} + \frac{d\lambda_{as}}{dt} \\
v_{bs} &= r_s i_{bs} + \frac{d\lambda_{bs}}{dt} \\
v_{cs} &= r_s i_{cs} + \frac{d\lambda_{cs}}{dt}
\end{aligned}\right\} \tag{2.4}$$

where r_s is the resistance of the stator winding.

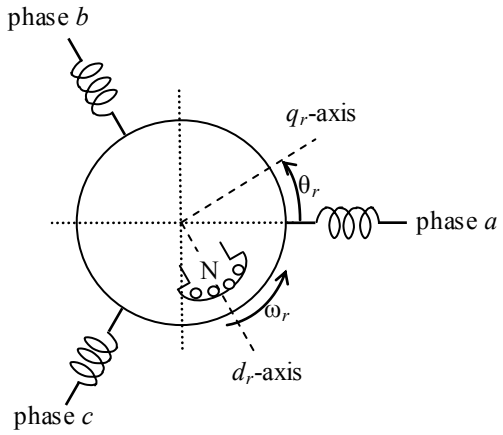

Figure 2-1. Schematic of a two-pole, three-phase PMSM with illustration of its conventions.

2.2.2 *Fundamentals of Reference Frame Theory*

It has been shown that the equations which describe the behaviour of AC machines contain time-varying coefficients due to the fact that some of the machine inductances are a function of the rotor displacement. Therefore, a conceptual frame of reference that rotates at certain angular velocity is used to convert the time-varying quantities to establish invariant inductances in the voltage, current and flux equations [71].

In addition to *abc* and $d_r q_r$ axes, a conceptual *dq* frame that rotates at a speed of ω is defined as shown in Figure 2-2. θ denotes the angle between *q* axis and stator *a* phase. The relationship between rotational speed and position can be represented as in (2.5).

$$\left.\begin{aligned} \frac{d\theta_r}{dt} - \theta_{r0} &= \omega_r \\ \frac{d\theta}{dt} - \theta_0 &= \omega \end{aligned}\right\} \tag{2.5}$$

θ_{r0} and θ_0 are the initial position of $d_r q_r$ axes and *dq* frame respectively. $\theta_{r0} = \theta_0 = 0$ is assumed in this work in work in order to simplify the analysis.

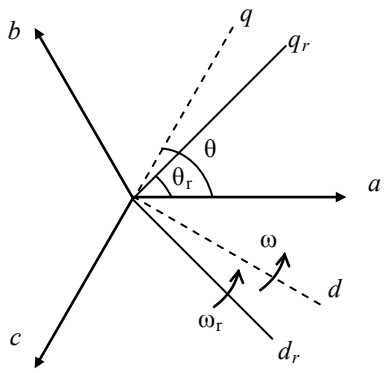

Figure 2-2. Illustration of the angular relationships for reference frame theory.

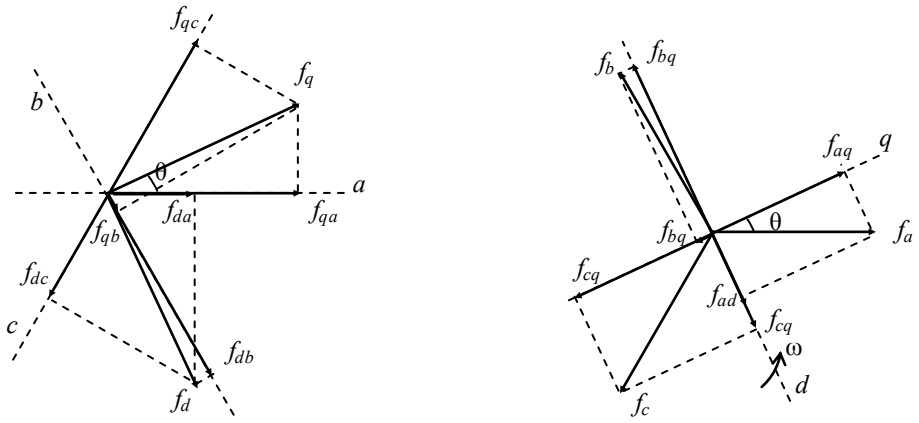

(a) (b)

Figure 2-3. Reference frame conversion. (a) *abc* to arbitrary reference frame. (b) Arbitrary reference frame to *abc*.

If the *dq* frame is chosen to rotate at the same speed as the rotor of the machine, i.e. $\omega = \omega_r$, then it is called the rotor reference frame. If the *dq* frame is chosen to rotate at the synchronous speed of the utility supply, i.e. $\omega = \omega_s$, then it is called the synchronously rotating reference frame. If the *dq* frame is stationary, i.e. $\omega = 0$, then it is called the stationary reference frame. Other than the aforementioned conditions, if the reference frame rotates at any other speed, it is called an arbitrary reference frame.

In order to convert variables in the *abc* frame to the arbitrary reference frame, the orthogonal projections of the *abc* frame quantities on *dq* frame need to be calculated as shown Figure 2-3(a) (note that the vectors are drawn for demonstration purpose and the length of the vector does not represent that of actual three-phase balanced quantities). Therefore the variables in *dq* frame can be written as:

$$\left.\begin{aligned} f_d &= a\left(f_{ad} + f_{bd} + f_{cd}\right) = a\left[f_a \sin\theta + f_b \sin\left(\theta - \frac{2\pi}{3}\right) + f_c \sin\left(\theta + \frac{2\pi}{3}\right)\right] \\ f_q &= a\left(f_{aq} + f_{bq} + f_{cq}\right) = a\left[f_a \cos\theta + f_b \cos\left(\theta - \frac{2\pi}{3}\right) + f_c \cos\left(\theta + \frac{2\pi}{3}\right)\right] \end{aligned}\right\} \tag{2.6}$$

where f_a , f_b , f_c, represent the voltage, current or flux in *abc* frame and f_d and f_q represent the quantities in the *dq* frame. Ratio *a* is a scale factor for the conversion.

Consider a set of balanced three-phase quantities f_a, f_b and f_c which are written as:

$$\left.\begin{aligned} f_a &= \hat{f}\sin\theta_s \\ f_b &= \hat{f}\sin\left(\theta_s - \frac{2\pi}{3}\right) \\ f_c &= \hat{f}\sin\left(\theta_s + \frac{2\pi}{3}\right) \end{aligned}\right\} \tag{2.7}$$

where $\hat{f}$ represents the peak value and $\theta_s = \omega_s t$ represents the phase of the defined signal.

From (2.6) and (2.7), f_d and f_q can be found:

$$\left.\begin{aligned} f_d &= \frac{3}{2}a\hat{f}\cos\left(\theta_s - \theta\right) \\ f_q &= \frac{3}{2}a\hat{f}\sin\left(\theta_s - \theta\right) \end{aligned}\right\} \tag{2.8}$$

The ratio for conversion is set as $\frac{2}{3}$ to keep the amplitude of the *abc* and *dq* quantities the same. Similarly, in order to convert the variables from *dq* frame back to *abc* frame, the following set of equations is used:

$$\left.\begin{aligned} f_a &= b\left(f_{da} + f_{qa}\right) = b\left[f_d\sin\theta + f_q\cos\theta\right] \\ f_b &= b\left(f_{db} + f_{qb}\right) = b\left[f_d\sin\left(\theta - \frac{2\pi}{3}\right) + f_q\cos\left(\theta - \frac{2\pi}{3}\right)\right] \\ f_c &= b\left(f_{dc} + f_{qc}\right) = b\left[f_d\sin\left(\theta + \frac{2\pi}{3}\right) + f_q\cos\left(\theta + \frac{2\pi}{3}\right)\right] \end{aligned}\right\} \tag{2.9}$$

where b is the scale factor from *dq* frame to *abc* frame.

Based on (2.8) into (2.9), the three-phase balanced quantities in *abc* frame are:

$$\left.\begin{aligned} f_a &= b\hat{f}\sin\theta_s \\ f_b &= b\hat{f}\sin\left(\theta_s - \frac{2\pi}{3}\right) \\ f_c &= b\hat{f}\sin\left(\theta_s + \frac{2\pi}{3}\right) \end{aligned}\right\} \tag{2.10}$$

To ensure the conversion does not change the amplitude of f, b=1.

Therefore the transformation from *abc* frame to *dq* frame in matrix form is:

$$\begin{bmatrix} f_d \\ f_q \end{bmatrix} = M^{abc-dq}\begin{bmatrix} f_a \\ f_b \\ f_c \end{bmatrix} \tag{2.11}$$

where $M^{abc-dq} = \frac{2}{3}\begin{bmatrix} \sin\theta & \sin\left(\theta - \frac{2\pi}{3}\right) & \sin\left(\theta + \frac{2\pi}{3}\right) \\ \cos\theta & \cos\left(\theta - \frac{2\pi}{3}\right) & \cos\left(\theta + \frac{2\pi}{3}\right) \end{bmatrix}$

Similarly, the matrix form for transformation from *dq* frame to *abc* frame is:

$$\begin{bmatrix} f_a \\ f_b \\ f_c \end{bmatrix} = M^{dq-abc}\begin{bmatrix} f_d \\ f_q \end{bmatrix} \tag{2.12}$$

where $M^{dq-abc} = \begin{bmatrix} \sin\theta & \cos\theta \\ \sin\left(\theta - \frac{2\pi}{3}\right) & \cos\left(\theta - \frac{2\pi}{3}\right) \\ \sin\left(\theta + \frac{2\pi}{3}\right) & \cos\left(\theta + \frac{2\pi}{3}\right) \end{bmatrix}$.

Unbalanced phase conditions are not considered in this work and hence the zero sequence components are not discussed here [71].

2.2.3 dq Equivalent Circuit Model for PMSMs

Based on the established stator *abc* phase flux linkages in (2.3) and the transformation from *abc* frame to *dq* reference frame in (2.11), the flux linkage in *d*- and *q*-axis can be calculated as:

$$\left.\begin{aligned}\lambda_{ds} &= \left(L_{ls}+L_A\right)i_{ds}+\frac{1}{2}L_A i_{ds} \\ &\quad +\frac{3}{2}L_B\left[i_{as}\sin\left(2\theta_r-\theta\right)+i_{bs}\sin\left(2\theta_r-\theta-\frac{2\pi}{3}\right)+i_{cs}\sin\left(2\theta_r-\theta+\frac{2\pi}{3}\right)\right]+\lambda_0^{'} \\ \lambda_{qs} &= \left(L_{ls}+L_A\right)i_{qs}+\frac{1}{2}L_A i_{qs} \\ &\quad -\frac{3}{2}L_B\left[i_{as}\cos\left(2\theta_r-\theta\right)+i_{bs}\cos\left(2\theta_r-\theta-\frac{2\pi}{3}\right)+i_{cs}\cos\left(2\theta_r-\theta+\frac{2\pi}{3}\right)\right]\end{aligned}\right\} \tag{2.13}$$

As seen from the equation, if $L_B = 0$, by converting to arbitrary reference frame, the relation between flux and current becomes independent of the rotor position. However, for salient machine, $L_B \neq 0$. Only when using the rotor reference frame i.e. $\theta = \theta_r$, the flux equations can be written as using the conversion matrix in (2.11):

$$\left.\begin{aligned}\lambda_{ds} &= L_{ls}i_{ds}+\frac{3}{2}\left(L_A+L_B\right)i_{ds}+\lambda_0^{'} \\ \lambda_{qs} &= L_{ls}i_{qs}+\frac{3}{2}\left(L_A-L_B\right)i_{qs}\end{aligned}\right\} \tag{2.14}$$

By converting to the rotor reference frame, the flux equation can be expressed with invariant inductances L_{ls}, L_{md} and L_{mq}, which are defined as leakage inductance, *d*-axis magnetizing inductance and *q*-axis magnetizing inductance respectively.

$$\left.\begin{aligned}L_{md} &= \frac{3}{2}\left(L_A+L_B\right) \\ L_{mq} &= \frac{3}{2}\left(L_A-L_B\right)\end{aligned}\right\} \tag{2.15}$$

For PMSMs *d*- and *q*-axis synchronous inductances are defined as:

$$\left.\begin{aligned}L_{ds} &= L_{ls}+L_{md} \\ L_{qs} &= L_{ls}+L_{mq}\end{aligned}\right\} \tag{2.16}$$

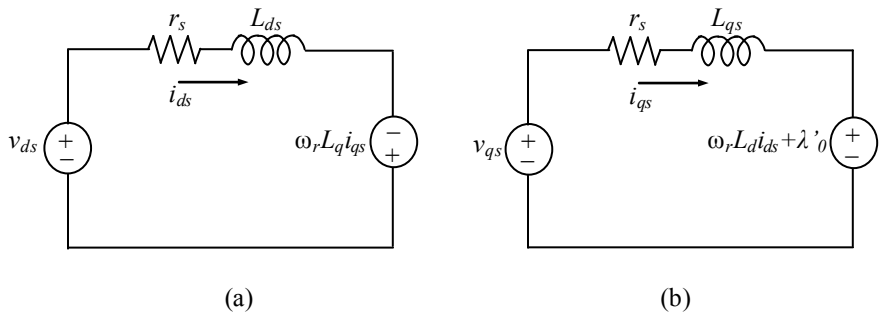

(a) (b)

Figure 2-4. *d*- and *q*-axis equivalent circuit model of a PMSM in the rotor reference frame. (a) *d*-axis. (b) *q*-axis.

Therefore, the flux linkage expression can be simplified as:

$$\left.\begin{aligned} \lambda_{ds} &= L_{ds} i_{ds} + \lambda'_0 \\ \lambda_{qs} &= L_{qs} i_{qs} \end{aligned}\right\} \tag{2.17}$$

The voltage equations in *dq* frame can be calculated using (2.4) and (2.11):

$$\left.\begin{aligned} v_{ds} &= r_s i_{ds} + \frac{d\lambda_{ds}}{dt} - \omega_r \lambda_{qs} \\ v_{qs} &= r_s i_{qs} + \frac{d\lambda_{qs}}{dt} + \omega_r \lambda_{ds} \end{aligned}\right\} \tag{2.18}$$

Using (2.17) in (2.18), the equivalent circuit can be developed as in Figure 2-4 and the stator terminal voltage in terms of current in *dq* reference frame can be expressed in matrix form as:

$$\begin{bmatrix} v_{ds} \\ v_{qs} \end{bmatrix} = \begin{bmatrix} r_s + pL_{ds} & -\omega_r L_{qs} \\ \omega_r L_{ds} & r_s + pL_{qs} \end{bmatrix} \begin{bmatrix} i_{ds} \\ i_{qs} \end{bmatrix} + \omega_r \begin{bmatrix} 0 \\ \lambda'_0 \end{bmatrix} \tag{2.19}$$

where p is the differential operator, d/dt.

The total power of the machine can be calculated with *abc* phase voltages and currents. Using the conversion matrix, total power can also be represented in terms of *dq* axis quantities as shown below.

$$P_e = v_{as} i_{as} + v_{bs} i_{bs} + v_{cs} i_{cs} = \frac{3}{2}\left(v_{qs} i_{qs} + v_{ds} i_{ds}\right) \tag{2.20}$$

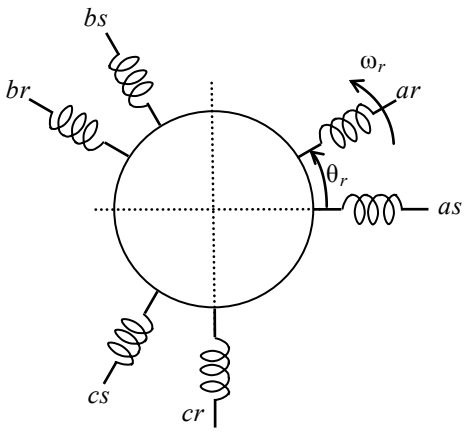

Figure 2-5. Two-pole, three-phase, wye-connected symmetrical induction machine.

The electromechanical torque developed in the machine is

$$T_e = \frac{3}{2}\frac{P}{2}\left[\lambda_0^{'} i_{qs} + \left(L_{ds} - L_{qs}\right) i_{ds} i_{qs}\right] \tag{2.21}$$

where P denotes the number of rotor poles.

2.2.4 dq Equivalent Circuit Model for Induction Machines

To obtain the equivalent circuit for the induction machine, the schematic of which is shown in Figure 2-5, the flux linkage equations can be established in *abc* frame [71] as follows:

$$\left.\begin{aligned}
\lambda_{as} &= L_{asas} i_{as} + L_{asbs} i_{bs} + L_{ascs} i_{cs} + L_{asar} i_{ar} + L_{asbr} i_{br} + L_{ascr} i_{cr} \\
\lambda_{bs} &= L_{bsas} i_{as} + L_{bsbs} i_{bs} + L_{bscs} i_{cs} + L_{bsar} i_{ar} + L_{bsbr} i_{br} + L_{bscr} i_{cr} \\
\lambda_{cs} &= L_{csas} i_{as} + L_{csbs} i_{bs} + L_{cscs} i_{cs} + L_{csar} i_{ar} + L_{csbr} i_{br} + L_{cscr} i_{cr} \\
\lambda_{ar} &= L_{aras} i_{as} + L_{arbs} i_{bs} + L_{arcs} i_{cs} + L_{arar} i_{ar} + L_{arbr} i_{br} + L_{arcr} i_{cr} \\
\lambda_{br} &= L_{bras} i_{as} + L_{brbs} i_{bs} + L_{brcs} i_{cs} + L_{brar} i_{ar} + L_{brbr} i_{br} + L_{brcr} i_{cr} \\
\lambda_{cr} &= L_{cras} i_{as} + L_{crbs} i_{bs} + L_{crcs} i_{cs} + L_{crar} i_{ar} + L_{crbr} i_{br} + L_{crcr} i_{cr}
\end{aligned}\right\} \tag{2.22}$$

where λ_{as}, λ_{bs} and λ_{cs} denote the flux linkages in stator phases. λ_{ar}, λ_{br} and λ_{cr} denote the flux linkages in rotor phases. i_{as}, i_{bs} and i_{cs} represent the phase currents in stator and i_{ar}, i_{br} and i_{cr} represent the phase currents in the rotor. The inductances in the equation

represent the self-inductances of the stator and rotor phases and the mutual inductances between difference phases of the stator and rotor [71].

The transformation matrix in (2.11) is used to convert the flux linkage into rotor reference frame. Note that because an induction machine is non-salient, it is not mandatory to use the rotor reference frame. The equivalent circuit of the machine can be developed in an arbitrary reference frame. Since in this study, the damper is added into the PMSM, which requires the rotor reference frame, the same frame is used to describe the induction machine to stay consistent. The flux linkage in an induction machine in the rotor reference frame is described as:

$$\left.\begin{aligned} \lambda_{ds} &= L_s i_{ds} + L_m i_{dr} \\ \lambda_{qs} &= L_s i_{qs} + L_m i_{dr} \\ \lambda'_{dr} &= L'_r i'_{dr} + L_m i_{ds} \\ \lambda'_{qr} &= L'_r i'_{qr} + L_m i_{qs} \end{aligned}\right\} \tag{2.23}$$

where L_m is the stator magnetizing inductance. λ'_{dr} and λ'_{qr} represent the flux of the rotor referred to the stator side. i'_{dr} and i'_{qr} represent the current of the rotor referred to the stator side. $L_s = L_{ls} + L_m$ is the stator inductance and $L'_r = L'_{lr} + L_m$ is the rotor inductance referred to the stator side.

The stator voltages in the *abc* frame in terms of flux linkage have been presented in (2.4), the rotor terminal voltages referred to the stator side are:

$$\left.\begin{aligned} v'_{ar} &= r'_r i'_{ar} + \frac{d\lambda'_{ar}}{dt} \\ v'_{br} &= r'_r i'_{br} + \frac{d\lambda'_{br}}{dt} \\ v'_{cr} &= r'_r i'_{cr} + \frac{d\lambda'_{cr}}{dt} \end{aligned}\right\} \tag{2.24}$$

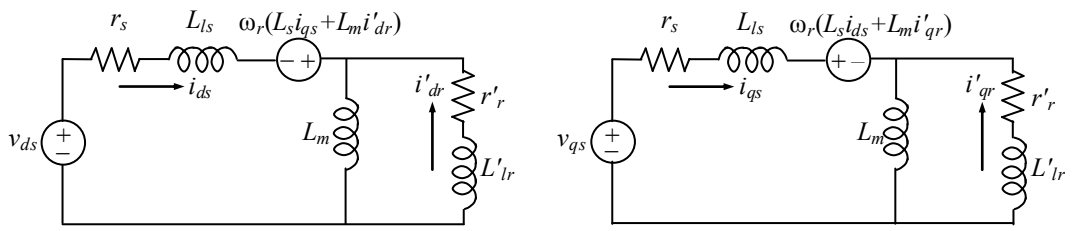

Figure 2-6. *d*- and *q*-axis equivalent circuit model of a squirrel cage IM in the rotor reference frame. (a) *d*-axis. (b) *q*-axis.

For squirrel cage induction machine, rotor bars are shorted, and therefore, $v'_{dr} = v'_{qr} = 0$. Combining (2.4), (2.23) and (2.24), the voltage in rotor reference frame in matrix form is as follows:

$$\begin{bmatrix} v_{ds} \\ v_{qs} \\ 0 \\ 0 \end{bmatrix} = \begin{bmatrix} r_s + L_s p & -\omega_r L_s & L_m p & -\omega_r L_m \\ \omega_r L_s & r_s + pL_s & \omega_r L_m & L_s p \\ L_m p & 0 & r'_r + L_r' p & 0 \\ 0 & L_m p & 0 & r'_r + L_r' p \end{bmatrix} \begin{bmatrix} i_{ds} \\ i_{qs} \\ i'_{dr} \\ i'_{qr} \end{bmatrix} \tag{2.25}$$

The equivalent circuit can be developed based on (2.25) as shown in Figure 2-6.

The electromechanical torque developed in an induction machine can be calculated as follows:

$$T_e = \frac{3}{2}\frac{P}{2} L_m \left(i_{qs} i'_{dr} - i_{ds} i'_{qr} \right) \tag{2.26}$$

2.2.5 Dynamic Model for a PMSM with Damper Bars

The schematic diagram of a PMSM with a damper is shown in Figure 2-7. The equivalent circuits of the machine, as shown in Figure 2-8, can be represented in a way similar to a conventional three-phase PMSM and an induction machine based on rotor reference frame. The voltage equations can be written as in (2.27), and the mechanical equations of the motor is represented in (2.28), (2.29) and (2.30). The first term of the total electromagnetic torque (T_e) on the right hand side of (2.29) represents the component arising out of 'synchronous machine' action due to permanent magnet and saliencies

(T_{epm}) and the second term on the right hand side of (2.29) represents the component arising out of 'induction machine' action due to the rotor cages ($T_{edamper}$).

$$\begin{bmatrix} v_{ds} \\ v_{qs} \\ 0 \\ 0 \end{bmatrix} = \begin{bmatrix} r_s + L_{ds}p & -\omega_r L_{qs} & L_{md}p & -\omega_r L_{mq} \\ \omega_r L_{ds} & r_s + L_{qs}p & \omega_r L_{md} & L_{mq}p \\ L_{md}p & 0 & r'_{kd} + L'_{kd}p & 0 \\ 0 & L_{mq}p & 0 & r'_{kq} + L'_{kq}p \end{bmatrix} \begin{bmatrix} i_{ds} \\ i_{qs} \\ i'_{kd} \\ i'_{kq} \end{bmatrix} + \omega_r \lambda'_0 \begin{bmatrix} 0 \\ 1 \\ 0 \\ 0 \end{bmatrix} \tag{2.27}$$

where v_{ds} and v_{qs} are the stator terminal voltages, i_{ds} and i_{qs} are the stator currents, i'_{kd} and i'_{kq} are the damper currents referred to stator side, r'_{kd} and r'_{kq} are the damper resistances referred to stator side in the d- and q-axis respectively. r_s is the stator resistance. $L_{ds} = L_{ls} + L_{md}$ and $L_{qs} = L_{ls} + L_{mq}$ are d- and q-axis synchronous inductances. L_{ls} is the stator leakage inductance. L_{md} and L_{mq} are the magnetizing inductances in d- and q-axis. $L'_{kd} = L'_{lkd} + L_{md}$ and $L'_{kq} = L'_{lkq} + L_{mq}$ are the damper inductances. L'_{lkd} and L'_{lkq} are the d-axis and q-axis leakage inductances, respectively, of damper referred to stator side. λ'_0 is the PM flux linkage referred to stator side.

$$p\omega_r = \left(P/2J\right)\left(T_e - T_L\right) \tag{2.28}$$

$$T_e = 3P/4\left[\lambda'_0 i_{qs} + i_{ds} i_{qs}\left(L_{ds} - L_{qs}\right)\right] + 3P/4\left[L_{md} i'_{kd} i_{qs} - L_{mq} i'_{kq} i_{ds}\right] \tag{2.29}$$

$$p\theta_r = \omega_r \tag{2.30}$$

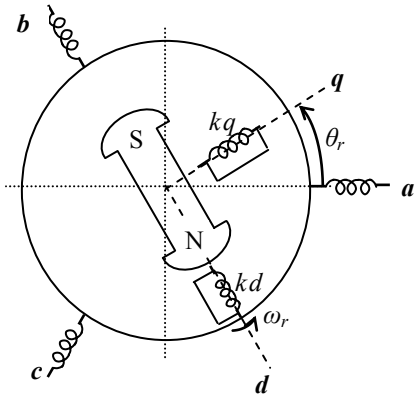

Figure 2-7. Winding schematics of a three-phase PMSM with a damper demonstrating the winding positions, electrical rotor position and the dq rotor reference frame.

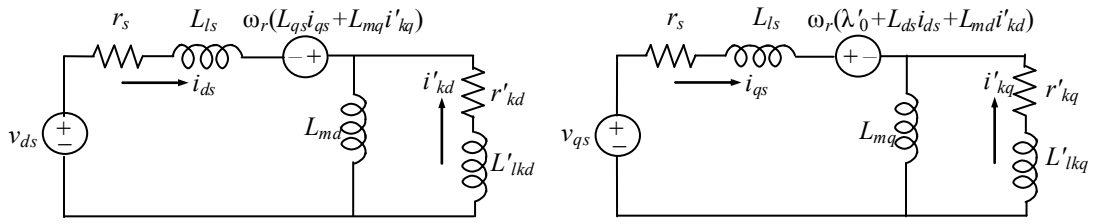

Figure 2-8. *d*-axis and *q*-axis equivalent circuit model of a PMSM with a damper in the rotor reference frame. (a) *d*-axis. (b) *q*-axis.

2.3 Parameter Determination of a PMSM with a Damper

Accurate equivalent circuit parameter estimation of the machine is of paramount importance as a reliable dynamic model of the machine has to be developed in order to design for, analyze and predict performance under varying loads and/or commanded speed. Parameter determination of this type of machine is an engineering challenge due to the complex rotor architecture consisting of permanent magnets and squirrel-cage rotor bars.

The experiments have been conducted on two machines, the ratings of which are presented in Appendix A. Machine I, as shown in Figure 2-9(a), is a PMSM with a symmetrical squirrel cage damper for starting purposes. Machine II as shown in Figure 2-9(b) is a wound-field rotor synchronous machine with an unsymmetrical damper (different damper parameters along *d* and *q* axes) for both starting and stability performance. Note that if the field current of the synchronous machine is set at a constant value during the operation, the machine may be conceptually considered as a PMSM.

2.3.1 DC Test

The stator resistance r_s can be determined through DC Test as presented in [72]. DC voltage is applied to the stator windings of the test machines and the voltage across the windings and the current through the windings are measured. Because the current is not alternating, the induced voltage is zero and there is no voltage drop across the inductances.

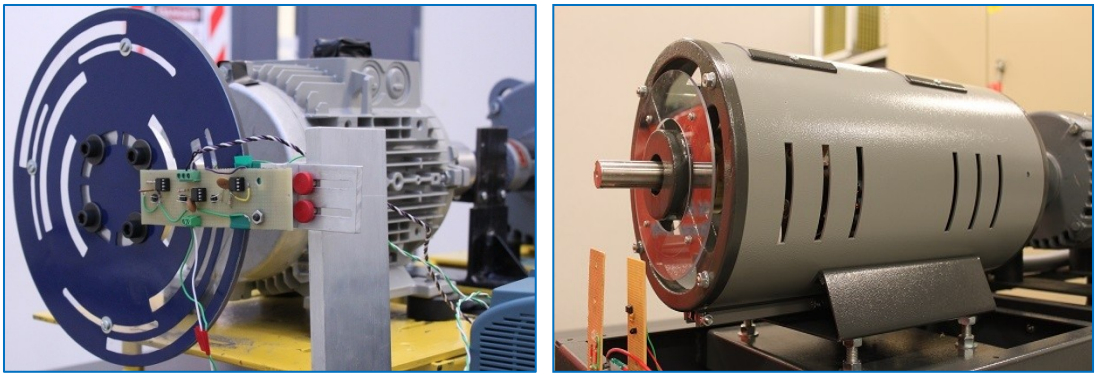

Figure 2-9. Laboratory machines with a damper for parameter estimation experimentation. (a) Machine I: line-start PMSM. (b) Machine II: synchronous machine with a damper.

TABLE 2-1. EXPERIMENT TEST DATA OF DC TEST ON MACHINE I & II.

Machine#	Test #	V_{DC}	I_{DC}	R_s
I	1	3.526	3.042	0.5795
	2	4.129	3.559	0.5801
	3	4.799	4.133	0.5805
			Average value:	0.58
II	1	1.93	1.57	0.6146
	2	2.94	2.39	0.6150
	3	4.32	3.5	0.6171
			Average value:	0.62

The stator resistance can be calculated as:

$$r_s = \frac{V_{DC}}{2I_{DC}} \tag{2.31}$$

where V_{DC} and I_{DC} denote the measured DC voltage and current respectively.

The results of DC tests conducted on machine I and II are presented in Table 2-1 [64]. Note that only three sets of test results are presented here, however, the average is taken based on a large number of tests. The value of r_s is not completely accurate with DC test, because it neglects the skin effect that occurs when an AC voltage is applied to the windings [73]. More details concerning correction of stator resistance can be found in the single-phase test proposed further in this study.

2.3.2 *Open Circuit Test*

The flux linkage created by the PMs referred to the stator side, λ_0' can be measured using a setup which is similar to that used to obtain open-circuit characteristics for synchronous machines [72]. The test machine, with its stator terminals kept open, is coupled with a DC motor as a prime mover. An induced voltage will be generated in the stator of the test machine and the electrical frequency of the stator is equal to the electrical velocity of the rotor, i.e. $\omega_s = \omega_r$. Therefore, there is no induced current through the rotor bars; the equivalent circuit of the test machine is the same as a regular PMSM as in Figure 2-4. Since the stator is kept open, there is no current through the stator windings. The *d*- and *q*-axis voltage under this condition is:

$$\left.\begin{aligned} v_{ds} &= 0 \\ v_{qs} &= \omega_r \lambda_0' \end{aligned}\right\} \tag{2.32}$$

The mechanical speed and terminal voltage of the test machine can be measured, and the relation between v_{qs} and terminal voltage using Park's transformation has been given in (2.8). Therefore, the flux linkage of PMs referred to the stator side is:

$$\lambda_0' = \frac{2}{P}\frac{30}{\pi n_m}\frac{\hat{V}_{ab}}{\sqrt{3}} \tag{2.33}$$

where n_m is the mechanical speed of the rotor in r/min and $\hat{V}_{ab}$ is the peak value of the line voltage.

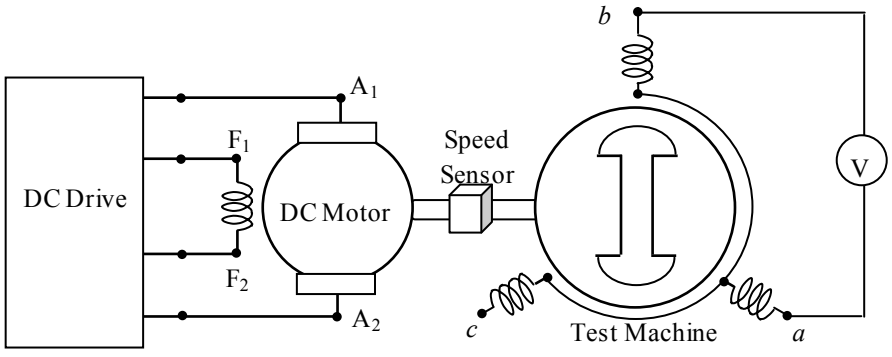

Figure 2-10. Schematic block diagram of the experimental setup for open circuit test.

TABLE 2-2. EXPERIMENT TEST DATA OF DC TEST ON MACHINE I AND II.

Machine #	Test #	$\hat{V}_{ab}$	n_m	λ'_0
I	1	63.4	855.3	0.2891
	2	94.1	1269	0.2892
	3	104	1399.2	0.2899
			Average value:	0.289
II	1	147.7	835.8	0.4874
	2	227.3	1296	0.4837
	3	315.9	1805.1	0.4828
			Average value:	0.485

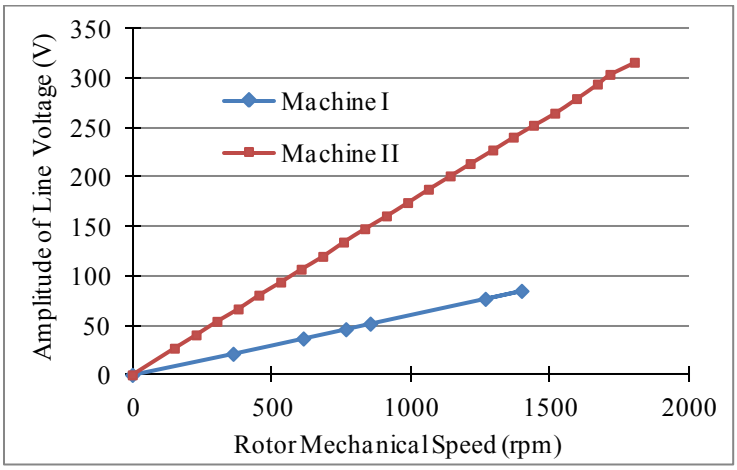

Figure 2-11. Measurement of rotor mechanical speed versus terminal voltage of Machine I and Machine II.

2.3.3 Synchronous Speed Loading Test

In order to measure the *d*- and *q*-axis synchronous inductances (L_{ds} and L_{qs}), a rotor position sensor has been developed, which yields on-line information of the operating torque angle (δ). It consists of three infrared emitter-detector diode pairs and a gray-coded disk as shown in Figure 2-9(a). This position sensor is mounted on the motor shaft (rotor) in such a way that it yields a binary signal, with a positive edge that coincides with the positive zero-crossing instant of the induced EMF *E* of phase *a* of the machine, when it is run by a prime-mover at any speed [64]. This is ensured by running the machine as a generator at no load so that the induced EMF appears at the machine terminals. Afterwards, when the same machine is run as a motor at steady state under a particular load at synchronous speed as illustrated in Figure 2-12, the angular difference between the zero crossing instant of the applied line voltage and the instant of the positive edge of

the position sensor signal, read through an oscilloscope, provides the torque angle. The input power factor angle (θ) for a particular operating condition has also been experimentally obtained from applied voltage (V_t) and stator current (I_{ph}) waveforms. Figure 2-13 shows the measured voltage, current and sensor signal waveforms under a typical steady state condition [64].

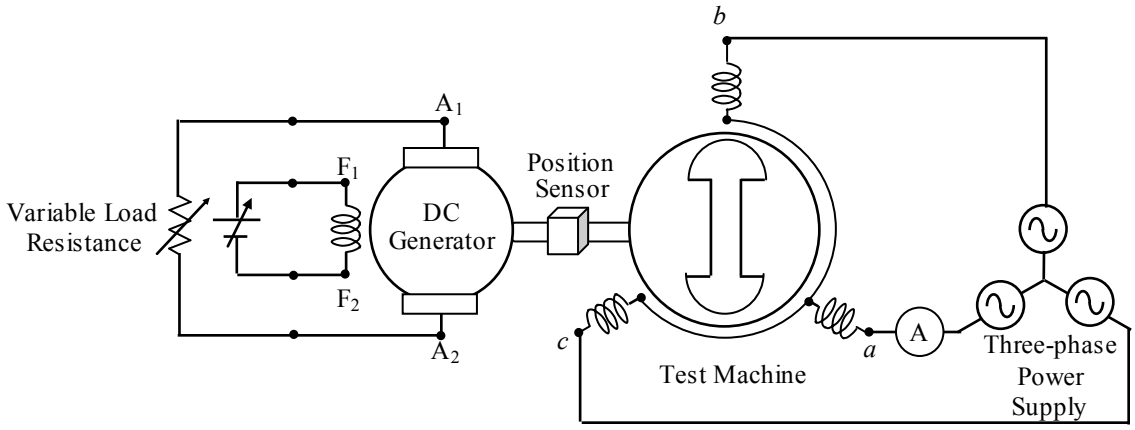

Figure 2-12. Schematic block diagram of the experimental setup for synchronous speed loading test.

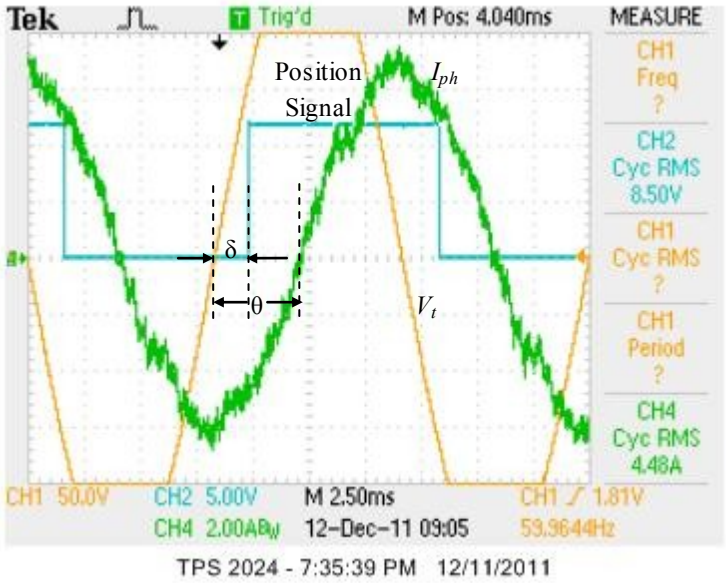

Figure 2-13. Measured voltage, current and position sensor output waveforms captured on an oscilloscope under a specific load at steady state.

Since at steady state, the test machines rotate at synchronous speed, there is no current in the rotor and therefore can be considered to operate as salient pole synchronous machines. A conventional phasor diagram of a salient pole synchronous machine shown in Figure 2-14 is employed to determine the *d*- and *q*-axis synchronous reactances (X_{ds} and X_{qs}). E, V_t and I_{ph} denote the rms value of the per phase induced voltage, terminal voltage and phase current. According to Figure 2-14(a), under the condition that the machine operates at lagging power factor and $\theta > \delta$, the stator current and voltage components can be expressed as:

$$\left.\begin{aligned} I_{ds} &= I_{ph}\sin(\theta-\delta) \\ I_{qs} &= I_{ph}\cos(\theta-\delta) \\ V_{qs} &= V_t\cos\delta \\ &= E + I_{ph}r_s\cos(\theta-\delta) + I_{ph}X_{ds}\sin(\theta-\delta) \\ &= E + I_{qs}r_s + I_{ds}X_{ds} \\ V_{ds} &= V_t\sin\delta \\ &= I_{ph}X_{qs}\cos(\theta-\delta) - I_{ph}r_s\sin(\theta-\delta) \\ &= I_{qs}X_{qs} - I_{ds}r_s \end{aligned}\right\} \quad (2.34)$$

Under the condition of lagging power factor and $\theta < \delta$ as shown in Figure 2-14(b), the expressions are:

$$\left.\begin{aligned} I_{ds} &= I_{ph}\sin(\delta-\theta),\ I_{qs} = I_{ph}\cos(\delta-\theta) \\ V_{qs} &= V_t\cos\delta \\ &= E + I_{ph}r_s\cos(\delta-\theta) - I_{ph}X_{ds}\sin(\delta-\theta) \\ &= E + I_{qs}r_s - I_{ds}X_{ds} \\ V_{ds} &= V_t\sin\delta \\ &= I_{ph}X_{qs}\cos(\delta-\theta) + I_{ph}r_s\sin(\delta-\theta) \\ &= I_{qs}X_{qs} + I_{ds}r_s \end{aligned}\right\} \quad (2.35)$$

Figure 2-14(c) represents the phasor diagram for a leading power factor angle.

$$\left.\begin{aligned} I_{ds} &= I_{ph}\sin(\delta+\theta),\ I_{qs} = I_{ph}\cos(\delta+\theta) \\ V_{qs} &= V_t\cos\delta \\ &= E + I_{ph}r_s\cos(\delta+\theta) - I_{ph}X_{ds}\sin(\delta+\theta) \\ &= E + I_{qs}r_s - I_{ds}X_{ds} \\ V_{ds} &= V_t\sin\delta \\ &= I_{ph}X_{qs}\cos(\delta+\theta) + I_{ph}r_s\sin(\delta+\theta) \\ &= I_{qs}X_{qs} + I_{ds}r_s \end{aligned}\right\} \tag{2.36}$$

Incorporating the above conditions, leading power factor angle, θ is taken as positive and lagging power factor angle is taken as negative, the synchronous reactances can be solved as:

$$\left.\begin{aligned} X_{ds} &= \frac{E + I_{qs}r_s - V_{qs}}{I_{ds}} \\ X_{qs} &= \frac{V_{ds} - I_{ds}r_s}{I_{qs}} \end{aligned}\right\} \tag{2.37}$$

where,
$$E = \omega_r\lambda_0^{'}$$
$$V_{ds} = V_t\sin\delta, V_{qs} = V_t\cos\delta \quad .$$
$$I_{ds} = I_{ph}\sin(\delta-\theta),\ I_{qs} = I_{ph}\cos(\delta-\theta)$$

As operating torque angle δ, input power factor angle θ, terminal phase voltage V_t, phase current I_{ph}, induced phase EMF E, and armature resistance r_s are all known at a particular steady state, the synchronous reactances can be computed. In order to verify the consistency of the results, the machines were operated under different applied voltages and different loadings. The values of the reactances for both the machines obtained from the trials shows acceptable precision in the results as seen from TABLE 2-3. Furthermore, the magnetizing characteristics can be determined using this method under different loading conditions as explained in [65]. It was shown that a model incorporating the measured magnetizing characteristics can predict the machine performance with higher accuracy than the original model.

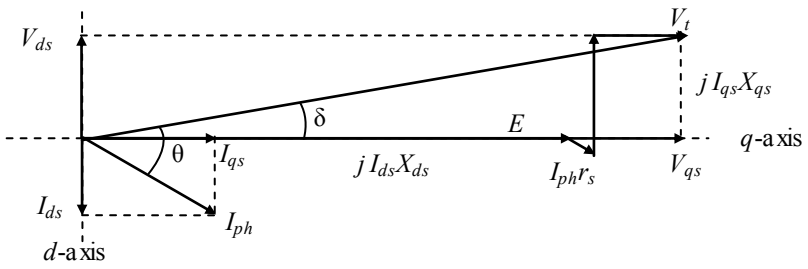

(a)

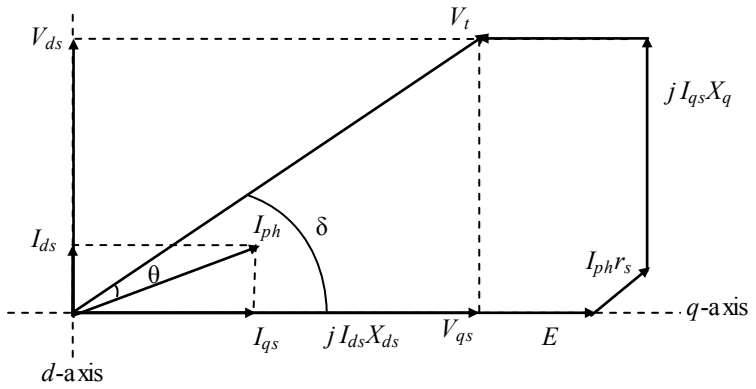

(b)

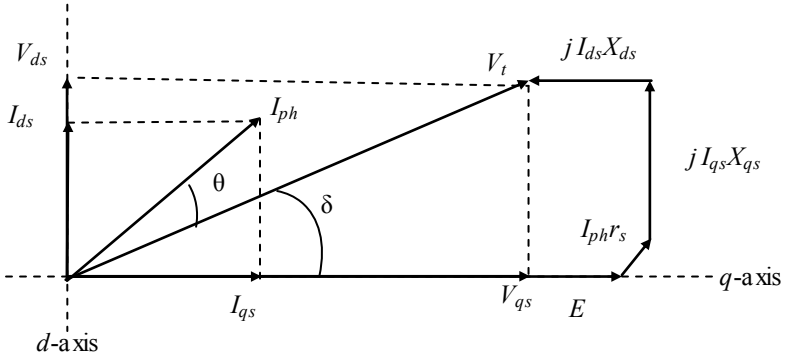

(c)

Figure 2-14. Phasor diagram of a salient pole PMSM. (a) Lagging power factor θ>δ. (b) Lagging power factor θ<δ. (c) Leading power factor.

TABLE 2-3. EXPERIMENTAL RESULTS TO OBTAIN D- AND Q-AXIS SYNCHRONOUS INDUCTANCE AT 60 HZ SUPPLY FREQUENCY

Machine	V_t (V)	I_t (A)	δ (°)	θ (°)	E_{ph}(V)	V_{ds} (V)	V_{qs} (V)	I_{ds} (A)	I_{qs} (A)	X_{ds}(Ω)	X_{qs}(Ω)
I	127.0	5.61	34.3	-75.0	76.5	71.5	104.9	3.66	4.25	7.08	17.34
		5.21	42.8	-55.7		86.3	93.2	1.16	5.08	11.73	17.13
	138.9	6.63	34.3	-77.4		78.3	114.7	4.50	4.87	7.84	16.88
		6.37	42.9	-64.3		94.4	101.6	2.32	5.93	9.27	16.68
II	99.6	3.12	10.6	45.0	129.9	18.4	97.9	2.58	1.75	12.62	9.52
		3.43	11.9	34.7		20.6	97.6	2.49	2.35	13.30	8.09
	117.0	4.36	16.87	4.11		33.96	111.96	1.56	4.07	12.74	8.10
		5.01	20.51	-0.51		40.98	109.58	1.71	4.71	13.23	8.47

2.3.4 Blocked Rotor Test

In order to obtain rotor leakage inductance and damper resistance, a blocked rotor test as conventionally performed on a three-phase induction motor [72] has been performed on the LSPMSM for a set of low three-phase voltages. Under a blocked rotor condition ($\omega_r = 0$), in the equivalent circuits of Figure 2-8, each dependant voltage source in the stator branch is considered as shorted. Also, as the operating voltage to establish rated current flow under a blocked rotor condition is much lower than its rated value, the flux in the machine is extremely low and hence the magnetizing branches of L_{md} and L_{mq} in Figure 2-8 can be treated as open circuited.

Therefore, each of the *d* and *q* equivalent circuits reduces to a series network consisting of two resistances (stator and cage) and two leakage inductances (stator and cage). The total resistance and total leakage reactance, R_{br} and X_{br} respectively, represent the input resistance and reactance, viewed from the stator side, under blocked conditions and are computed from the blocked rotor test results using (2.38) and (2.39).

$$R_{br} = \frac{V_{pk}}{I_{pk}} \cos\theta = r_s + r'_{kd(kq)} \tag{2.38}$$

$$X_{br} = \frac{V_{pk}}{I_{pk}} \sin\theta = X_{ls} + X'_{kd(kq)} \tag{2.39}$$

The tests are conducted for two different locked rotor positions; first the *d*-axis is aligned with the *a* phase, and next the *q*-axis is aligned with the *a* phase. Table 2-4 shows the measured input current I_{pk}, voltage V_{pk} and the power factor angle θ, as well as R_{br} and X_{br} calculated by using (2.38) and (2.39), respectively. The presented test results suggest that in either of the aforesaid aligned conditions, the input impedance of TABLE 2-4 are almost constant. The series parameters of the *d*-axis equivalent circuit and the *q*-axis equivalent circuit have therefore been treated same for the tested machine, i.e. $r'_{kd}=r'_{kq}$ and $L'_{lkd}=L'_{lkq}$. Therefore, it is further verified that the LSPMSM machine has a symmetrical squirrel cage in the rotor.

Given that r_s and R_{br} are known, r'_{kd} and r'_{kq} can be obtained using (2.38). After inspecting the rotor, by removing it from the stator with proper jigs and fixtures, the machine was found to belong to design class A. Therefore, the leakage inductances in the stator and rotor sides are considered same [72]. Hence, $X_{ls} = X'_{lkd} = X'_{lkq} = (1/2)X_{br}$.

Since the equivalent circuit reactance values X_{ds}, X_{qs}, X_{ls}, X'_{lkd} and X'_{lkq} are obtained experimentally, the corresponding inductance values can be calculated as the supply frequency is known to be 60 Hz. Once, L_{qs}, L_{ds} and L_{ls} are known, L_{md} and L_{mq} can be obtained easily [64].

TABLE 2-4. EXPERIMENTAL DATA OBTAINED FROM BLOCKED ROTOR TEST ON MACHINE I

Condition		I_{pk} (A)	V_{pk} (V)	θ (°)	R_{br}(Ω)	X_{br} (Ω)
d-axis aligned with a phase	#1	1.2	2.42	60	1.010	1.750
	#2	1.65	3.34	60	1.014	1.757
	#3	2.5	4.91	60	0.981	1.700
Average value:					1.012	1.754
q-axis aligned with *a* phase	#1	1.6	3.18	60	1.010	1.750
	#2	2	4.04	60	1.019	1.764
	#3	2.55	5.20	60	0.992	1.719
Average value:					1.007	1.740

2.3.5 *Single-phase AC Test*

A blocked rotor test is valid under the condition that the inductances of the magnetizing branches L_{md} and L_{mq} are higher than the leakage inductances of the damper L'_{lkd} and L'_{lkq}. Moreover, the rotor structure needs to be known in order to determine the machine class, to be able to determine L_{ls}, L'_{lkd} and L'_{lkq} from X_{br}. A single-phase AC test was proposed based on the fundamental magnetic circuit properties of the machine [66]. Referring to Section 2-1, the flux linkage of stator phase *a, b* and damper in the *d*- and *q*-axis for a PMSM with a damper are:

$$\left.\begin{aligned}
\lambda_{as} &= \left\{L_{ls} + L_A - L_B\cos 2\theta_r\right\} i_{as} + \left\{-\frac{1}{2}L_A - L_B\cos\left(2\theta_r - \frac{2\pi}{3}\right)\right\} i_{bs} \\
&\quad + \left\{-\frac{1}{2}L_A - L_B\cos\left(2\theta_r + \frac{2\pi}{3}\right)\right\} i_{cs} + L_{mq}\cos\theta_r i'_{kq} + \lambda'_0\sin\theta_r + L_{md}\sin\theta_r i'_{kd} \\
\lambda_{bs} &= \left\{-\frac{1}{2}L_A - L_B\cos\left(2\theta_r - \frac{2\pi}{3}\right)\right\} i_{as} + \left\{L_{ls} + L_A - L_B\cos\left(2\theta_r - \frac{4\pi}{3}\right)\right\} i_{bs} \\
&\quad + \left\{-\frac{1}{2}L_A - L_B\cos(2\theta_r + 2\pi)\right\} i_{cs} + L_{mq}\cos\left(\theta_r - \frac{2\pi}{3}\right) i'_{kq} + \lambda_0\,'\sin\left(\theta_r - \frac{2\pi}{3}\right) + L_{md}\sin\left(\theta_r - \frac{2\pi}{3}\right) i'_{kd} \\
\lambda'_{kd} &= \frac{2}{3}L_{md}\sin\theta_r i_{as} + \frac{2}{3}L_{md}\sin\left(\theta_r - \frac{2\pi}{3}\right) i_{bs} + \frac{2}{3}L_{md}\sin\left(\theta_r + \frac{2\pi}{3}\right) i_{cs} + \lambda'_0 + \left(L_{lkd}\,' + L_{md}\right) i'_{kd} \\
\lambda'_{kq} &= \frac{2}{3}L_{mq}\cos\theta_r i_{as} + \frac{2}{3}L_{mq}\cos\left(\theta_r - \frac{2\pi}{3}\right) i_{bs} + \frac{2}{3}L_{mq}\cos\left(\theta_r + \frac{2\pi}{3}\right) i_{cs} + \left(L_{lkq}\,' + L_{mq}\right) i'_{kq}
\end{aligned}\right\} \tag{2.40}$$

The motoring condition has been assumed positive here. In the proposed methodology for determining the electrical parameters of the dampers in the conventional *d*- and *q*-axis equivalent circuit, a controlled single-phase AC sinusoidal voltage is applied to the armature *a* phase winding with the rotor held stationary at certain strategic positions all throughout the test. When the rotor is held stationary, $p\theta_r = \omega_r = 0$. The tests are performed under two rotor positions similar to that of the blocked rotor test [66].

Condition 1: the *a* phase is aligned with *d*-axis (i.e. field axis), kept stationary and is excited with a single-phase sinusoidal AC voltage with the other two phases kept open (i.e. $\theta_r = 90^0$, i_b=i_c=0, $pi_b = pi_c = 0$). The voltages v_{an}, v_{bn} and current i_a are measured in steady state.

Therefore the voltage v'_{kq} can be calculated as:

$$
\begin{aligned}
0 &= r'_{kq} i'_{kq} + p\lambda'_{kq} \\
&= r'_{kq} i'_{kq} + \frac{2}{3} L_{mq} \cos\theta_r \, p i_a + \frac{2}{3} \omega L_{mq} \sin\theta_r \, p i_a + \left(L'_{lkq} + L_{mq} \right) p i'_{kq} \\
&= r'_{kq} i'_{kq} + \frac{2}{3} L_{mq} \cos\theta_r \, p i_a + \left(L'_{lkq} + L_{mq} \right) p i'_{kq}
\end{aligned} \tag{2.41}
$$

Because $\theta_r = 90°, \cos\theta_r = 0,$ the q-axis damper current must satisfy:

$$
0 = r'_{kq} i'_{kq} + \left(L'_{kq} + L_{mq} \right) p i'_{kq} \tag{2.42}
$$

As there is no external excitation in the q-axis damper at steady state, i'_{kq} is zero.

$$
\left.
\begin{aligned}
v_{as} &= r_s i_{as} + p\lambda_{as} \\
&= r_s i_a + \left(L_{ls} + \frac{2}{3} L_{md} \right) p i_{as} + L_{md} \, p i'_{kd} \\
v_{bs} &= r_s i_{bs} + p\lambda_{bs} \\
&= -\frac{1}{3} L_{md} \, p i_{as} - \frac{1}{2} L_{md} \, p i'_{kd} \\
0 = v_{kd}' &= r_{kd}' i_{kd}' + p\lambda_{kd} \\
&= r'_{kd} i'_{kd} + \frac{2}{3} L_{md} \, p i_{as} + \left(L'_{lkd} + L_{md} \right) p i'_{kd}
\end{aligned}
\right\} \tag{2.43}
$$

At steady state condition, the voltage can be expressed in terms of current, resistance and reactance at supply frequency. For phase a,

$$
V_{as} = r_s I_{as} + jX_{ls} I_{as} + \frac{2}{3} jX_{md} I_{as} + jX_{md} I'_{kd} \tag{2.44}
$$

where the phase of the current in phase a is considered as the reference phase with a phase angle zero, i.e. $I_{as} = | I_{as} | \angle 0°$. The angle measured between the supply voltage and the stator current in a phase is defined as θ, i.e. $V_{as} = | V_{as} | \angle \theta$.

For phase b,

$$
V_{bs} = -\frac{1}{3} jX_{md} I_{as} - \frac{1}{2} jX_{md} I'_{kd} \tag{2.45}
$$

The measured angle between the induced voltage in phase *b* and the current in phase *a* is defined as β, i.e. $V_{bs} = |V_{bs}| \angle \beta$. Then,

$$0 = r_{kd}^{'} I_{kd}^{'} + \frac{2}{3} j X_{md} I_{as} + j\left(X_{lkd}^{'} + X_{md}\right) I_{kd}^{'} \tag{2.46}$$

From (2.46), I_{kd} can be represented as:

$$I_{kd}^{'} = -\frac{\frac{2}{3} j X_{md} I_{as}}{r_{kd}^{'} + j X_{lkd}^{'} + j X_{md}} \tag{2.47}$$

Inserting (2.47) into (2.45) and (2.46) yields,

$$\left.\begin{aligned}
\frac{|V_{as}|}{|I_{as}|}\cos\theta &= r_s + \frac{\frac{2}{3} X_{md}^{\,2} I_a r_{kd}^{'}}{r_{kd}^{'\,2} + \left(X_{lkd}^{'} + X_{md}\right)^2} \\
\frac{|V_{bs}|}{|I_{as}|}\cos\beta &= -\frac{\frac{1}{3} X_{md}^{\,2} I_a r_{kd}^{'}}{r_{kd}^{'\,2} + \left(X_{kd}^{'} + X_{md}\right)^2} \\
\frac{|V_{as}|}{|I_{as}|}\sin\theta &= X_{ls} + \frac{2}{3} X_{md} - \frac{\frac{2}{3} X_{md}^{\,2}\left(X_{lkd}^{'} + X_{md}\right)}{r_{kd}^{'\,2} + \left(X_{lkd}^{'} + X_{md}\right)^2} \\
\frac{|V_{bs}|}{|I_{as}|}\sin\beta &= -\frac{1}{3} X_{md} + \frac{\frac{1}{3} X_{md}^{\,2}\left(X_{lkd}^{'} + X_{md}\right)}{r_{kd}^{'\,2} + \left(X_{lkd}^{'} + X_{md}\right)^2}
\end{aligned}\right\} \tag{2.48}$$

Therefore,

$$\left.\begin{aligned}
r_s &= \frac{|V_a|}{|I_a|}\cos\theta + 2\frac{|V_{bs}|}{|I_{as}|}\cos\beta \\
X_{ls} &= -\left(\frac{|V_{as}|}{|I_{as}|}\sin\theta + \frac{|V_{bs}|}{|I_{as}|}\sin\beta\right)
\end{aligned}\right\} \tag{2.49}$$

Since AC excitation is injected to the stator windings, the stator resistance r_s found using this method is the AC resistance and is more accurate for the model compared to the

standard DC test. Once X_{ls} is found, X_{md} and X_{mq} can easily be calculated using the X_{ds} and X_{qs} values from the synchronous speed loading test. Therefore, r'_{lkd} and X'_{lkd} can be found by solving either the first and third or second and fourth equations of (2.48).

Condition 2: Under operating conditions similar to that of condition 1, but now with the q-axis aligned with the a phase axis at stationary position $\theta_r = 0^o$. The voltage V_{an}, V_{bn} and current I_a are measured in steady state. The voltage along the d-axis in the damper can be written as,

$$0 = v'_{kd} = r'_{kd} i'_{kd} + p\psi_{kd} = r'_{kd} i'_{kd} + \frac{2}{3} L_{md} \sin\theta_r \, p i_{as} + \left(L_{lkd}' + L_{md} \right) p i'_{kd} \tag{2.50}$$

As $\theta_r = 0°$, $\sin\theta_r = 0$; the d-axis damper current must satisfy

$$0 = r'_{kd} i'_{kd} + \left(L'_{lkd} + L_{md} \right) p i'_{kd} \tag{2.51}$$

Therefore, under this alignment, $i'_{kd} = 0$.

The stator phase a, phase b and damper q-axis voltage can be calculated considering the given conditions:

$$\left.\begin{aligned} v_{as} &= r_s i_{as} + \left(L_{ls} + \frac{2}{3} L_{mq} \right) p i_{as} + L_{mq} p i'_{kq} \\ v_{bs} &= -\frac{1}{3} L_{mq} p i_{as} - \frac{1}{2} L_{mq} p i'_{kq} \\ 0 &= v'_{kq} = r'_{kq} i'_{kq} + \frac{2}{3} L_{mq} p i_{as} + \left(L'_{lkq} + L_{mq} \right) p i'_{kq} \end{aligned}\right\} \tag{2.52}$$

Now the measured terminal voltage is represented in terms of q-axis parameters, and hence the parameters in q-axis can be found using the above equations.

$$\left.\begin{aligned}
\frac{|V_a|}{|I_a|}\cos\theta &= r_s + \frac{\frac{2}{3}X_{md}{}^2 I_a r'_{kq}}{r'_{kq}{}^2 + \left(X'_{lkq} + X_{mq}\right)^2} \\
\frac{|V_b|}{|I_a|}\cos\beta &= -\frac{\frac{2}{3}X_{mq}{}^2 I_a r'_{kq}}{r'_{kq}{}^2 + \left(X'_{lkq} + X_{mq}\right)^2} \\
\frac{|V_a|}{|I_a|}\sin\theta &= X_{ls} + \frac{2}{3}X_{mq} - \frac{\frac{2}{3}X_{mq}{}^2\left(X'_{lkq} + X_{mq}\right)}{r'_{kq}{}^2 + \left(X'_{lkq} + X_{mq}\right)^2} \\
\frac{|V_b|}{|I_a|}\cos\beta &= -\frac{1}{3}X_{mq} + \frac{\frac{1}{3}X_{mq}{}^2\left(X'_{lkq} + X_{mq}\right)}{r'_{kq}{}^2 + \left(X'_{lkq} + X_{mq}\right)^2}
\end{aligned}\right\} \quad (2.53)$$

Similar to condition 1, r_s and X_{ls} can be calculated using (2.53). Since the stator does not have saliency, the value found from condition 1 should closely match with that from condition 2. r'_{lkq} and X'_{lkq} can be found by solving either the first and third or second and fourth equations of (2.53).

It can be seen from the waveforms measured using the oscilloscope as presented in Figure 2-15 that the stator *a* phase voltage is leading the current in phase *a*, i.e., $\theta>0$. Also, the voltage induced in phase *b* is lagging the current in phase *a*, i.e. $\beta<0$. The measured resistances and reactances shown in TABLE 2-5 is consistent as the supply voltage and current vary. Also, the measured values of the impedances in the *d* and *q*-axis are not equal, validating the observed unsymmetrical rotor structure of the machine.

TABLE 2-5. EXPERIMENTAL RESULTS OBTAINED FROM SINGLE-PHASE AC TEST OF MACHINE II

Condition		$\|V_{as}\|$ (V)	$\|V_{bs}\|$ (V)	$\|I_{as}\|$ (A)	θ (°)	β (°)	r_s (Ω)	X_{ls} (Ω)	$r'_{kd(kq)}$(Ω)	$X'_{lkd(kq)}$(Ω)
d-axis aligned with *a* phase	#1	11.77	4.61	6.30	61.32	-100.23	0.637	0.199	0.569	2.638
	#2	14.37	5.66	7.73	61.29	-100.18	0.633	0.189	0.567	2.641
	#3	15.31	6.05	8.30	61.38	-100.07	0.628	0.184	0.557	2.625
q-axis aligned with *a* phase	#1	17.75	7.86	5.42	67.53	-102.30	0.633	0.190	4.300	9.214
	#2	19.46	8.54	6.12	66.95	-102.38	0.646	0.200	3.807	8.474
	#3	22.04	9.65	7.23	66.28	-102.65	0.641	0.187	3.401	7.751

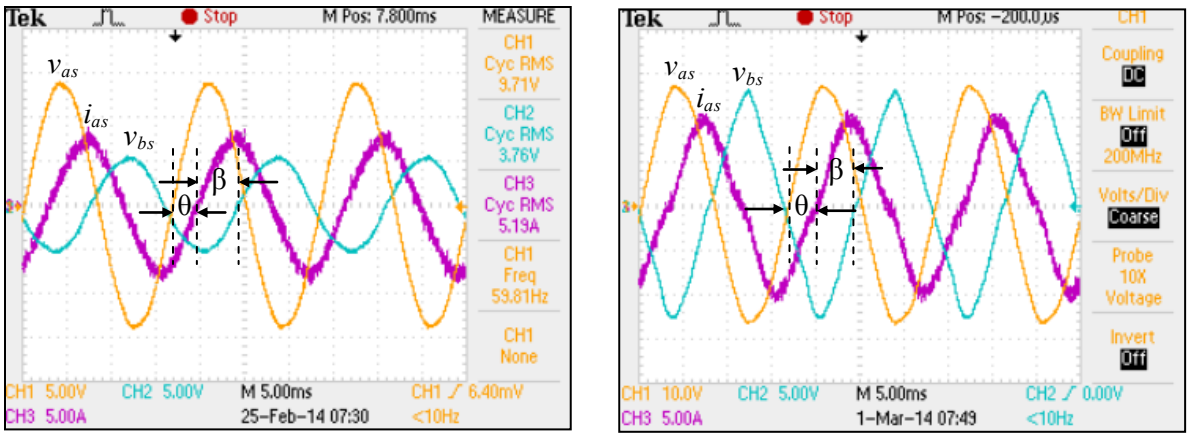

(a) (b)

Figure 2-15. Measure stator voltage of phase *a* and phase *b*, and current through phase *a*. (a) *d*-axis aligned with *a*, (b) *q*-axis aligned with *a*.

2.4 Model Verification under Steady State and Free Acceleration Conditions

In order to validate the above mentioned methodolgy, the determined parameters have been incorporated in a numeric model based on the two-axis machine model described in (2.27)-(2.30). The steady state and dynamic behaviour were obtained through numerical computation methods. Experiments were then performed to obtain similar dynamic and steady state operating conditions and the results are compared. Figure 2-16 shows the calculated and measured steady state stator current waveforms of machine I at a terminal voltage of 220 V and load torque of 4 Nm. From the figure, it is evident that the results obtained from the parameter assisted mathematical model of the machine are in close agreement with the experimentally captured values. Similar comparisons have been performed under a range of voltages and loads, and it was found that the calculated results match closely with that of the experimental values. The high frequency components obtained in the experimental current waveform are due to slot harmonics present in the induced EMF waveform of the laboratory machine [64].

Figure 2-17(a) and (b) show the calculated and measured stator current waveforms obtained under direct online (DOL) starting with 200 V at 60 Hz, applied at the instant of the peak of the *a* phase supply voltage waveform at no load to machine I. This was performed to establish the accuracy of the dynamic nature of the model, influenced mainly by satisfactorily accurate determination of the cage parameters. The huge inrush

current has been found to settle down to steady state in 2 seconds, as evident from both the presented waveforms, and therefore the measured damper parameters, particularly, are verified to be sufficiently accurate, to be used to represent the machine's electromechanical behaviour. The overshoots, undershoots and the settling time of the calculated and measured waveforms further verify the dynamic accuracy of the model.

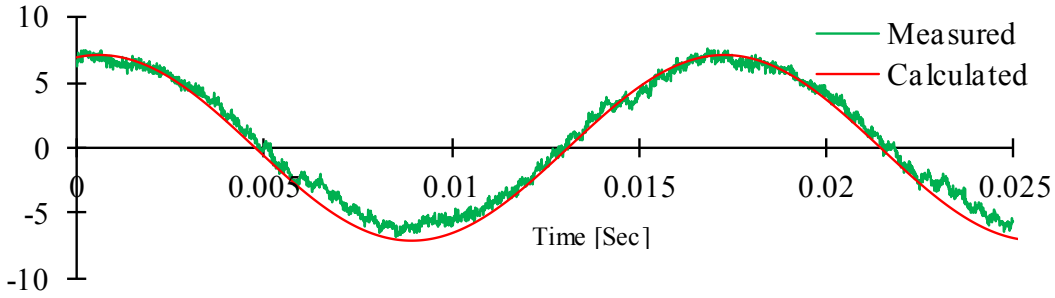

Figure 2-16. Calculated and measured stator current waveforms during steady state condition of the machine.

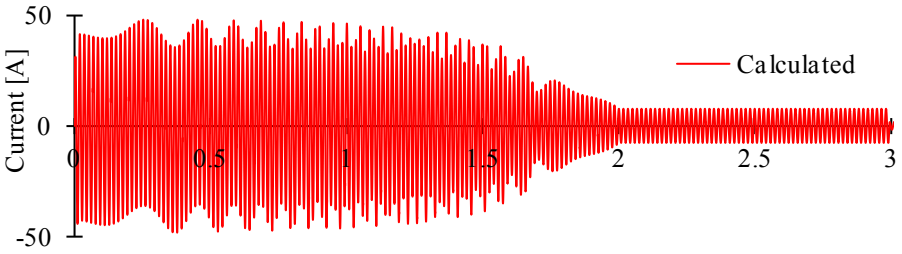

(a)

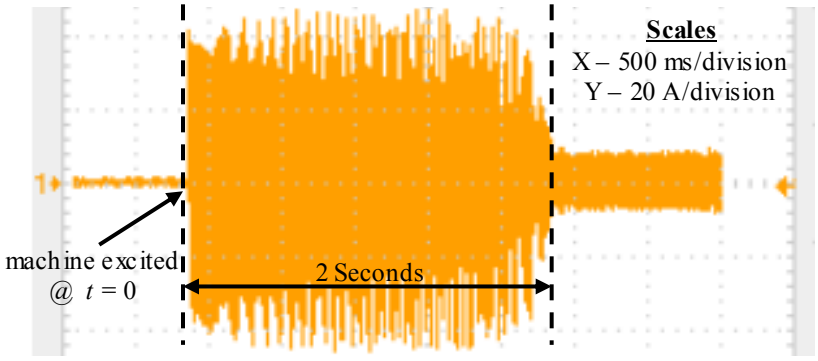

(b)

Figure 2-17. Calculated and measured stator current waveforms during starting (dynamic) condition of the machine. (a) Calculated. (b) Measured.

2.5 Performance Prediction and Analysis of a LSPMSM through Numerical Investigations

Once the parameters have been obtained and the two-axis model incorporating these equivalent circuit parameters has been validated, an exhaustive analysis of various steady state and dynamic operating conditions can be conducted. Figure 2-18(a) shows the calculated electromagnetic torque (T_e) and speed response of the model under DOL starting at 240 V, 60 Hz with a constant load torque of 10 Nm and then a step increment in load torque (T_l) of 5 Nm is introduced after 1 second. Figure 2-18(b) and Figure 2-18(c) show the constituent torque component arising from the 'synchronous' motor action (T_{epm}) and 'induction' motor action, respectively. The induction motor torque component ($T_{edamper}$) is found to vanish once synchronous speed is reached and is found to come into existence during transient stages of starting and/or when a step change in load torque is made. Studies of these constituent torque components would allow designers to design improved machines for faster starting capabilities under loads by apportioning the constituent torques properly.

Figure 2-19(a)-(b) present the calculated performance of the stator currents (two-axes components) and damper currents (two-axes components) when the machine is started DOL with a speed-invariant load torque of 10 Nm and then a step increment in load torque of 5 Nm is introduced after 1 second. Such current waveforms under different loading conditions would help the designers to predict the losses, improve the design and also to design the cage in a proper way capable of providing the requisite starting torque for an application. An insufficient torque from the cage action may prevent the motor from starting optimally with a particular load as this torque is opposed by the torque from synchronous motor action at starting. The waveforms are suggestive of the machine's steady state and transient performances under a large perturbation (starting) and a small perturbation (change in loading) [64].

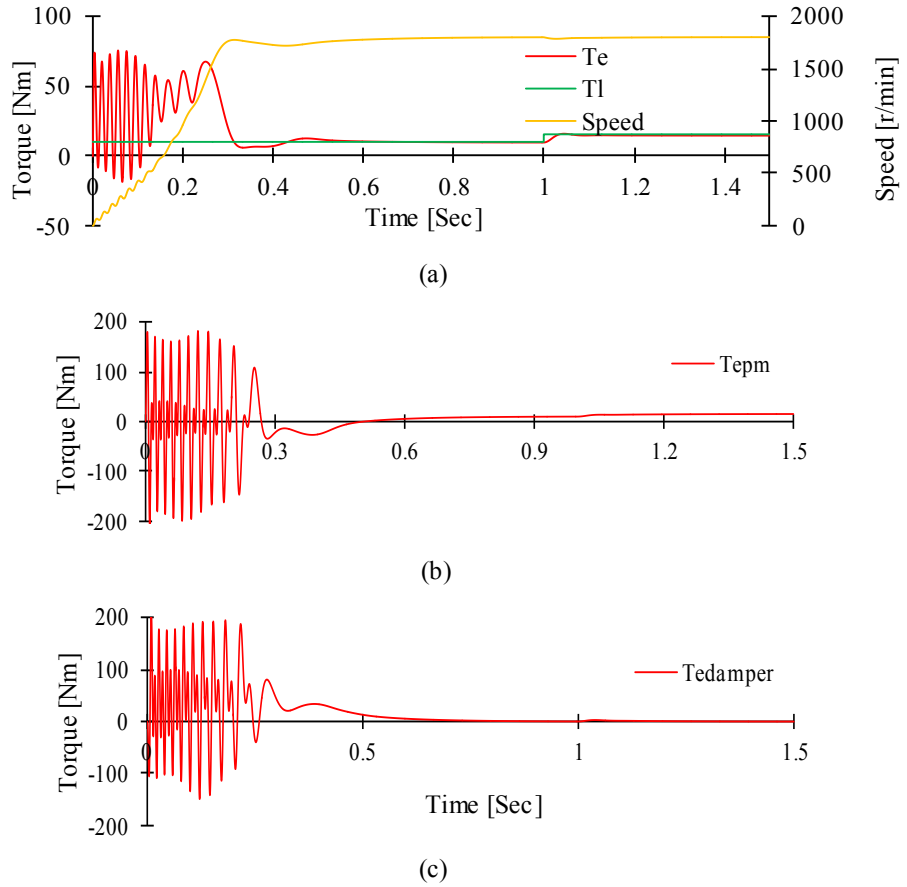

Figure 2-18. Calculated torque components. (a) Electromagnetic torque. (b) Torque from 'Synchronous' motor action. (c) Torque from 'Induction' motor action.

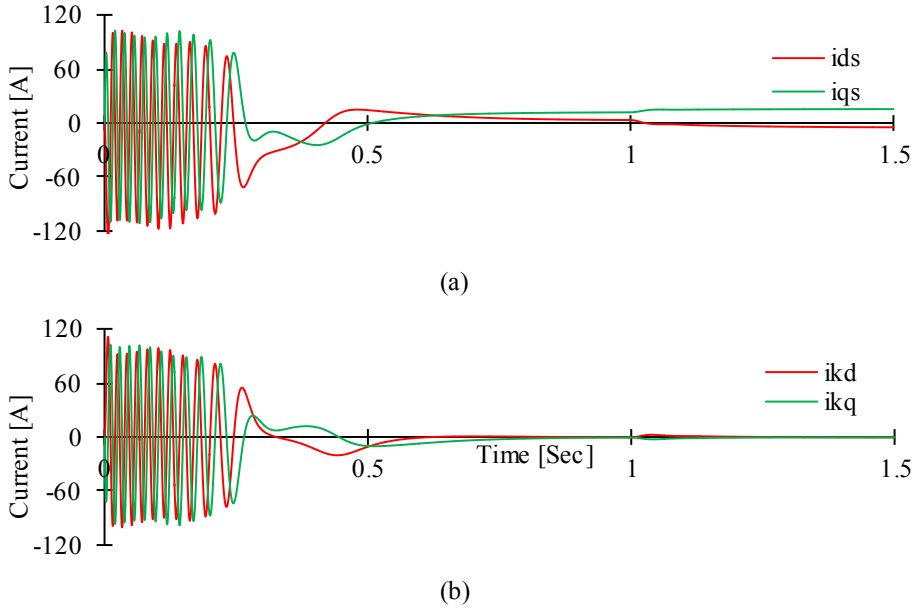

Figure 2-19. Calculated performance of the stator currents (two-axes components) and damper currents (two-axes components. (a) Stator currents. (b) Damper currents.

2.6 Study of the Magnetization Characteristics of a LSPMSM

This section puts an effort to elicit the performance of the machine through the machine models incorporating and not incorporating the magnetization characteristics. Model A incorporates the characteristics and Model B does not. Figure 2-20(a) and (b) show the speed, torque and current waveforms obtained through these models at the rated condition. Faster synchronization in the machine is obtained from the investigations through Model A when compared to that of B. Better starting performance through model A can be attributed towards less oscillations in torque and speed due to the lower slope of the saturation curve which limits the oscillations.

However, the torque and speed oscillations obtained through model B oscillate more because no limitation is offered by the unsaturated parameters and the linear characteristics. According to [74], the start-up performance of LSPMS motors benefits from a large magnetizing inductance whereas the synchronization capability is enhanced with a small magnetizing inductance.

This theory can be validated by the result shown in Figure 2-20(a) and (b). The start-up performance of the machine in model A is better than that of B because of the higher value of its magnetizing inductance at starting. However, as the machine reaches near synchronism, the value of the magnetizing inductances in model A is smaller than that of the constant values in model B and this results in faster synchronization of the machine in model A. Moreover, as seen in Figure 2-20(b) less energy is consumed from start to synchronization, if the magnetization characteristics are incorporated in model A. This also leads to reduced starting losses in the machine. Also, the starting current for the saturated model is a bit higher than that of the unsaturated model as expected.

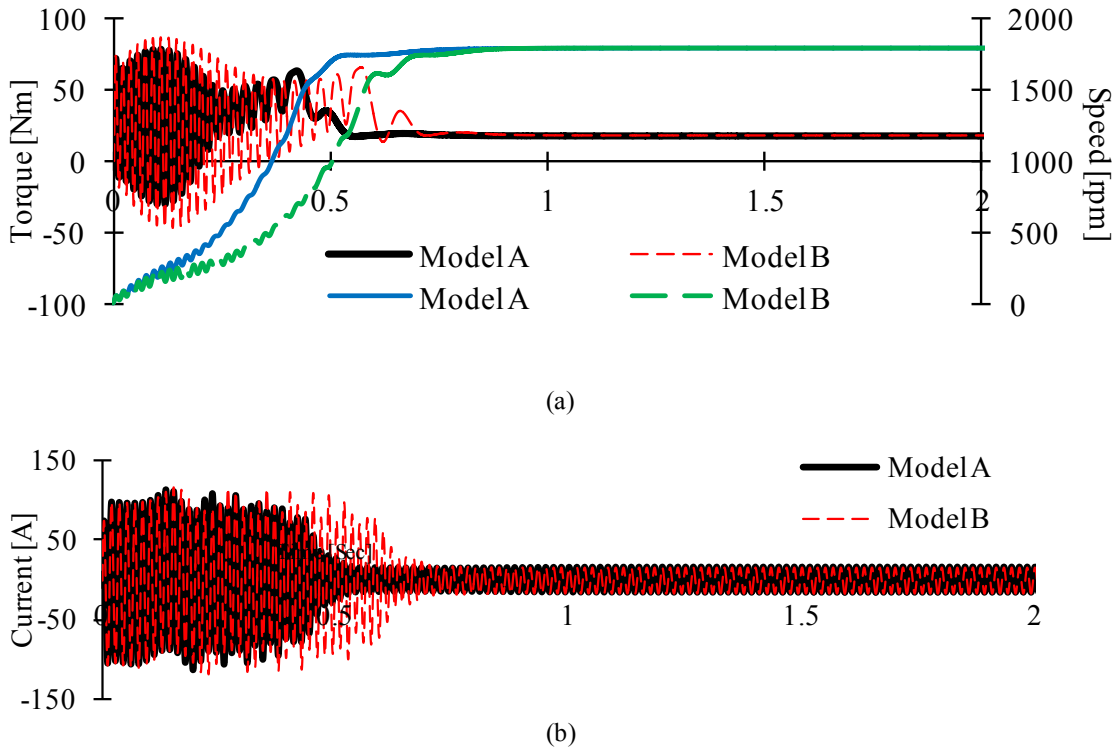

Figure 2-20. Calculated torque, speed and current waveforms from to start to synchronization near rated conditions of the machine with and without incorporating saturation in the machine models.

2.7 Conclusions

In this chapter, the rotor reference frame model based on Park's Transformation is developed for a PMSM with a damper winding. A novel and yet fundamental methodology to determine the parameters of a PMSM with a damper is proposed. Experiments have been performed using a developed position sensor and an experimental setup on a laboratory LSPMSM and synchronous machine. The parameters are determined through a combination of conventional machine theories and innovative methods of exciting the windings. The determined parameters have been subsequently incorporated into the developed LSPMSM mathematical model based on *dq* axis rotor reference frame theory. Numerical and experimental investigations have been performed to validate the determined parameters under both steady state and dynamic conditions of the machine. The results obtained from experiments are found to closely match with that of the numerical investigations. Hence, the accuracy of the parameters determined is claimed satisfactory.

Chapter 3

Dynamic and Steady State Performance

3.1 Introduction

Understanding EV motors and their operating conditions will be beneficial for tailoring them for traction purposes. This research focuses on transient performance during high speed and high torque operations and also short circuit conditions [75].

As discussed in the previous section, most EVs use an IPMSM as their traction motor due to the large power density, higher efficiency and capability to run over a large speed range with an almost constant power output with zero maintenance [76]. These synchronous motors for such vehicle applications invariably run under self-synchronous mode with rotor position feedback through a pulse-width modulated (PWM) inverter. Self-synchronous operation or self-control [77], [78] of the synchronous motor cause the drive to be self-starting and rules out the possibility of rotor falling out of step as rotor-position synchronized switching of the inverter devices always keeps the rotor speed synchronous with the exciting currents in the armature [77]. IPMSMs are known to be generally designed with an expectation of sinusoidal back EMF distribution [78]. The inductances of the armature circuit of the conventional IPMSMs generally provide enough filtering to smooth the armature currents into a sinusoidal waveform in response to the PWM voltage pulses impressed by the inverter on the armature terminals. Hence, torque ripple should be zero if purely sinusoidal currents are injected to a IPMSM with a purely sinusoidal back EMF distribution. Conventional wisdom, based on the aforementioned reasoning, dictates that dampers are not required in such motors for such applications as operation will always be synchronous. Dampers will therefore not be required - neither for starting nor for pulling into synchronism for such synchronous

motors. This line of reasoning is generally why IPMSMs employed in EVs do not possess dampers.

A LSPMSM, on the other hand, operates without rotor position feedback and in order to be self-starting must possess dampers and the design of dampers for such applications should be such that they should provide enough starting torque, and at the same time, help towards the pull-in phenomenon. Additionally, for such applications, the design of the dampers should be such that while drastic load disturbances appear on the system and the transient operation of the machine becomes asynchronous, the dampers should help in increasing the transient stability limit of the machine. Hence, substantial research to investigate the role of dampers for LSPMSMs has been conducted [60, 79, 80].

Similarly, for any permanent magnet synchronous generator (PMSG) which does not operate under rotor position feedback, dampers come into play during the transient asynchronous durations and help in restoring stability. The damper design for such applications has thus far solely concentrated on restoring transient stability [81, 82].

To the best of the authors' knowledge, publications to date have not yet investigated the performance of an IPMSM incorporating dampers bars for an EV application.

3.2 Motor Drives in Electric Vehicles

Most of the PMSMs on-board commercially available EVs have either a distributed or concentric winding arrangement in their stators and permanent magnets in their rotor. They are mostly three-phase (IPMSMs) driven with a maximum torque per ampere (MTPA) control strategy [10]. The DC link voltage of the three-phase self-controlled voltage source converter (VSC) driving the traction motor for such a vehicle remains constant and the inverter runs with under-modulation in the low-speed region and with over-modulation in the high-speed region of operation of the motor drive [11]. As the speed becomes progressively higher, the back EMF of the motor keeps increasing, and over a certain speed, the inverter starts operating as a pure square wave inverter, impressing a six-stepped phase voltage at the motor terminals. For EVs, this mode of operation can continue for a long time. As this mode of operation also calls for speed control, it is performed by the speed controller of the drive by adjusting the phase angle

of the six-stepped phase voltage waveform with respect to the back EMF of the corresponding armature phase, as dictated by the MTPA control strategy[78].

3.3 Case Study for Illustrating Repeated Overmodulation Operation Periods in an IPMSM Drive

The detailed specification of a commercially available vehicle used as case study for this research is shown in Appendix B. The vehicle has an IPMSM with maximum output power of 50 kW between 1,200 and 1,540 r/min and maximum torque of 400 Nm between 0 and 1,200 r/min. The combined output of the engine and motor is 82 kW at 85 km/h and higher, the maximum torque at 22 km/h or lower is 478 Nm. A Nickel-metal hydride battery pack with a nominal voltage of 201.6 V and output power of 21 kW is used as the electrical storage unit [83, 84]. The detailed data collected from a performance-mapping test of a 2004 Prius subsystem is presented in Appendix C [84].

The DC-DC converter, shown in Figure 3-1, is connected between the battery pack and the inverter to maintain the input voltage to the inverter at a level of 500 V. The three-phase voltage source Inverter (VSI) shown in Figure 3-1 is switched based on space vector pulse width modulation (SVPWM). The magnitude and frequency of the AC output depend on the reference voltage space vector and for the PWM.

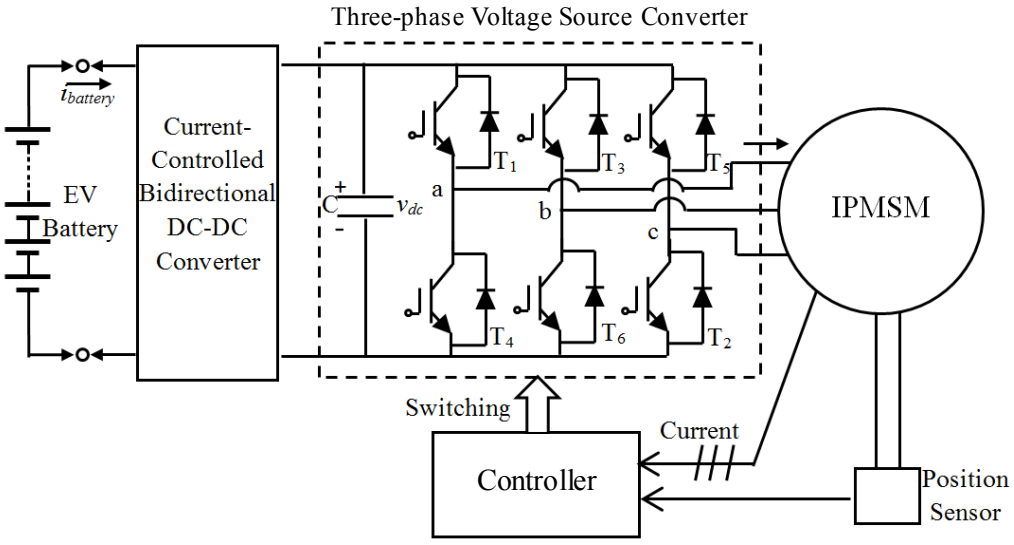

Figure 3-1. Diagram of electric components of an HEV powertrain.

The fundamental frequency voltage magnitude increases proportionally with the reference voltage space vector magnitude in undermodulation (linear) region. With further increase in the required voltage level, the overmodulation mode is encountered. In this mode, the voltage magnitude no longer varies in proportion with the reference voltage and a saturation emerges. Finally, beyond another point, the controller loses its control over the voltage amplitude and PWM degenerates into a square wave inverter waveform. With a given DC link voltage, the output line-to-line voltage fundamental rms value becomes fixed at $0.78V_{dc}$.

As seen in Table C-1, when the speed and torque of the motor are low such as data sets 1-1, 1-2, 2-1, etc., the output voltage level depends on the reference voltages. As the speed increases, in sets 4-3, 5-1, 6-1, etc., the output voltage exceeds the linear region and the inverter operates in 180 degree conduction mode. As indicated from Table C-1, for a large number of operating conditions, the motor is controlled by a self-controlled, rotor position synchronized square wave inverter during which the harmonic components of the voltage signal are significantly high and the torque response depends mainly on the load angle command set to the inverter.

3.4 IPMSM Drives for EV Application

Due to the variable speed and torque requirement of the traction application, a rotor position synchronized inverter is necessary to condition the current and voltage to control the motor (Figure 3-1) torque. Inverter switching is controlled to provide desired output voltage at a certain frequency synchronized with the speed of the electric motor. The inverter has to act depending upon the magnitude, phase, and frequency of the output voltages and currents.

3.4.1 Modeling of a Three-phase Voltage Source Inverter

The topology of a three-phase voltage source inverter is shown in Figure 3-1. The 6 switches are numbered based on their switching sequences. Top switches are odd numbers and bottom switches are even number and no two switches of the same leg will be on at a time [85]. The switching for leg a is represented with Boolean variable S_a : S_a =

1 signifies top switch of leg 1 is gated on; S_a =0 signifies bottom switch of leg 1 is gated on. Similarly S_b and S_c are defined for the other two legs.

With respect to the three switches, if V_{dc} is the DC link voltage of the voltage source inverter, the three-phase voltages of the inverter with respect to the load neutral in terms of switching action can be expressed as:

$$\left.\begin{aligned} v_{an} &= \frac{1}{3}(2S_a - S_b - S_c)V_{dc} \\ v_{bn} &= \frac{1}{3}(2S_b - S_a - S_c)V_{dc} \\ v_{cn} &= \frac{1}{3}(2S_c - S_a - S_b)V_{dc} \end{aligned}\right\} \tag{2.54}$$

The line voltages of the inverter is:

$$\left.\begin{aligned} v_{ab} &= (S_a - S_b)V_{dc} \\ v_{bc} &= (S_b - S_c)V_{dc} \\ v_{ca} &= (S_c - S_a)V_{dc} \end{aligned}\right\} \tag{2.55}$$

As seen from the voltage equations, the output AC voltage of the VSI depends only on the switching action, provided the DC link voltage is set to a particular value. In a square wave inverter the IGBTs of the inverter are switched on in sequence at every 60 degree interval and each switch is kept on for 180 degrees and then off for 180 degrees as. Three switches are gated at a time, either one at the top and two at the bottom or two at the top and one at the bottom.The phase voltage changes between $2V_{dc}/3$, $V_{dc}/3$, $-V_{dc}/3$ and $-2V_{dc}/3$ and the difference between phases is 120 degrees. The output voltage waveform does not depend on the load and contains low order harmonics. From Fourier analysis, the peak values of the fundamental frequency and harmonic components in the inverter output waveform can be obtained for a given input V_{dc} as [85]:

$$\left.\begin{aligned} \left(\hat{V}_{an}\right)_1 &= \frac{4}{\pi}\frac{V_{dc}}{2} = 0.637V_{dc} \\ \left(\hat{V}_{an}\right)_h &= \frac{\left(\hat{V}_{an}\right)_1}{h} \end{aligned}\right\} \tag{2.56}$$

where the harmonic order h takes only odd values.

3.4.2 Experimental Implementation of a Square Wave Inverter Driven LSPMSM

In order to verify the role of dampers in a PMSM intended for electrified vehicle application, it is required to have a PMSM with damper bars, which conventional PMSM's do not have. A line-start PMSM was available in the laboratory and the damper which are integral with such a machine initiated the investigation of the effects of dampers. This LSPMSM has been run in the self-controlled mode (with rotor position feedback) through a three-phase square wave inverter. The *dq* axis model and its parameters for this LSPMSM have already been derived and experimentally validated by a novel technique in Section 2.3.

The test machine (motor) is equipped with a low cost position sensor indicating the position at every 60 degrees and is coupled with a DC machine (operating in the generator mode) as load. A three-phase IGBT inverter stack is used as the voltage source inverter, and a TMS320 series digital signal controller is used to provide rotor position synchronized gate signals based on a 180 degree conduction scheme to actuate the inverter. A photograph of the whole arrangement as made in the laboratory is shown in

Figure **3-2**.

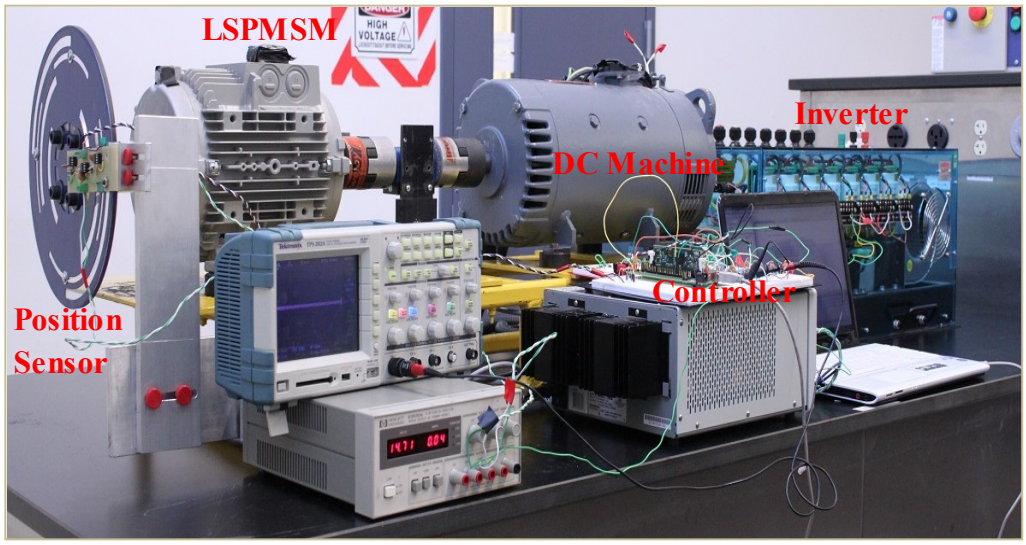

Figure 3-2. Laboratory PMSM driven by rotor-position synchronized square wave inverter.

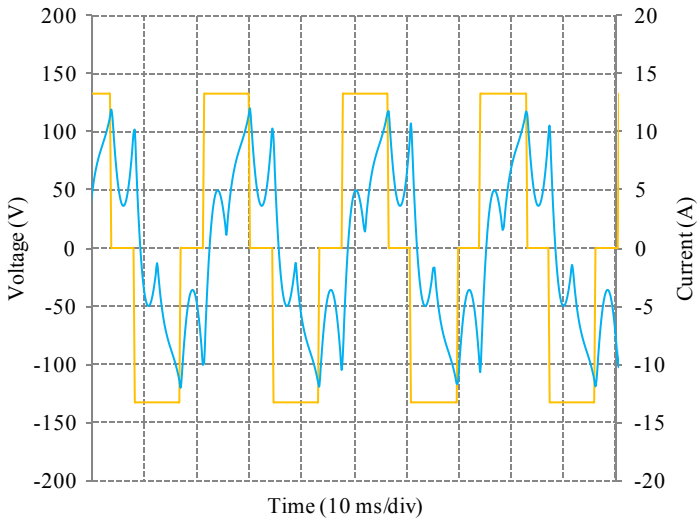

(a)

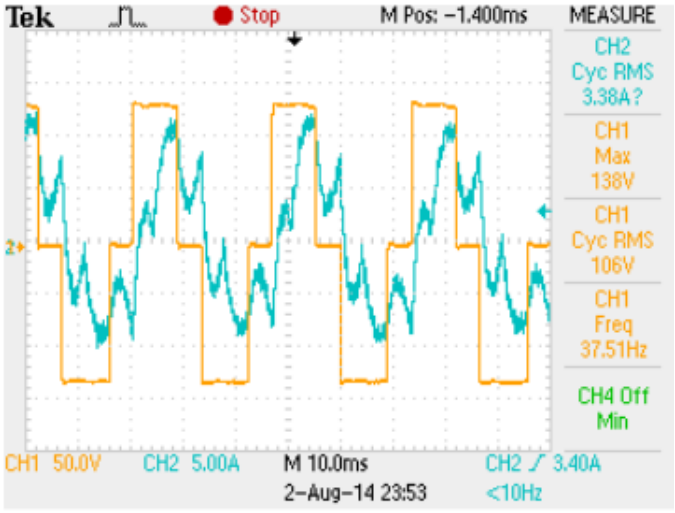

(b)

Figure 3-3. Calculated and experimental voltage and current waveforms of the LSPMSM driven by a square wave inverter. (a) Calculated: —v_{ab}, —i_a. (b) Experimental: — v_{ab}, — i_a.

The calculated results, as per the previously derived *dq* axis model and its parameters [64], and experimental results of the described drive are presented in Figure 3-3 for a particular load angle. The DC link voltage is set as 132 V and the load angle δ is controlled to be 60 degrees. The machine settles at a speed of 1125 r/min. The simulated result closely manifests the distortion in the current waveform that is seen in the experiment due to the squirrel-cage damper in the LSPMSM. The amplitude of simulated current has been found higher than the experimental one for all cases of set loads and load angles for which the drive is run, because the mechanical and core losses are neglected in the calculations. Instantaneous current flowing into the machine armature is

considered positive in the presented waveforms. The fact that the actual operating load angle is equal to the set one in the simulation and the experiment is verified by comparing the phase of the terminal line to line voltage with the phase of the corresponding back EMF, which is obtained by calibrating the rotor position sensor [64].

The calculated and experimental results show similar characteristics thus establishing that the developed model of the rotor-position-synchronized, square wave inverter driven LSPMSM, characterized by its *dq* equivalent circuit resistance and inductance parameters satisfactorily describes an interior PMSM with dampers under steady state and dynamic conditions. Thus, this model is henceforth employed to study the effect of dampers in the performance of the drive, by changing its damper parameters in an iterative procedure.

3.5 Comparative Analysis of Dynamic and Steady State Performance

When a sudden change in the applied voltage at the stator terminals occurs, in the *dq* equivalent circuits shown in Figure 2-8, the branches containing the damper parameters become operative. They remain operational in the circuit until a steady state condition is reached. During this dynamic condition, the damper *RL* branch comes in parallel with the magnetising reactance. The equivalent impedance of the parallel branch is lower than the magnetizing reactance resulting in a low value of net impedance viewed from the *d*- or *q*-axis stator terminals. This low impedance across the stator terminal causes larger overshoots in the current when compared to a machine without the damper.

When a damper branch is paralleled across L_{md} or L_{mq}, an additional resistance is present in the parallel branch which causes the equivalent resistance of the circuit to also reduce. However, the practical values of damper parameters employed are such that, the net decrease in L is much more than the net decrease in R. Hence the net time constant reduces resulting in a faster dynamic response.

TABLE 3-1. SAMPLE STEADY STATE AND DYNAMIC PERFORMANCE OF THE EXISTING AND PROPOSED MACHINES (STATOR RESISTANCE TO DAMPER RESISTANCE RATIO – 3:2, STATOR LEAKAGE INDUCTANCE TO DAMPER LEAKAGE INDUCTANCE RATIO – 1:1)

Load Angle		Original on-board EV motor	Proposed on-board EV motor with a damper
30°	Speed (r/min)	3951	3952
	Torque Ripple (%)	14	64
	Stator Current (A)	47.1	47.1
	THD in Current (%)	11.1	66.8
40°	Speed (r/min)	5579	5577
	Torque Ripple (%)	14	36
	Stator Current (A)	61.7	61.7
	THD in Current (%)	5.8	36.6
Transition	Transition Time (s)	1.255	0.59
	Peak Electromagnetic Torque (Nm)	90	340
	Peak Stator Current (A)	76	255

TABLE 3-2. SAMPLE STEADY STATE AND DYNAMIC PERFORMANCE DATA OF THE PROPOSED MACHINE WITH A DAMPER KEEPING STATOR TO DAMPER RESISTANCE RATIO OF 1:1 AND VARYING THE STATOR TO DAMPER LEAKAGE INDUCTANCE RATIO

Load Angle		Stator to Damper Leakage Inductances Ratio					
		3:1	2:1	1:1	1:3	**1:5**	1:10
40°	Speed (r/min)	5584	5580	5576	5572	**5571**	5570
	Torque Ripple (%)	64	50	32	22	**16**	14
	Stator Current (A)	61.5	61.6	61.6	61.6	**61.6**	61.6
	THD in Current (%)	56.6	48.6	35.9	79.6	**13.4**	9.8
Transition	Transition Time (s)	0.88	0.901	0.898	0.885	**0.853**	0.847
	Peak Electromagnetic Torque (Nm)	480	430	334	200	**150**	125
	Peak Stator Current (A)	373	410	317	155	**142**	118

TABLE 3-3. SAMPLE STEADY STATE AND DYNAMIC PERFORMANCE DATA OF THE PROPOSED MACHINE WITH A DAMPER KEEPING STATOR TO DAMPER LEAKAGE INDUCTANCE RATIO OF 1:5 AND VARYING THE STATOR TO DAMPER RESISTANCE RATIO

Load Angle		Stator to Damper Resistance Ratio					
		3:1	2:1	**1:1**	1:3	1:5	1:10
40°	Speed (r/min)	5575	5572	**5571**	5570	5570	5570
	Torque Ripple (%)	18	16	**16**	16	16	16
	Stator Current (A)	61.6	61.6	**61.6**	61.6	61.6	61.6
	THD in Current (%)	13.4	13.4	**13.4**	13.4	13.4	13.4
Transition	Transition Time (s)	0.424	0.499	**0.853**	1.022	1.151	1.188
	Peak Electromagnetic Torque (Nm)	155	150	**150**	160	159	145
	Maximum Stator Current (A)	143	142	**142**	121	121	114

3.5.1 Investigation of the Effects of Damper Parameters in Dynamic and Steady State Performance

In order to further study the effect of a damper on an IPMSM to consider it for EV application, the developed and validated model is used to simulate a 50 kW on-board EV motor with emulated dampers, the equivalent circuit parameters of which are given in Appendix D [86]. The measured parameters of the LSPMSM are utilized as the starting point of this investigation. The LSPMSM has a symmetrical squirrel cage, and therefore the equivalent circuit parameters in *d*-axis equal to that in *q*-axis. The ratio between the stator resistance and damper resistance is 3:2, and the ratio between the stator leakage inductance and rotor leakage inductance is 1:1 [64].

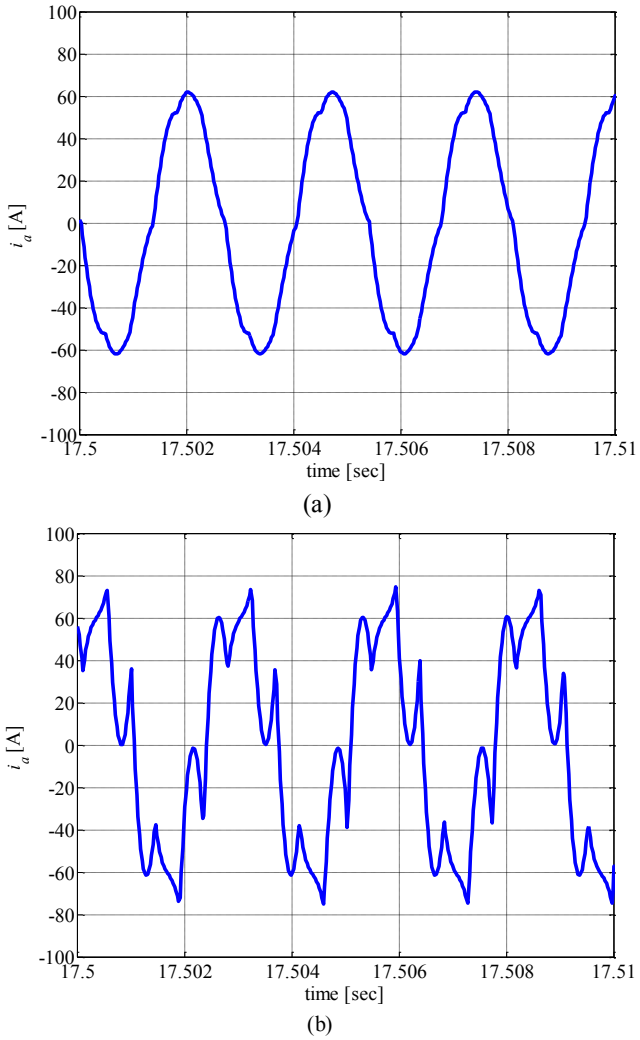

Figure 3-4. Current waveforms of the machines investigated driven by a square wave inverter with rotor position feedback at a load angle of 40°. (a) Original on-board EV motor. (b) On-board EV motor with a damper parameters corresponding to Table II.

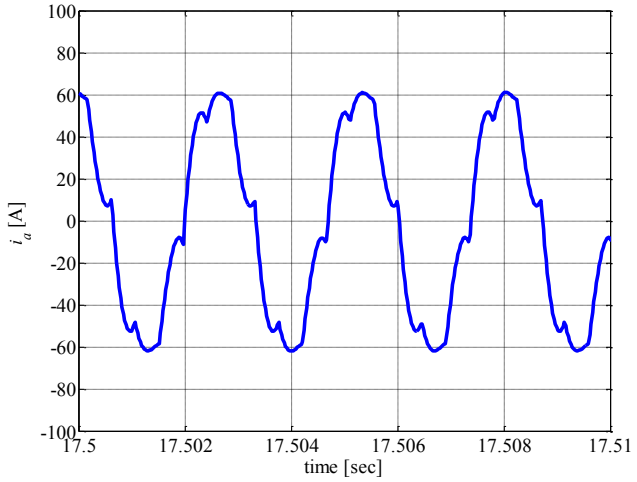

Figure 3-5. Current waveform of the finalized EV motor with a damper having a stator to damper resistance ratio of 1:1 and stator to damper leakage inductance ratio of 1:5.

The steady state and dynamic performance of the on-board EV motor and the proposed on-board EV motor with emulated damper parameters of the same stator to damper ratio as that in the LSPMSM is investigated first to understand the role of dampers in high speed region of the EV motor. Both machines are driven by a square wave inverter with rotor feedback, which initially controlled the machine with a load angle of 30° and later changes to a load angle of 40° after the speed reaches steady state. Load torque kept constant at 50 Nm. The DC link of the inverter is also kept constant at a level of 500 V. The values of the major electrical and mechanical variables are presented in Table 3-1.

As seen from Table 3-1, for both machines, the final speeds of the machines are determined by the load angle. The speed increases when the load angle increases. Because of the distortion in the terminal voltage, now containing lower side band harmonics, the phase current has high distortion, and causes higher torque ripple in the machine. The distortion is more at lower speed than that at higher speed. The current waveforms of both machines at a load angle of 40° is shown in Figure 3-4.

The maximum current and torque of the machines during transition from one steady state speed to another are greatly influenced by the damper. It can be seen from the transition time, (defined as the time for the speed to reach 90% of the steady state value) that by adding a damper, the machine responds faster to changes and restores to a new steady state faster. This fast dynamic response is desired in an EV application. The final speed of the machine is not reduced appreciably with the added damper. The fundamental

current amplitude is not affected by the damper either. However, the damper increases the distortion in current and consequently increases the torque ripple significantly. As a result, it is necessary to design a damper for traction motors in order to improve dynamic performance as well as keeping satisfactory steady state performance.

Further studies to investigate the effect of damper on machine performance have therefore been performed to understand the role of damper in IPMSM for EV application. The operation conditions are kept same as mentioned previously.

Firstly, the ratio between stator resistance and damper resistance is kept constant as 1:1, and the ratio between stator leakage inductance and damper leakage inductance is varied as shown in the cases presented in TABLE 3-2. The steady state evaluations are only shown at a load angle of 40° as the trend at lower speed can be inferred from Table 3-1. It can be elicited from TABLE 3-2 that, given a resistance, the current distortion reduces as the damper leakage inductance increases. The current overshoot of the motor is more significant with smaller rotor leakage inductances. However, the response time remains almost same.

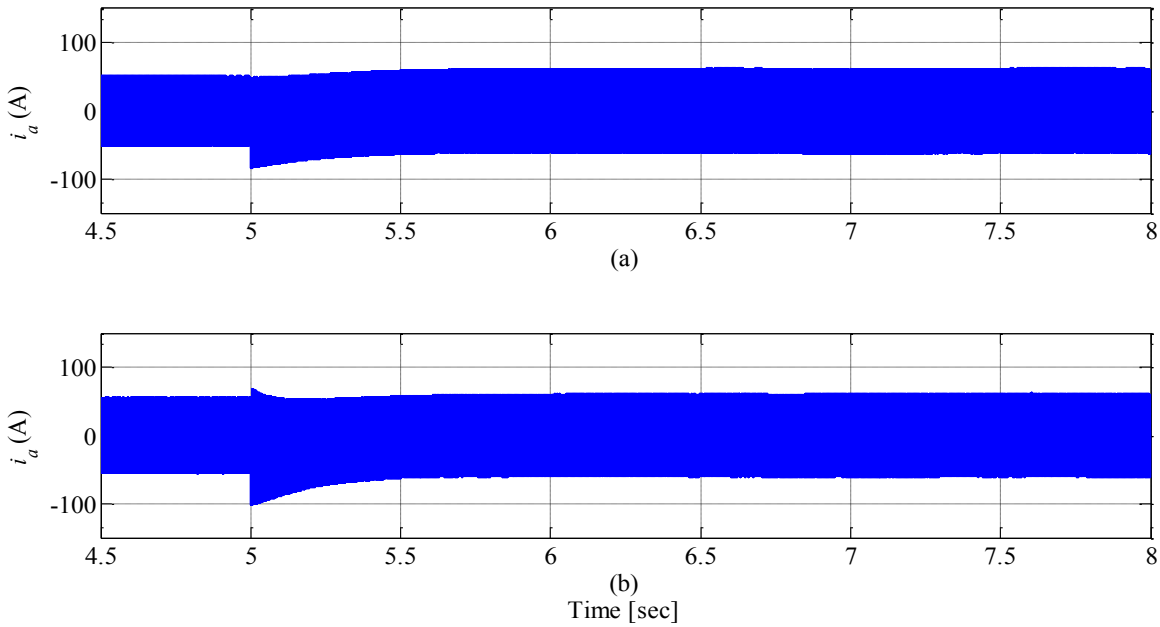

Figure 3-6. Calculated stator current of the original PMSM without a damper and proposed PMSM with a damper under a sudden increase in load angle. (a) Without damper. (b) With damper.

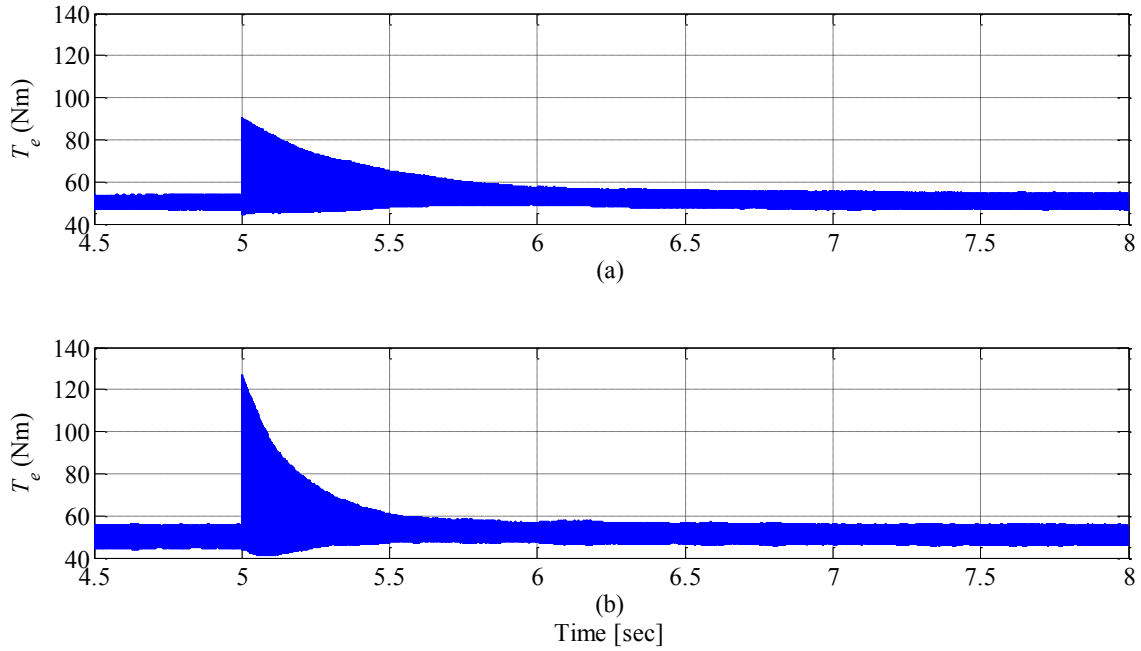

Figure 3-7. Calculated developed electromagnetic torque of the original PMSM without a damper and proposed PMSM with a damper under a sudden increase in load angle. (a) Without damper. (b) With damper.

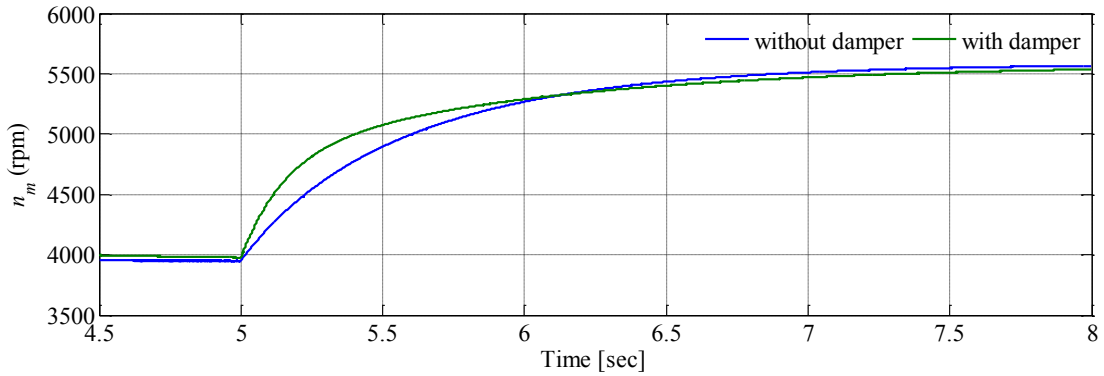

Figure 3-8. Calculated developed speed of the original PMSM without a damper and proposed PMSM with a damper under a sudden increase in load angle.

Based on the performance analysis in Table 3-2, a stator to damper leakage inductance ratio of 1:5 is selected for the analysis of the effect of damper resistance as it yields the most satisfactory performance out of the considered cases. From the results shown in

Table 3-3, the system response time is marginally different with different values of damper resistance. Moreover, the distortion in the current and torque ripple, the overshoot of current and torque during transition do not change significantly with the rotor resistance. It can be inferred from Table 3-2 and

Table **3-3** that the improvement of transition time with a damper is mainly determined by the damper resistance. The harmonic components and the overshoot during transient conditions are influenced largely by the damper leakage inductance. Figure 3-5 illustrates the current waveform of an emulated machine with a stator to damper resistance ratio of 1:1 and stator to damper leakage inductance ratio of 1:5. It can be seen that the waveform quality is significantly improved compared the current waveform of the machine with a line-start damper. The damper parameters will also influence the equivalent line inductances during integrated charging operation, further details of the damper effect will be presented in later section of this study. Based on the requirements, the damper parameters are decided and shown in Appendix D. However, investigation to select the optimized damper parameters considering traction and integrated charging simultaneously is of great importance and viewed as a future scope of this research.

3.5.2 Investigation of Dynamic Response with Change in Load Angle

The damper parameters of the *dq* equivalent circuit of the finalized EV motor with a damper are chosen based on the previous investigation keeping in mind both the transient response and steady state performance. An operating condition is considered, when the DC input to the inverter is 500 V and the machine is operating under a constant load torque of 50 Nm. Both machines initially operate with a load angle of 30° and at steady state speed of 4,000 r/min. At the time instant of 5 seconds from start, the load angle increases to 40º. Due to the paralleled effect of the damper, the phase current in the machine with a damper shown in Figure 3-6(b) rises to a higher value in a shorter amount of time compared to the phase current of the IPMSM without a damper shown in Figure 3-6(a). As a result of the transient response of the current, the peak electromagnetic torque developed in the machine with a damper shown in Figure 3-7(b) is higher than that of the original machine presented in Figure 3-7(a). The corresponding speed responses of the two machines are given Figure 3-8. As the torque response of the finalized EV motor with a damper is faster, speed of that motor also settles faster for the same load torque as evident from Figure 3-8. The torque and speed of the machine with a damper definitely shows a better dynamic response compared to the original machine. Figure 3-9 to Figure

3-11 represent the stator current, electromagnetic torque and speed of the original PMSM and the proposed machine with a damper under a sudden decrease of load angle from 40º to 30º. The torque and speed of the machine with a damper also shows a better dynamic response compared to the original machine.

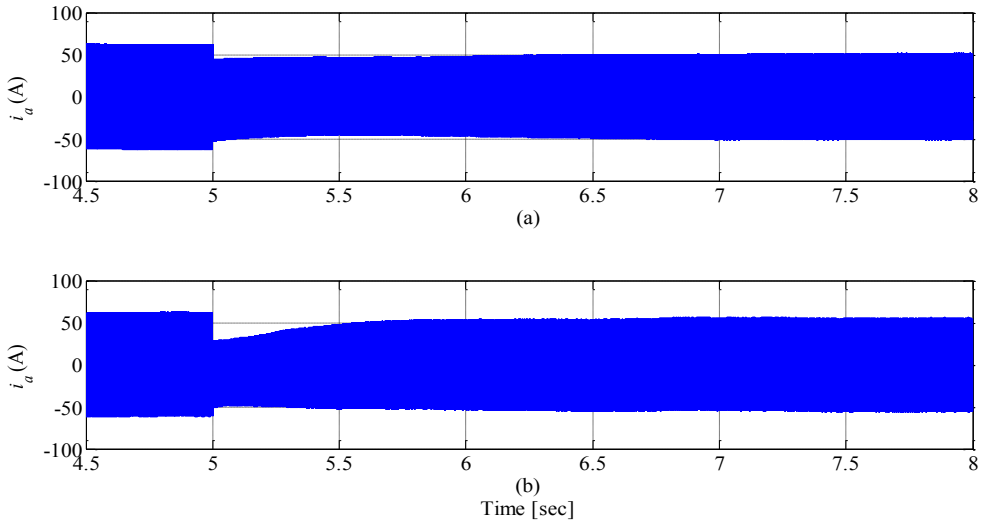

Figure 3-9. Calculated stator phase current of the original PMSM and proposed PMSM with a damper under a sudden decrease in load angle. (a) Without damper. (b) With damper.

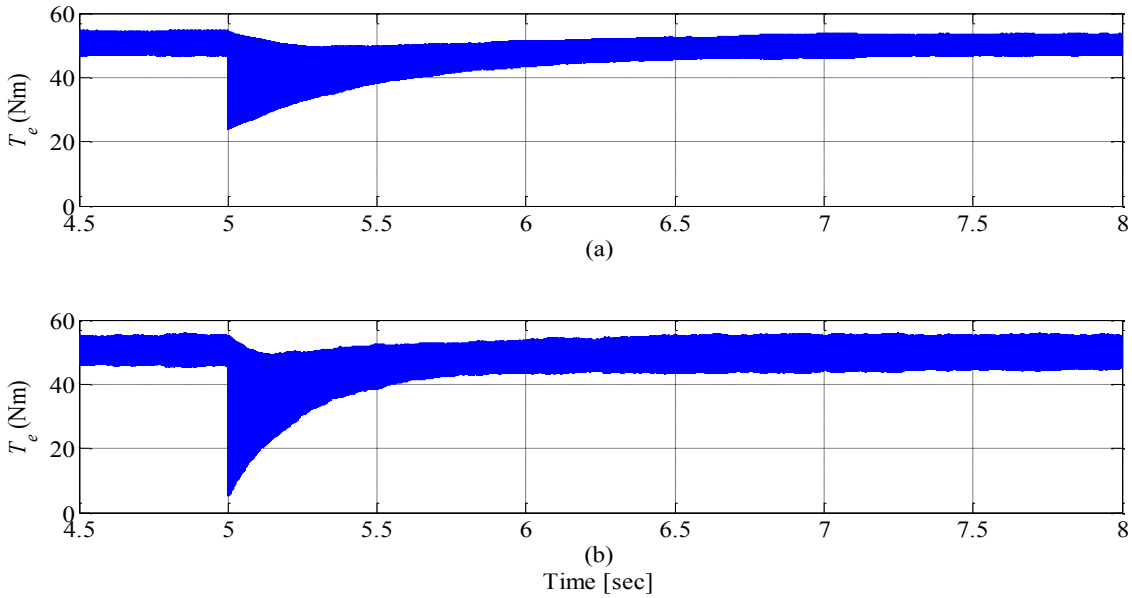

Figure 3-10. Calculated developed electromagnetic torque of the original PMSM and proposed PMSM with a damper under a sudden decrease in load angle. (a) Without damper. (b) With damper.

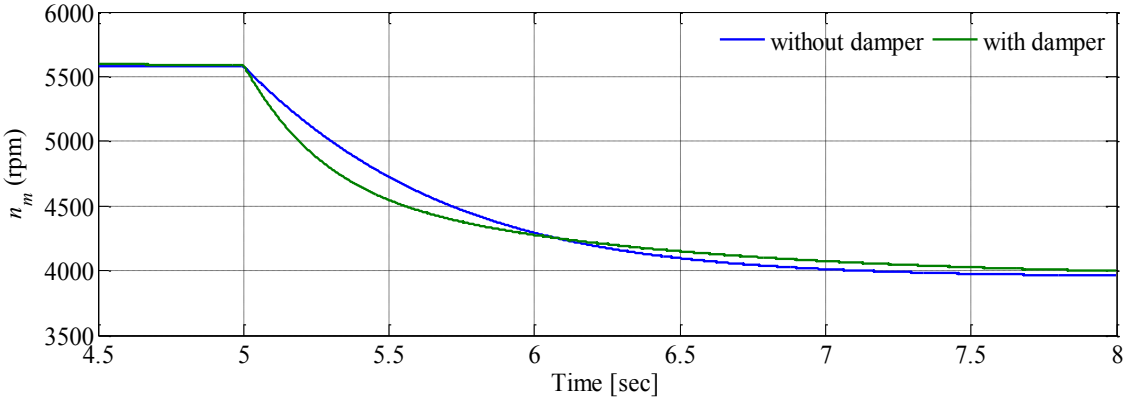

Figure 3-11. Calculated speed of the original PMSM and proposed PMSM with a damper under a sudden decrease in load angle.

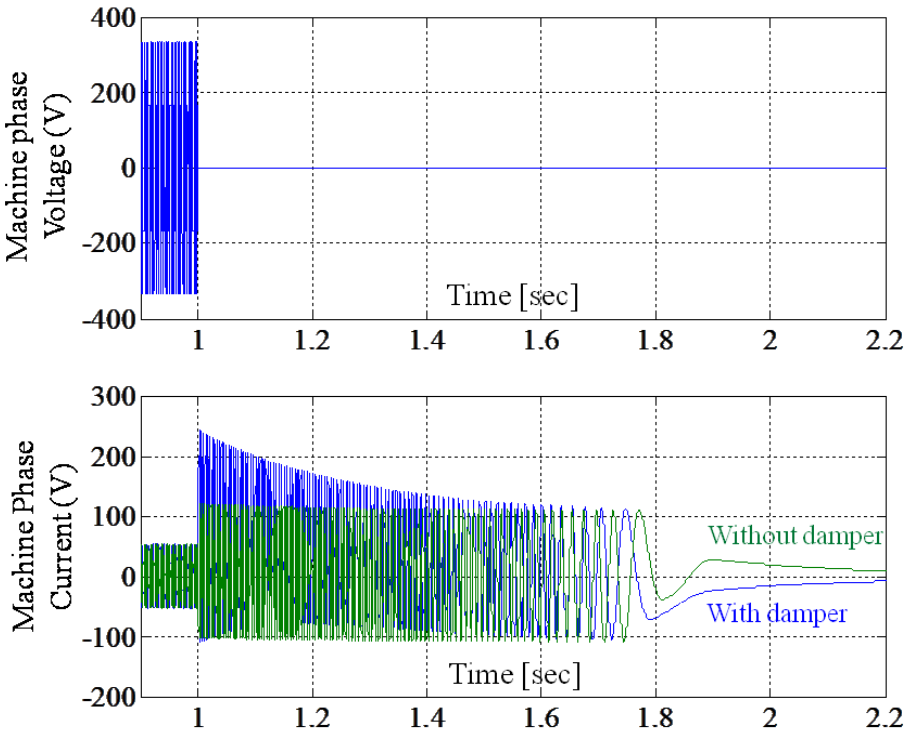

Figure 3-12. Response of machine phase current during a three-phase symmetrical short circuit fault.

3.5.3 Short Circuit Response

Generally, any machine is protected against short circuit conditions using high rupturing capacity (HRC) fuses. The melting ability of fuses are based on various characteristics which include the ratio of threshold current to rated continuous current (threshold ratio),

peak let-through current versus prospective short circuit current characteristic curves, and I^2t characteristics [87].

Considering the machine is operating with a constant load torque of 100 Nm and at a speed of 4,000 r/min, a three-phase symmetric fault is initiated at the machine terminal. The calculated currents for the original EV motor without a damper and the finalized EV motor with a damper are shown in Figure 3-12. It can be seen that the overshoot is more and rise time is less in the machine with the damper. This feature will cause the fuse to blow off faster in case of the machine with a damper, thus, saving the machine.

3.6 Conclusion

In this chapter, results of experimental testing of an in-house hybrid electric vehicle are presented and the necessity of improving dynamic performance is justified through experimental data. Experiments were performed on a square wave inverter driven LSPMSM and the developed motor and drive model were verified. The improved performance is shown through the comparison of calculated results based on a 50 kW IPMSM with and without a damper. It is shown that the IPMSM with a damper is effective in improving the dynamic performance during high speed operation and short circuit response without significantly compromising the steady state performance.

Chapter 4

Three-phase Integrated Charging

4.1 Introduction

Next generation electric vehicles (EV) and plug-in hybrid electric vehicles (PHEV) with vehicle-to-grid (V2G) and grid-to-vehicle (G2V) integration capability call for advanced research and development on charging strategies. The integration of such large number of vehicles, would leave a huge stress on the stability of the power system especially vehicles with single-phase on-board chargers [69]. A three-phase charger which imposes balanced loading on the utility and also ensures high power quality and power output is an excellent option for EV charging. However, due to the weight and size, three-phase chargers are generally off-board and comparably more expensive than single-phase ones. The traction motor and power electronics converters can be reconfigured to make on-board three-phase charging feasible. IPMSMs are the most common traction motor in existing EVs, however, due to the salient nature of the rotor, the self inductances and mutual inductances values depend on the rotor position [39]. By adding a damper, the 'salient' nature can be compensated by the damper cage, and the machine windings can be considered as three equal inductances when connected in series with the grid for charging purposes.

4.2 Investigation of a Single-phase On-board Battery Charger for an Electric Vehicle

As the leading names in auto industry compete to market high performance hybrid vehicles, Canadian consumers now have a wide selection of plug-in hybrid/electric models to choose from. Federal programs and incentives such as Automotive Partnership

Canada (APC), *ecoAUTO* rebate program, *ecoTECHNOLOGY* for vehicles program and *ecoENERGY* for personal vehicles program are encouraging consumers to convert to electrified transportation. The Government of Ontario's vision to have one out of every twenty vehicles to be electrically powered by 2020 is also a commercial boost to the alternative vehicle sector [88].

However, one has to notice that all plug-in and electric vehicles have to be charged from the existing grid. Utility companies would feel the heat in the future as these vehicles would leave an impact on the distribution grid as the new age of distributed generation in transportation electrification arises through the vehicle-grid and grid-vehicle concepts. These vehicles connected simultaneously to the grid, consume a large amount of electrical energy and this demand of electrical power can lead to extra large and undesirable peaks. Also, the power quality problems such as poor power factor, higher total harmonic distortion (THD) during charging and discharging may cause equipment malfunction and component failures [89, 90]. In addition, electrical distribution systems are normally of the three-phase four-wire type, allowing loads and renewable energy sources to be connected either at line-to-line or line-to-neutral. These are usually arranged in order to result in a balanced power distribution across the three-phases. However, when a single-phase battery charger converter, with a relatively larger output impedance of the low pass filter, is connected to the grid, a large voltage imbalance might appear [91].

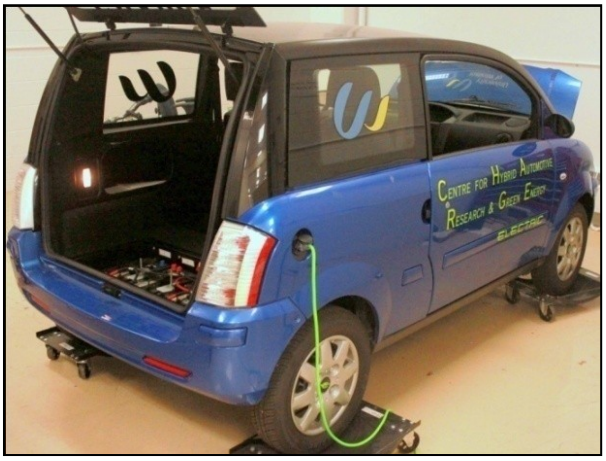

Figure 4-1. The in-house electric vehicle with a single-phase battery charger under consideration in the experimental investigations.

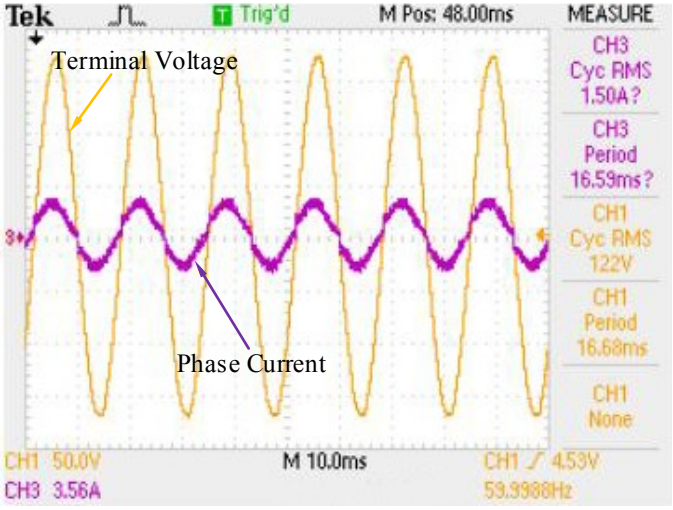

(a)

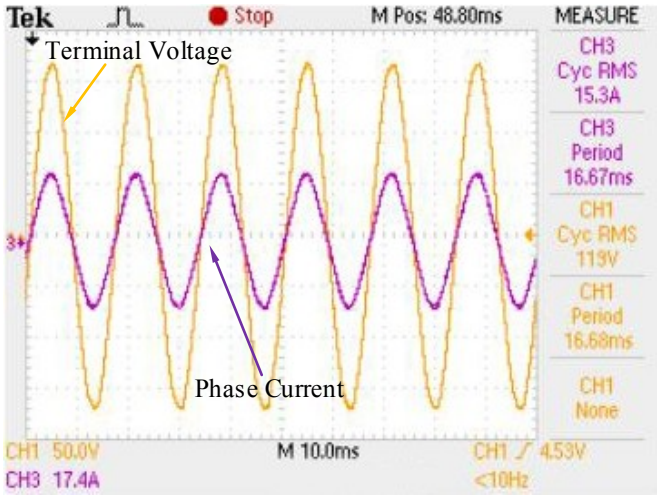

(b)

Figure 4-2. Grid current and voltage waveforms for the single-phase battery charger under consideration. (a) Low charging current. (b) High charging current.

In order to study the quality of voltage and current profiles during charging of the battery, experiments were performed using a battery electric vehicle shown in Figure 4-1. The current profile, voltage profile, total harmonic distortion and displacement power factor were measured using a Tektronix 2024 digital storage oscilloscope and a Fluke 434 power quality analyzer connected across the terminals of the on-board single-phase battery charger over a period of time. The measured waveforms of current and voltage are as shown in Figure 4-2(a) and (b) for two different states of charging. From Figure 4-2, it can be observed that the applied voltage across the charger terminals has almost a sinusoidal waveform and the displacement power factor is very close to unity. However,

the amount of harmonics inserted into the current waveform is rather high (in regards to the IEEE 519 power quality standard) at lower levels of charging current under 'trickle' mode, as evident from Figure 4-3(a). This is typical of the single-phase PWM rectifier based resistor-emulating DC-DC converter [92].

As discussed in the previous section these harmonics injected into the system might cause detrimental effects on the distribution grid's transformers and feeders. Also, the battery charger readily fitted on-board takes around 8 hours to charge the battery from 0% to 100% SOC. Figure 4-3(a) and (b) show the measured total harmonic distortion (THD) and the harmonic spectrum of the current waveform [69].

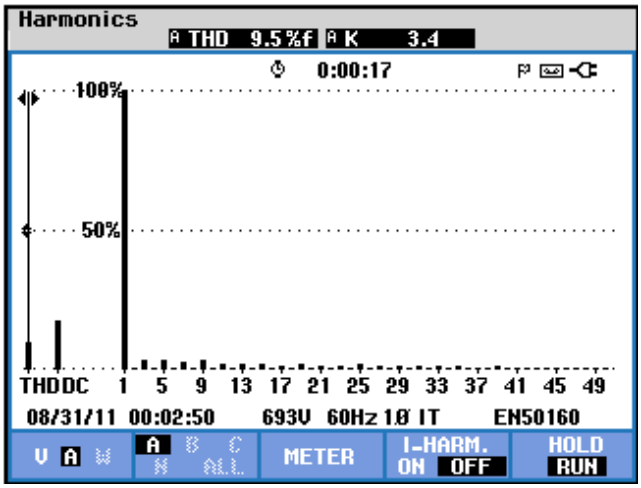

(a)

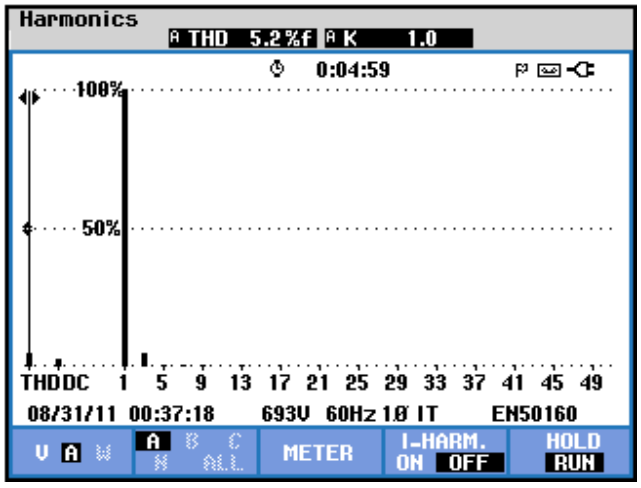

(b)

Figure 4-3. Measured THD and the harmonic spectrum of the current waveform. (a) Low charging current. (b) High charging current.

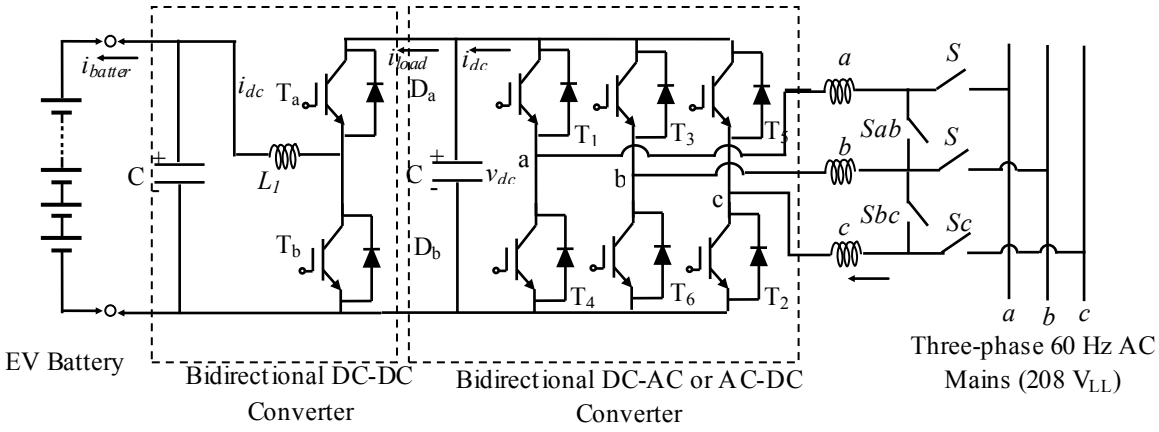

Figure 4-4. Overall block diagram of the three-phase bi-directional charger.

4.3 Integrated Charger Using Traction Components

Understanding the merits and demerits of the chargers proposed previously, an efficient charger should have high output power, balanced AC side loading, fast dynamic response without overshoots and undershoots, bi-directional power flow capability, unity power factor and very low harmonics. High performance three-phase battery chargers at higher power levels employ a two stage power converter system consisting of a grid side two-level IGBT based voltage source converter (VSC) and a two quadrant buck-boost current controlled DC-DC converter at the battery side. The DC-DC converter is employed to control the charging rate for its optimal performance and the grid side VSC is employed to ensure that the power factor at the point of common coupling (PCC) can be ideally maintained at unity, thereby maximizing the power flow in either direction. The grid side VSC is generally controlled by adopting a technique very similar to the field-oriented/vector control of electrical AC machines [93]. Figure 4-4 demonstrates the topology of an integrated charging system with additional relay/contactors on the machine windings. In traction mode, switches S_{ab} and S_{bc} are closed to form a single neutral point of machine, while in charging mode, switches S_a, S_b and S_c are closed to connect the windings to the grid so that the machine inductors act as part of a boost rectifier for G2V operation. Due to electric motor construction, a magnetic coupling exists between the three inductances, because of this coupling and the buried magnets rotor structure of IPMSM, the equivalent impedances in the thee phases at stand-still condition are not equal and depend on the rotor position [39].

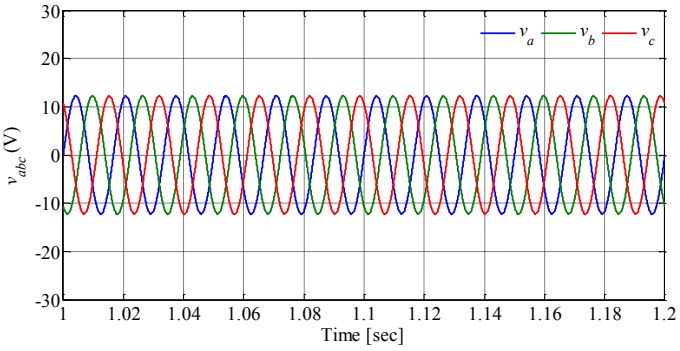

(a)

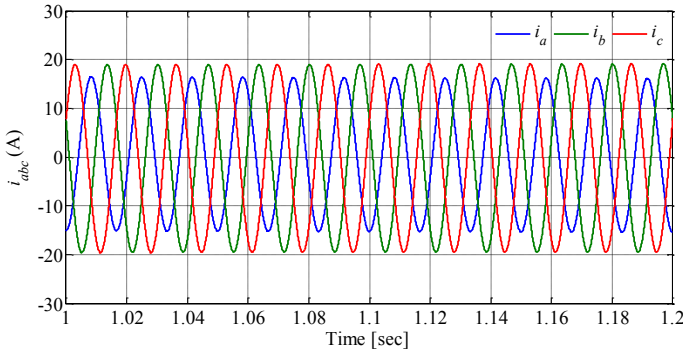

(b)

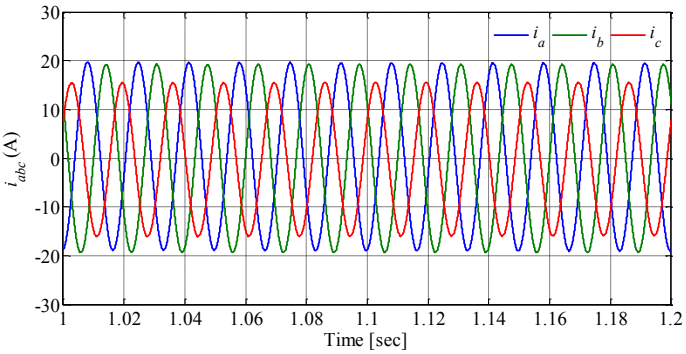

(c)

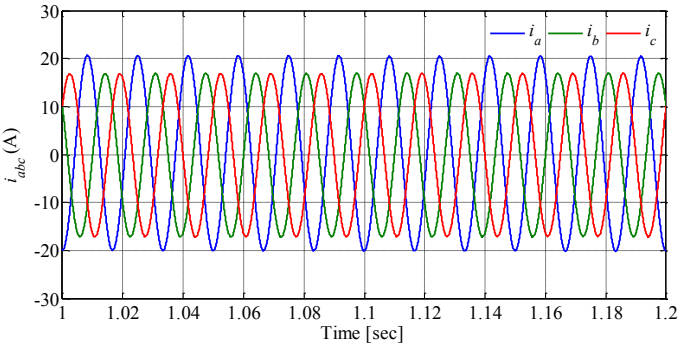

(d)

Figure 4-5. Stator voltage and current of an IPMSM at stand-still condition. (a) Terminal phase voltage. (b) Terminal current when $\theta_r = 0°$. (b) Terminal current when $\theta_r = 60°$. (c) Terminal current when $\theta_r = 90°$.

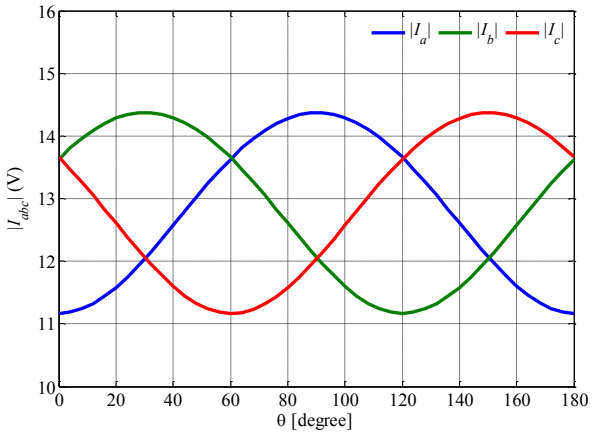

Figure 4-6. The rms value of the induced current in *abc* phases with respect to rotor position θ_r for a given line voltage of 15 V.

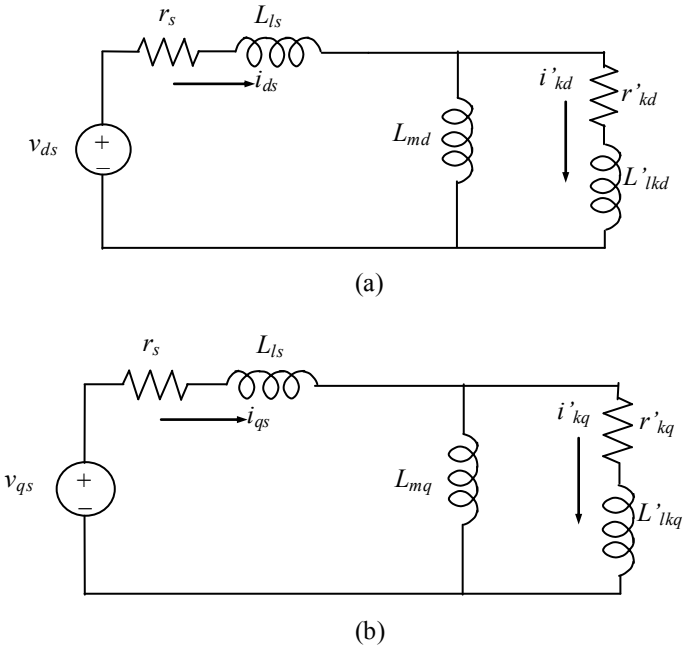

Figure 4-7. Equivalent circuit of an IPMSM with a damper under blocked rotor condition.

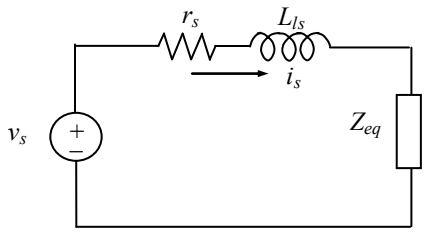

Figure 4-8. Per phase equivalent circuit of an IPMSM with a special damper..

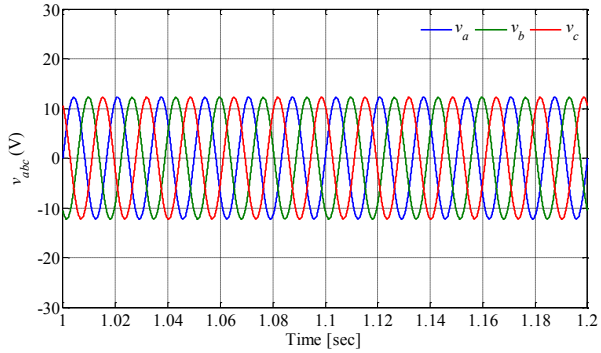

(a)

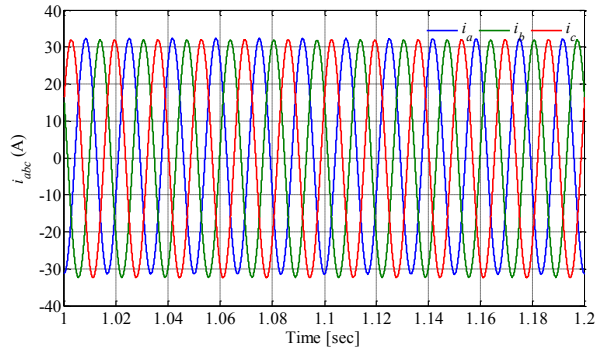

(b)

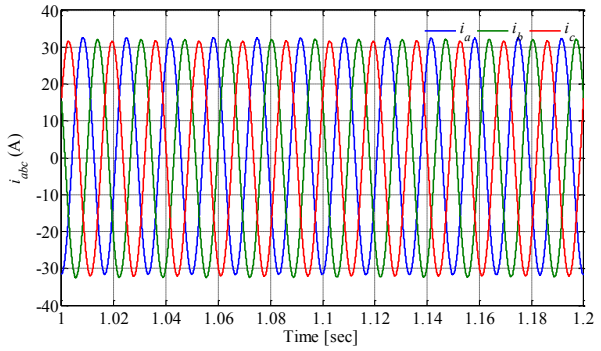

(c)

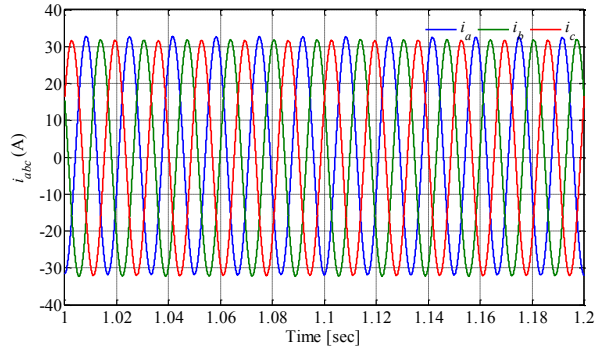

(d)

Figure 4-9. Stator voltage and current of an IPMSM with a special damper at stand-still condition. (a) Terminal phase voltage. (b) Terminal current when θr = 0°. (c) Terminal current when θr = 60°. (d) Terminal current when θr = 90°.

In order to understand the machine equivalent inductance at standstill, an IPMSM under block rotor condition with a three-phase balanced voltage of 15 V line to line is studied and the results are presented in Figure 4-5. It is clear from the current waveforms at three different rotor positions that the magnitudes of the currents in the three-phases are not equal and are varying with θ_r. This is because of the unequal values of the self inductances of each phase and mutual inductances between phases in an IPM machine. The relationship of the rms value of the phase current and θ_r is shown in Figure 4-6. Therefore, if an IPMSM is connected for integrated charging, the impedance of each phase is not equal and the three-phase charging will be drawing unbalanced current from the grid side causing a hazardous neutral current in the grid. By adding a damper, the unbalanced condition can be mitigated significantly. Referring to the equivalent circuit shown in Figure 2-8, under blocked rotor condition (ω_r=0), the equivalent circuit can be simplified as shown Figure 4-7. As shown in previous studies, because of the difference in the *d* and *q* axes parameters of the machine, the inductances in three-phases vary with rotor position. If the damper is designed such that the equivalent inductances in the parallel branches of *d* and *q* axes are equal, the saliency effect created by buried magnets will be canceled by the damper circuits. The machine can be represented by a per phase equivalent circuit as shown in Figure 4-8. In other words, when switches Sa, Sb and Sc in Figure 4-4 are connected for charging operation, the equivalent impedances on the three lines are equal and therefore will draw balanced current from the grid.

4.4 Real-time Control Strategy of the Integrated Charger Converter

4.4.1 Bidirectional DC-DC Converter

The rating of the integrated battery charger system with bi-directional power flow capability considered is 10 kW. A maximum controlled charging current of +/- 20 A at 500 V DC level has been considered to be ultimately drawn from or feeding to the three-phase 60 Hz, 208 V AC grid, depending on the direction of power flow. The current controlled bidirectional DC-DC converter at the battery end operates in two-quadrants, where the voltage polarity does not change but the DC current polarity should change

depending whether it is a G2V or V2G application. The direction of average power flow or current for G2V application has been considered positive in the calculations and analysis, and hence negative for V2G application. For G2V operation, the DC-DC converter acts as a current-controlled buck chopper and for V2G case, it acts as a current-controlled boost chopper.

The vehicle in this study has six lead acid batteries rated at 12 V and 100 Ah each. The voltage at the low voltage side is considered to be varying from 60 V to 360 V and a current output range from 25 A to 150 A to cater to a range of vehicles varying from the in-house battery electric vehicle (BEV), Mitsubishi iMiEV and Nissan Leaf which have fast charging capability. The switching frequency employed for the converter is 10 kHz considering a power throughput range of around 10 kW. The topology of the bidirectional DC-DC converter is shown in Figure 4-4 and the control of the IGBT's T_a and T_b should be such that the battery is able to be charged or discharged as per requirement. When the battery is to be charged, i.e. power has to flow from the DC bus side to the battery side, the IGBT T_b should permanently remain off and the IGBT T_a has to be periodically made ON and OFF by a PWM strategy. The converter will act as a buck chopper with T_a and D_b as the active devices. Similarly, when the batteryis discharged, the IGBT T_a should permanently remain off and the IGBT T_b should be periodically made ON and OFF by a PWM strategy, so that the converter will act as a boost chopper with T_b and D_a acting as the active devices.

Generally, the mode of charging and discharging of any battery depends on the SOC level. the two most common modes are: (i) Constant current mode of charging, at low levels of SOC, i.e. terminal voltage of battery becomes too low and, (ii) Constant voltage mode of charging, when terminal voltage of the battery has almost come up to its rated value.

A DC-DC converter is inherently nonlinear due to its switching devices. In order to design a controller with existing linear control system tools to obtain required steady state and transient responses, the power stage including the output filter has to be linearized using the state-state averaging method [94, 95]. As the main focus of this study is DC fast charging of electric vehicle, analysis is presented here only for the adjustable current

charging mode. Therefore, the transfer function $G_1(s)$ of the power stage reflects the relation between output current and duty ratio and is given in (2.57).

$$G_1(s) = \frac{\tilde{\quad}}{\tilde{\quad}} = \frac{V_{DC}}{R_1 L_1 C_1} \frac{C_1 r_{C1} s + 1}{s^2 + \left[1/C_1 R_1 + \left(r_{C1} + r_{L1}\right)/L_1\right] s + 1/L_1 C_1} \tag{2.57}$$

$\tilde{\quad}$ and $\tilde{\quad}$ represent small AC disturbance of the output current and duty ratio of the converter respectively. R_1 is considered as a conceptual output resistor (output power equivalent) to represent the load effect of the battery. L_1 and C_1 are the filter inductor and capacitor of the DC-DC converter. R_{C1} and R_{L1} are the internal resistances of the filter inductor and capacitor. As shown in the system transfer function in (2.57), the system response changes as the load resistor i.e. charging/output power varies. The converter frequency response under power outputs of 4 kW, 6 kW, 8 kW and 10 kW is shown in

Figure 4-10. During discharging, the battery side is the input end of the DC-DC converter and the high voltage DC link is the output. Similar to the charging case, the state-state averaging method is applied to model the power stage including the output filter [94, 95]. The transfer function $G_2(s)$ of the power stage that reflects the relation between input current and duty ratio is:

$$G_2(s) = \frac{\tilde{\quad}}{\tilde{\quad}} = \frac{V_{DC}}{R_2 C_2 L_2} \times \frac{R_2 C_2 s + 2}{s^2 + \left[1/C_2 R_2 + \left(r_{C2} + r_{L1} + D r_{Cdc}\right)/L_1\right] s + \left(1-D\right)^2 / L_1 C_2} \tag{2.58}$$

where $\tilde{\quad}$ and $\tilde{\quad}$ represents small AC disturbance of the output current and duty ratio of the converter during discharging. C_2 is the total capacitance and r_{C2} is the total ESR at the DC link. R_2 is considered a fictitious output resistor to represent the input effect of the battery discharging to the grid. The system response changes as the load resistor i.e.

output power and duty ratio varies. The converter frequency response under battery discharging power of 4 kW, 6 kW, 8 kW and 10 kW is presented in Figure 4-11.

The models of the two converter power stages have been formulated, and their Bode plots are presented in Figure 4-10 and Figure 4-11. Based on these models, the current regulator system for the bidirectional DC-DC converter is illustrated in Figure 4-12. $G_1(s)$ and $G_2(s)$ represent the converter power stages during charging and discharging as shown in (2.57) and (2.58). The pulse width modulation results in an additional constant gain which is represented as the pulse width modulator in Figure 4-12. It is incorporated with each of the transfer functions for the two converter power stages [94]. PI (proportional-integral) controllers, denoted as $G_{c1}(s)$ and $G_{c2}(s)$, are employed for the DC-DC converters. The proportional gain and the integral gain for these two controllers are obtained using the methodology mentioned below:

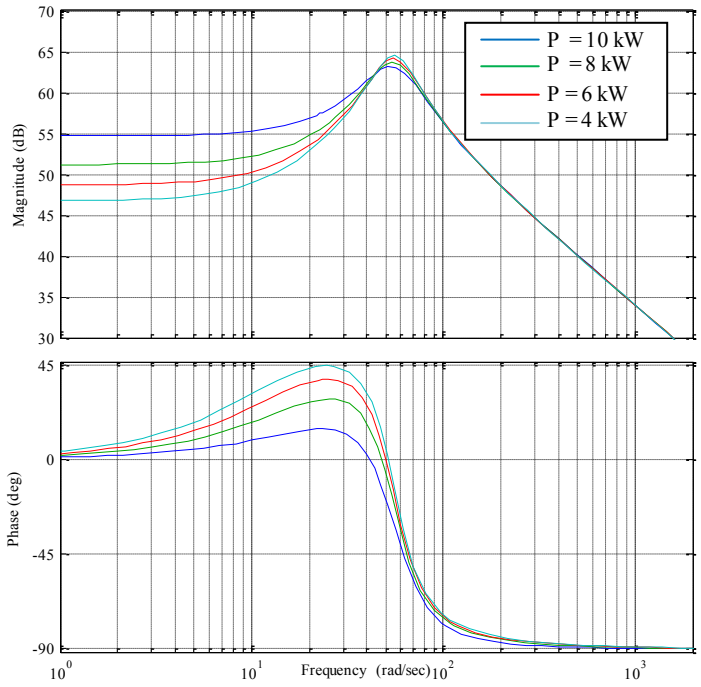

Figure 4-10. Converter frequency response. (a) Gain plot of DC-DC converter at different battery charging power in dB. (b) Phase plot of DC-DC converter I at different output power, i.e. phase angle in degrees.

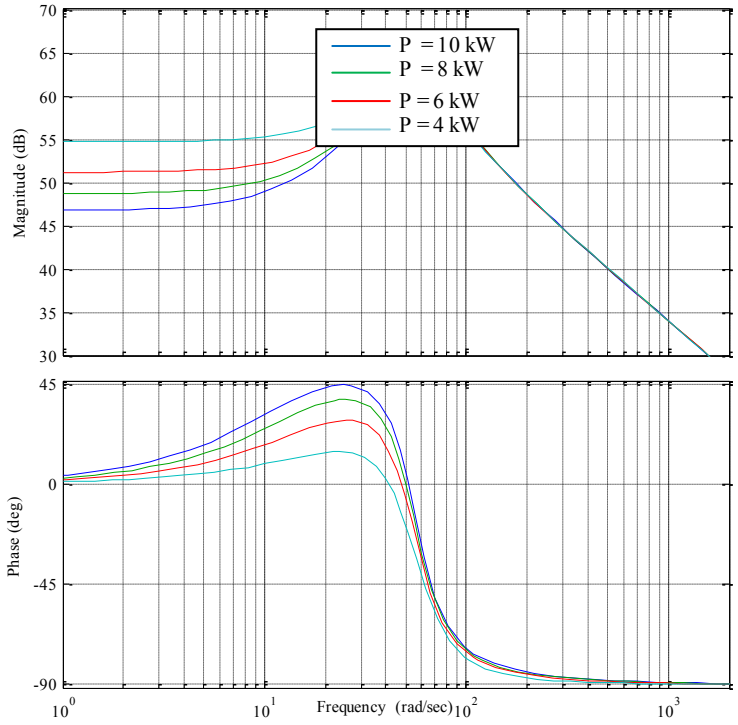

Figure 4-11. Converter frequency response. (a) Gain plot of DC-DC converter at battery discharging power in dB. (b) Phase plot of DC-DC converter I at varying output power, i.e. phase angle in degrees.

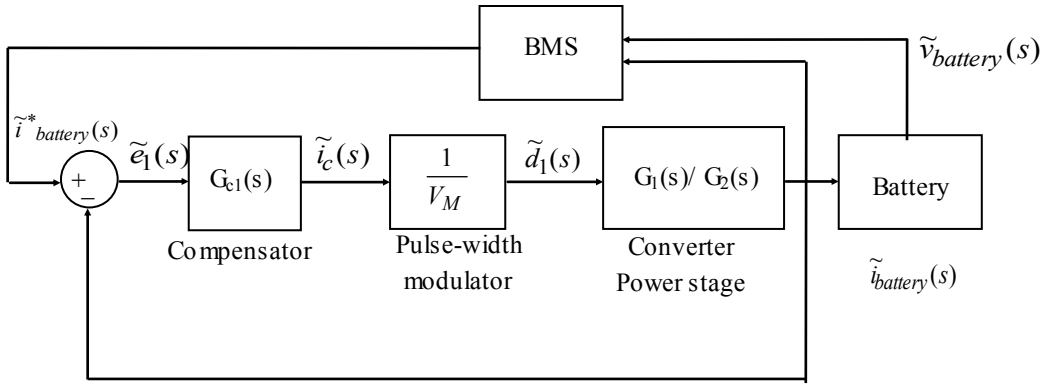

Figure 4-12. Current regulator system small-signal model of the DC-DC converter in the battery side.

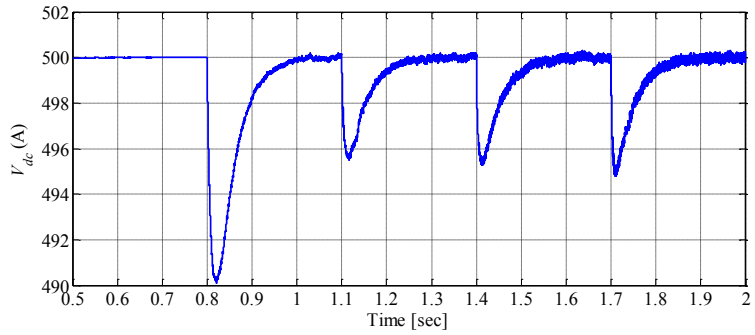

(a)

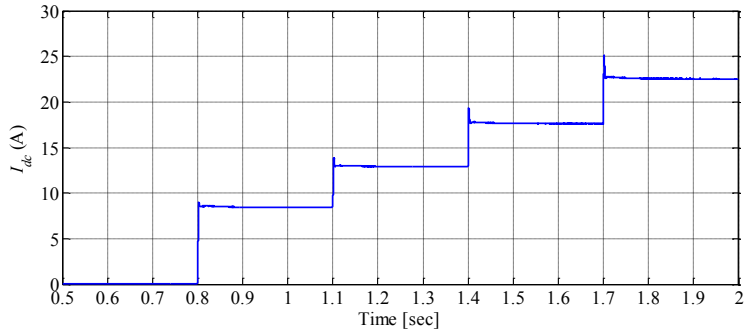

(b)

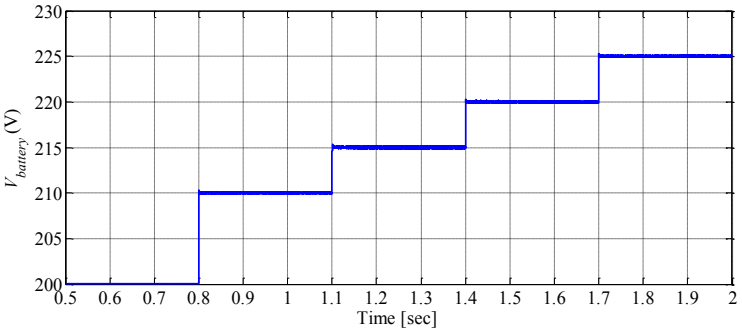

(c)

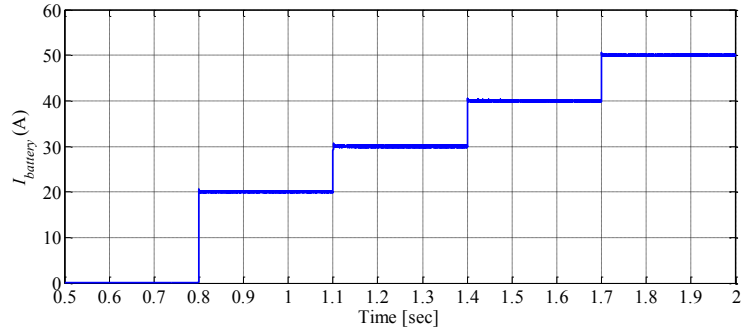

(d)

Figure 4-13. DC-DC converter response during G2V operation at different power level.

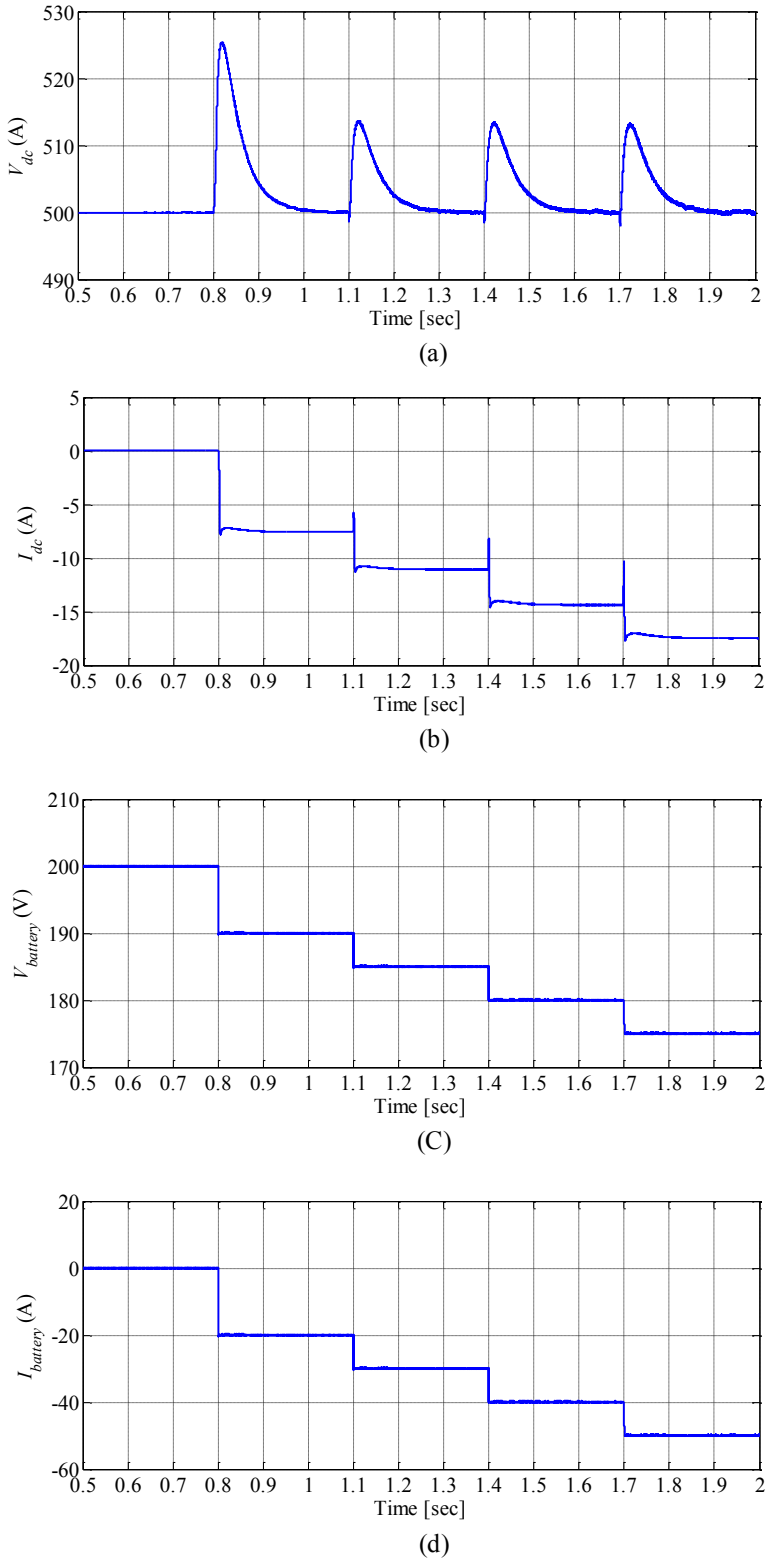

Figure 4-14. DC-DC converter response during V2G operation at different power levels.

For each DC-DC converter, the gain crossover frequency (GCF) of the total forward path transfer function (consisting of the controller, PWM modulator and the DC-DC converter power stage) is chosen as one-tenth of the switching frequency of the respective converter. The highest value of GCF, which is obtained for multiple steady state operating points, about which perturbations are introduced, is finally taken. A phase margin of 55 degrees is chosen for the total open loop forward path transfer function for each of the operation mode of the DC-DC converter.

The battery is modeled as a constant DC source in series with an internal resistance. The high voltage side of the DC-DC converter is initially charged to a voltage level of 500 V using the VSC connected to the grid. After the high voltage DC link is established, depending on the switching strategy explained earlier, the DC-DC converter will facilitate G2V or V2G operations. The waveforms illustrated in Figure 4-13 and Figure 4-14 depict the operation of the bi-directional DC-DC converter during charging and discharging at different power throughput levels. The initial battery voltage is considered 200 V for both cases. At the time instant of 0.8 sec, 1.1 sec, 1.4 sec and 1.7 sec, the reference charging/discharging current of the battery is set to be 20 A, 30 A, 40 A and 50 A for a power level of around 4 kW, 6 kW, 8 kW and 10 kW respectively.

Figure 4-13(a) is the DC link voltage. Before the time instant of 0.8 sec, the DC link voltage is maintained as 500 V by the grid side converter acting as a three-phase rectifier. At every instant that the output power of the DC link increases, the voltage drops slightly due to the dynamics of the controller and quickly regains to the set value. Figure 4-13(b) is the average output current from the DC link to the battery. The current amplitude depends on the load power demand of the battery and it is used to generate the reference *d*-axis current control. Detailed controller design will be explained in the next section.

Figure 4-13(c) and (d) are the battery voltage and current during charging. The current is positive as the defined positive direction is from grid to vehicle. The controller has excellent dynamic and steady state performance as the actual current reaches the reference in a short time with no steady state error. Figure 4-14 shows voltage and current waveforms of the bidirectional DC-DC converter which acts as a boost converter to transfer power from the battery (low voltage) side to the DC link (high voltage) side

during vehicle to grid operation. It can be seen that initially the voltage is set to be 500 V before the battery sends power to the grid. At the instant that the battery output current increases, the DC link voltage rises due to the dynamics of the system and quickly returns to the reference level maintained by the grid side VSC. The battery current is negative, opposite to the defined positive direction of the current, which means the current is flowing from the battery side to the grid side. The voltage ripple on the battery side of the bidirectional DC-DC converter, i.e. ΔV_{C1}, is smaller than 5% of the maximum battery voltage and the inductor ripple current, i.e. ΔI_{L1}, is 20% of the battery current, which satisfy the battery charging/discharging requirement states in [95].

4.4.2 Bidirectional DC-AC/AC-DC Converter

The IGBT-based VSC has a bank of electrolytic capacitors (equivalent capacitance C) at its DC side and a bank of AC chokes (R_s and L_s represent the loss-emulating component and the inductance value of each choke) connected between its AC side and the grid. This arrangement makes the VSC act as a boost converter, whose DC link voltage would be controlled at 500 V DC, which is much greater than the peak of the AC side line-to-line voltage. A 20 A DC current at 500 V corresponds to 27.76 A line current at the 208 V AC side at unity power factor, which will be maintained by properly controlling the switching of the IGBTs of the VSC [68, 69]. Total Harmonic Distortion (THD) in the current is expected to be within 5% as per *IEEE* 519 standard.

The analysis and the real-time control strategy is based on the decoupled *dq* theory [96] in Park's reference frame, as is generally done for achieving high performance control of AC electrical machines. An equivalent star-connected system is assumed. The voltage equations for the circuit consisting of the grid, the AC choke and the AC side terminals of the VSC (Figure 4-4) in the synchronously rotating *dq* frame, based on the Kirchoff's voltage law are:

$$v_{sd} = R_s i_{std} + L_s \frac{di_{std}}{dt} - \omega L_s i_{stq} + v_{cond} \tag{2.59}$$

$$v_{sd} = R_s i_{std} + L_s \frac{di_{std}}{dt} - \omega L_s i_{stq} + v_{cond} \tag{2.60}$$

where, v_{sd}, v_{sq} are d- and q-axis components of the utility voltage, i_{std}, i_{stq} are the corresponding components of the grid-converter currents (grid to converter side assumed positive), v_{cond}, v_{conq} are the corresponding components of the AC side terminal voltages of the VSC, R_s represents the per phase resistance representing the AC choke active power-loss, L_s represents the per phase inductance of the AC choke and ω represents the electrical synchronous utility frequency. The important equation in the DC side is:

$$i_{load} + C_2 \frac{dv_{dc}}{dt} = i_{dc} \tag{2.61}$$

where, i_{load} is the current flowing out of the capacitor to the battery (assumed positive convention), v_{dc} is the voltage across the capacitors at the DC bus of the VSC and i_{dc} is the DC link current of the VSC.

The utility voltage space vector is controlled to always remain oriented along the direct axis. This may be achieved by on-line monitoring of the utility voltages and employing a phase locked loop (PLL) [97] during hardware implementation. With this being achieved, the expressions for instantaneous active and reactive powers would become:

$$\left.\begin{aligned} p &= v_{sd} i_{std} = V_{bus} i_{std} \\ q &= -v_{sd} i_{stq} = -V_{bus} i_{stq} \end{aligned}\right\} \tag{2.62}$$

where, V_{bus} is the magnitude of the grid voltage space vector and is a constant under balanced conditions and powers from the grid to converter side are considered positive. It appears that if i_{std} and i_{stq} are controlled independently, the active power and the reactive power can be controlled independently by controlling i_{std} and i_{stq} respectively. Although this seems to provide a decoupled control of active and reactive power flow, it actually does not, as a cross-coupling effect exists between d- and q-axis variables if (2.62) is examined closely. This calls for development of a proper feed-forward control which would truly yield a decoupled control of real and reactive power flow.

With the feed-forward control in place, the s-domain block diagram of the d- and the q-axis current control loops is shown in Figure 4-15 where, K_{pd}, K_{id} are the d-axis proportional-integral (PI) current controller parameters and K_{pq}, K_{iq} are the q-axis current

controller parameters. These two unknown controller parameters for either *d*- or *q*-axis are designed in this work based on:

- Cancellation of the pole of the respective plant with the zero of the respective PI controller, in either of Figure 4-15(a) or (b).
- Assumption of a bandwidth of 500 Hz for the current control loop, to be at least an order of magnitude less than the sinusoidal pulse width modulation (SPWM) carrier frequency of 10 kHz that has been considered in this work.

The values obtained after calculations are: K_{pd}=K_{pq}=79 and K_{id}=K_{iq}=787. The reference value of *q*-axis current (i_{qs}*) should be maintained at zero throughout as power injected to the grid or from the grid is optimum if the power factor at the grid is maintained unity. This is desired both from the point of view of optimizing battery resources as well as from the point of view of excellent power quality of the currents drawn from or injected to the grid. It is desired that i_{qs} should track i_{qs}* with zero steady state error, low overshoot and within a reasonably fast settling time. The reference *d*-axis current (i_{ds}*) should be such as to keep the DC link voltage constant at a value much above the amplitude of the utility line voltage, regardless of different values of battery charging currents. This is to ensure that the VSC acts as a boost converter so that lower order harmonics do not appear in the grid-to-converter or converter-to-grid currents and hence good power quality is ensured.

The *d*-axis current controls active power flow in between the grid and the VSC. Considering power balance between the DC side and the AC side of the VSC, this power should therefore be directly related to the DC side battery charging/discharging power, the losses in the inverter devices, AC chokes and the stored energy in the DC link capacitor. A proper DC link voltage controller is therefore mandatory to regulate the DC link capacitor voltage. The DC link voltage control loop should therefore be an outer loop with a lower bandwidth and the DC link voltage controller output should produce the requisite amount of *d*-axis current reference of the VSC in order to maintain the required boosted voltage level across the DC link capacitor under varying charging/discharging currents.

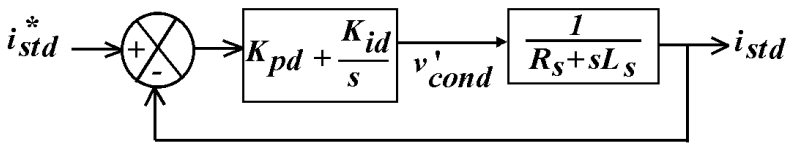

(a)

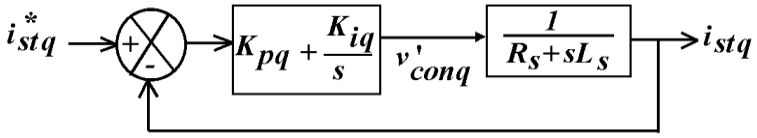

(b)

Figure 4-15. The *s*-domain block diagram of the decoupled current control loop for the three-phase battery charger. (a) *d*-axis. (b) *q*-axis.

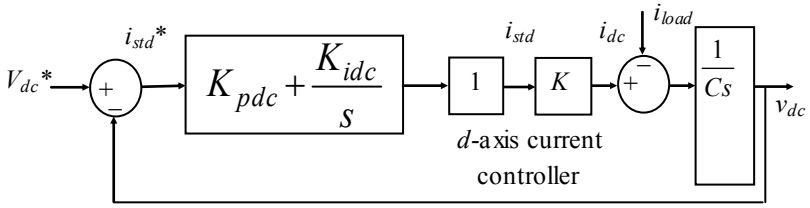

Figure 4-16. The *s*-domain block diagram of the outer DC link voltage control loop for the three-phase battery charger.

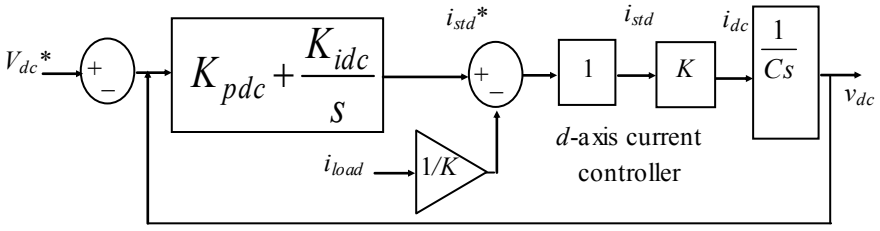

Figure 4-17. The reduced *s*-domain block diagram of the outer DC link voltage control loop for the three-phase battery charger for Figure 4-16.

The *d*-axis current control loop has to be an inner loop and its bandwidth is much larger compared to the outer DC link voltage control loop. The *s*-domain block diagram of the DC link voltage control loop is presented in Figure 4-16. The DC link voltage PI controller parameters have been determined considering another feed-forward technique to reduce the *s*-domain block diagram of Figure 4-16 to that of Figure 4-17. The bandwidth of the voltage control loop has been assumed to be 50 Hz, which is one order lower than the bandwidth of the inner *d*-axis current control loop. It is for this reason that the inner *d*-axis current control loop has been represented as a block with unity gain in

Figure 4-16 or Figure 4-17. The DC link voltage reference has to be set at 500 V DC, as discussed earlier.

In Figure 4-16 or Figure 4-17, 'K' is the ratio of the magnitude of the utility voltage space vector and the value of the DC link voltage. It is noteworthy that when the battery charging or discharging current changes (i_{load}), the DC current flowing in the DC link capacitor of the VSC should ideally be zero, to ensure that the DC link voltage remains constant. This is essential to achieve a fast dynamic response and close to unity power factor operation. This depends on the controller tuning and a proper on-line estimation technique to determine the value of 'K' in the transient condition.

The block diagram for the comprehensive control technique is presented in Figure 4-18. The grid line voltages are fed back to the controller for on-line generation of the unit vectors (cos ωt and sin ωt). These are required for maintaining orientation of the grid voltage space vector in the synchronously rotating reference frame and on-line computation of the d- and q-axis components of the grid voltages and similar components for the currents between the grid and the VSC. The control structure initiates with the reference value of the DC link voltage (V_{dc}*) and the q-axis reference current (i_{stq}*). They are set at 500 V and 0 respectively.

The actual DC link voltage (v_{dc}) is monitored on-line, fed back and compared with the reference value and the error is generated. This error is fed to a PI DC link voltage controller whose output generates the necessary d-axis current reference to ensure constant DC link voltage, after adding a fraction of feed-forward compensation obtained from on-line monitoring of the battery charging or discharging current. This d-axis current reference is compared with the actual d-axis current which is computed on-line and from measured AC side line currents of the VSC. The error is fed to the d-axis PI current controller to ensure that the actual current tracks the reference. This PI controller output is added with the feed-forward obtained from on-line computation of the cross-coupling terms of (2.59) (V_{bus} and $\omega L_s i_{stq}$ with proper signs) to derive the necessary reference value of d-axis voltage component at the VSC AC terminals (v_{cond}).

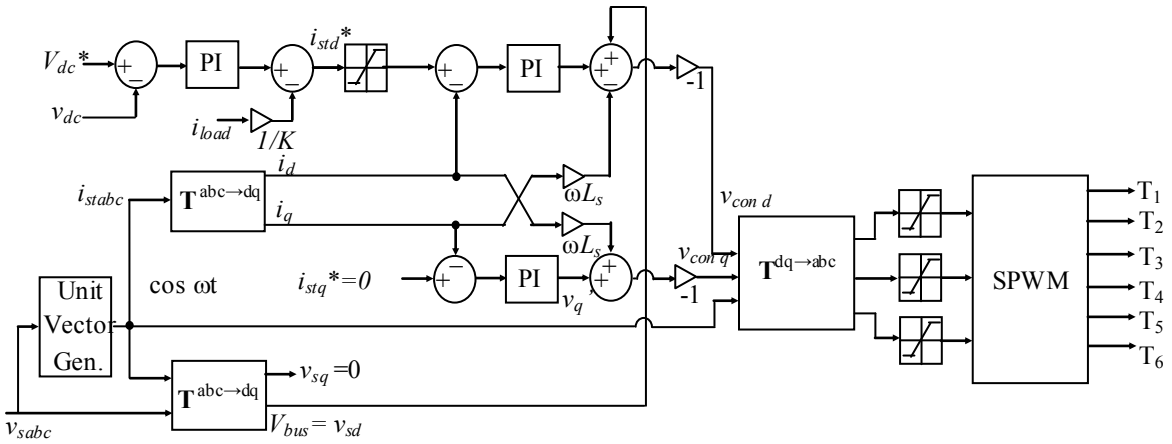

Figure 4-18. Overall block diagram showing the comprehensive control technique.

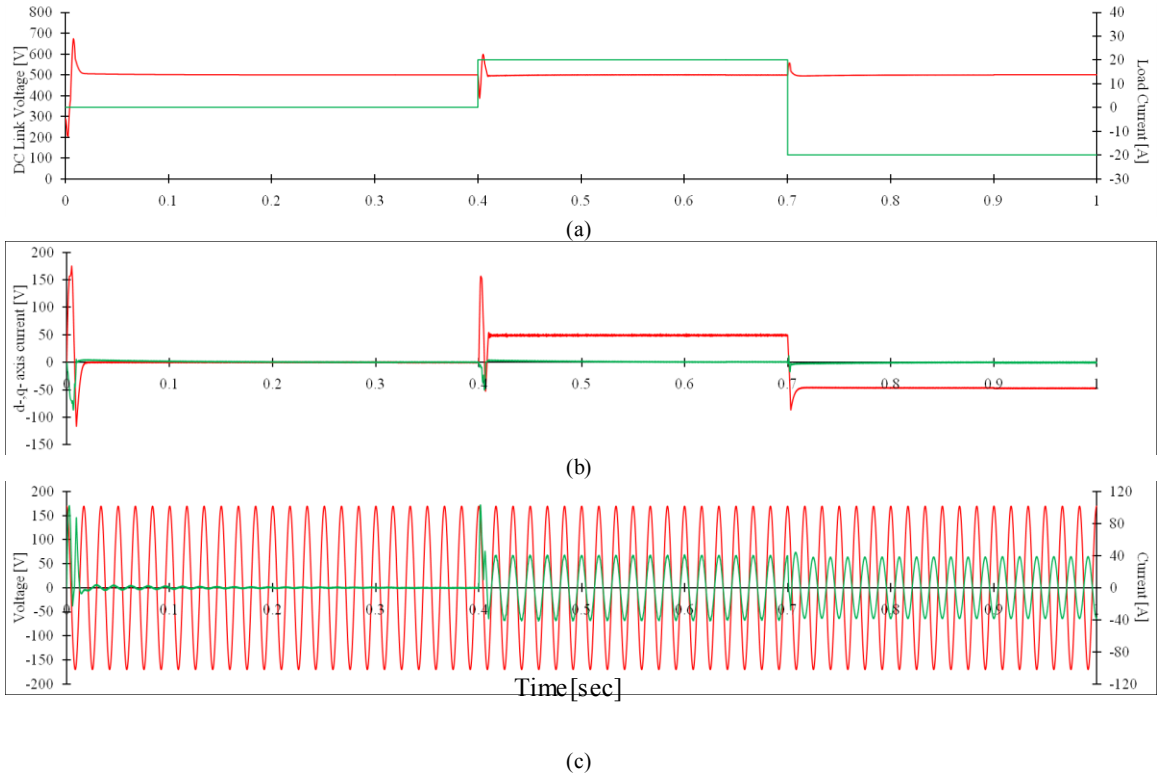

Figure 4-19. Calculated results illustrating the performance of the developed high performance level 3 bi-directional battery charger. (a) DC link voltage and current waveforms (b) *d*- and *q*- axis grid currents (c) Grid phase voltage and phase current.

A similar task is performed in the q-axis current-control loop and its PI controller output is added with the cross-coupling terms of (2.60) ($\omega L_s i_{std}$ with proper signs) to derive the necessary reference value of q-axis voltage component at the VSC AC terminals (v_{conq}).

The necessary three-phase reference voltages required for the SPWM strategy in the *abc* frame are computed on-line from v_{cond} and v_{conq} with the help of the on-line unit vectors. The SPWM is considered to have a carrier frequency of 10 kHz considering the IGBTs proposed at the 10 kW, 500 V DC power level. The comparator outputs of the SPWM strategy form the desired switching signals of the IGBT's of the VSC to finally achieve the desired performance of the converter system.

The waveforms illustrated in Figure 4-19(a) to (c) which depict the performance of the charger, are corresponding to the following operating conditions:

At the uncharged state of the DC link capacitor, initially it is ensured that the battery does not draw any current. The DC link electrolytic capacitor bank is to be first 'pre-charged' from an uncharged state to a level close to the peak value of the grid line voltage. Then, the DC link voltage reference of 500 V DC is given to the controller so that the switching of the IGBT's in the VSC start and the DC link capacitor voltage starts boosting. This is considered as the 'time=0' instant in the presented waveforms. After 0.4 seconds from this instant, a constant battery charging current of 20 A is drawn as a step input from the charger to examine the high performance of the VSC under G2V operation. At time = 0.7 second, a negative step battery current of 20 A is drawn, mimicking the effect of V2G operation. The waveforms under this testing condition are presented next.

Figure 4-19(a) shows the DC link voltage waveform with time. It is seen to settle at the reference value within 15 ms after an overshoot well within 800 V, which is considered as the safe DC bus voltage level, as mentioned earlier. It is found to undergo minimal changes at the instants of introduction of the battery charging/discharging current. The overshoot in the dynamics is within safe limit, the settling time is low enough and the DC link voltage restores to the reference value. This has only been possible due to proper design of the DC link voltage control loop, the d-axis current control loop and proper evaluation of the constant 'K'.

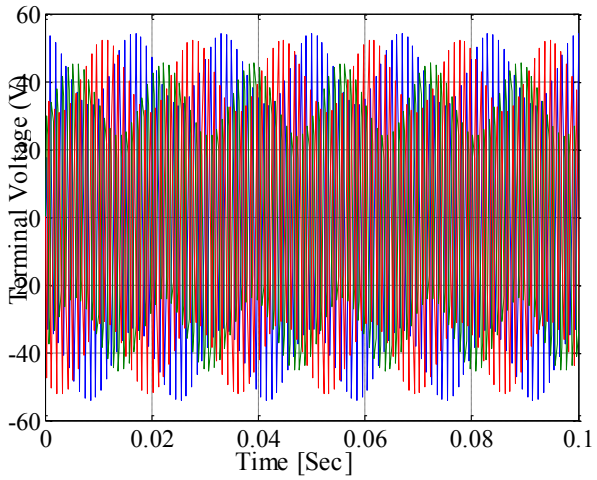

(a)

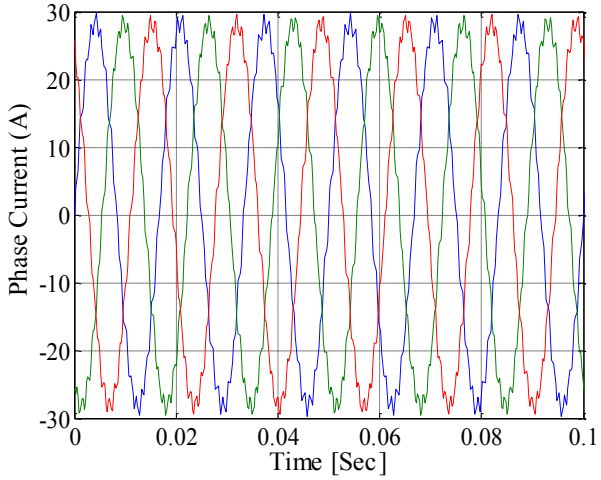

(b)

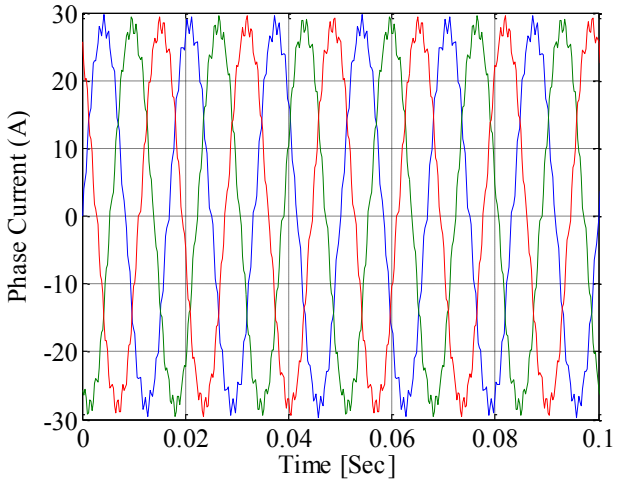

(c)

Figure 4-20. Machine terminal voltage and current during integrated charging, (a) Terminal phase rms voltage. (b) Per phase current when θ_r=0°. (c) Per phase current when θ_r=45°.

Figure 4-19(b) shows the i_{std} and i_{stq} waveforms of current with time, under the same testing condition. The average value of the i_{stq} waveform is found to remain almost at zero all throughout, tracking its reference value (i^*_{qs} kept at 0). This ensures near unity power factor operation. The i_{std} changes depending on the requirement to maintain proper DC link voltage. Figure 4-19(c) shows the *a* phase grid current and the corresponding *a* phase voltage waveform (equivalent star connected system). It is found that the distortions in the current is minimal, almost near unity power factor is achieved regardless of the battery current is positive or negative. Additionally, the transition from a positive power flow to negative power flow ensuring unity power factor occurs in few milliseconds. All these waveforms prove the soundness of the implemented vector control strategy of the battery charger [69].

Figure 4-20 indicates the electrical characteristic of the machine during integrated charging. Three-phase currents are balanced irrespective of the rotor position. The machine terminal voltage has high frequency ripple due to the PWM switching during charging. The amplitude of the fundamental voltage is significantly lower than the rated machine voltage, the current through the machine armature during charging or discharging never exceeds the rated current and its fundamental is always at the utility power frequency with little PWM ripples of the high switching frequency; thus the machine has not been found to rotate.

4.5 Real-time Simulation of the Three-phase Bidirectional Charger

In order to study the performance of the developed charging strategy, experiments were performed on the BEV available at the laboratory and a range of charging characteristics were measured between its safe discharging voltage and its rated voltage. The vehicle under study has six 12 V lead-acid batteries in series, therefore $V_{battery}$ is equal to 72 V. The vehicle was charged using the on-board charger installed in the vehicle supplied by the utility grid. These experiments were performed to obtain the DC reference current and voltage dictated by the battery management system.

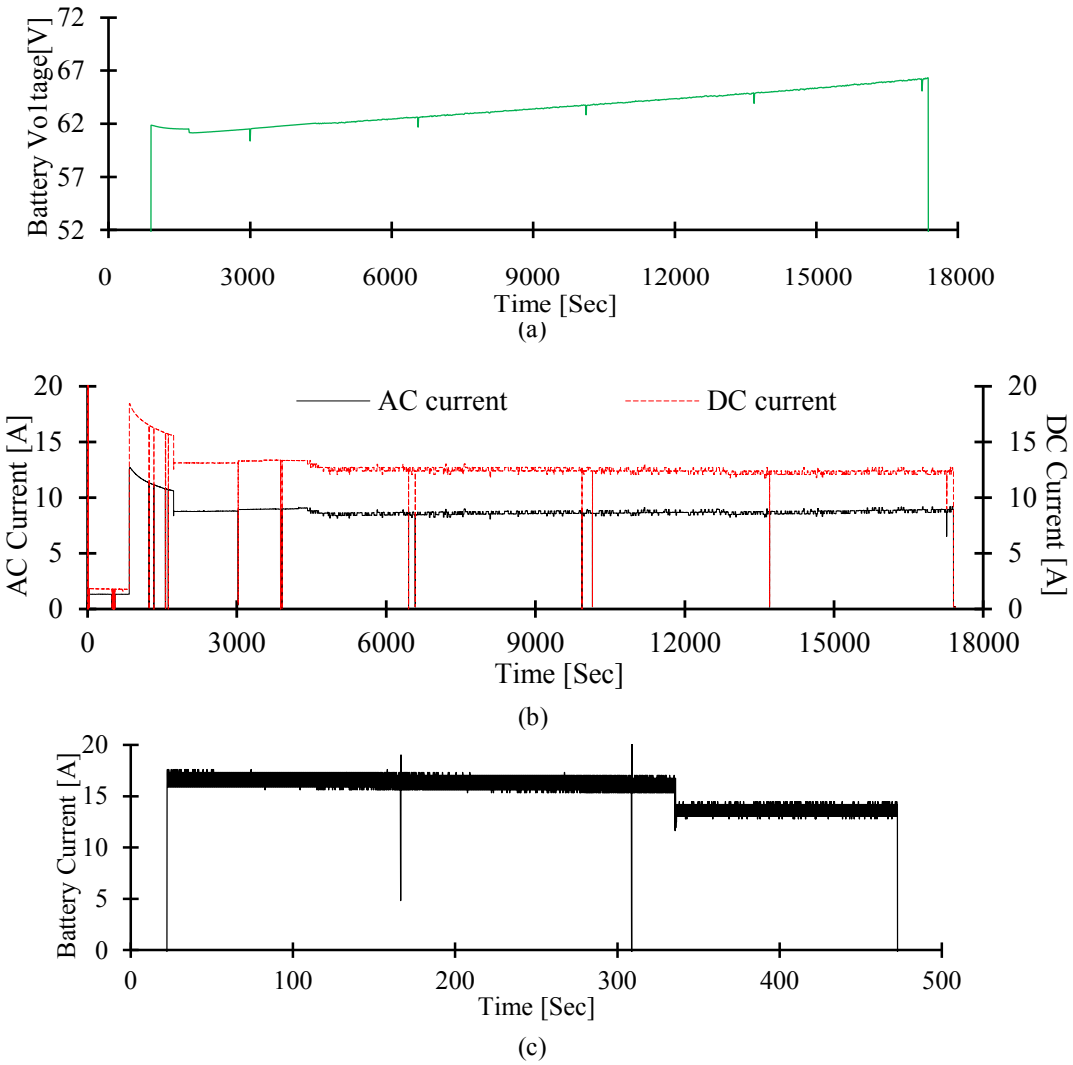

Figure 4-21. Measured lead-acid battery characteristics using the charger on-board the battery electric vehicle. (a) Battery voltage. (b) rms values of AC and DC currents. (c) The battery current characteristics that are used to replicate the reference current for the developed charging system.

Figure 4-21(b) shows the measured DC and the corresponding AC currents while charging. Through experimentation it was found that it would be sufficient to use such a DC current trend as shown in Figure 4-21(c) as the reference current for testing the developed DC fast charging station. Moreover, it replicates a unit step. Note that this profile will be used for the battery charging reference for V2G operation; this vehicle voltage level is not high enough for a single-level DC-DC converter topology. Another DC-DC converter to step up the voltage level needs to be added.

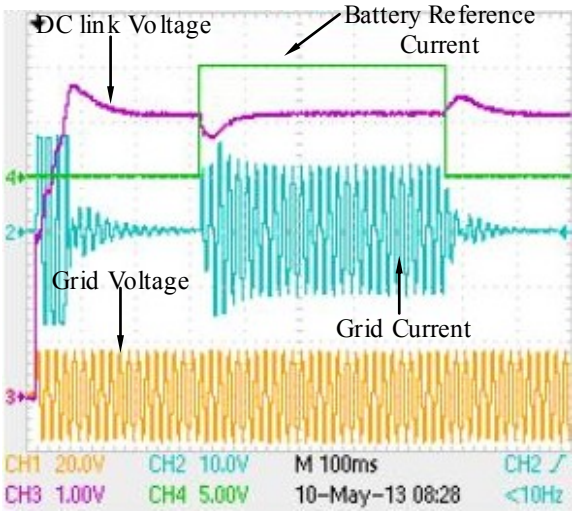

(a)

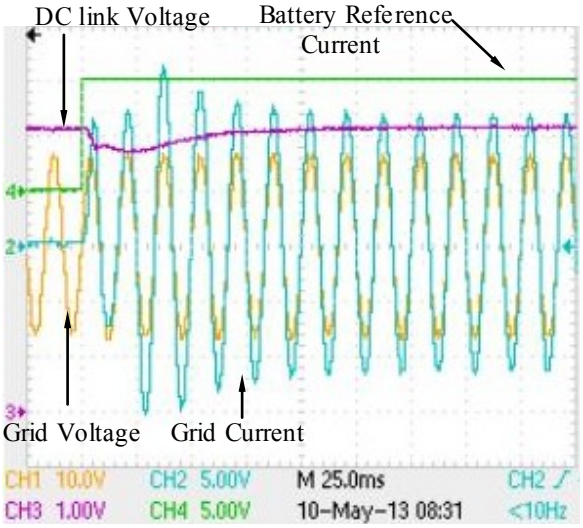

(b)

Figure 4-22. (a) Measured current and voltage waveforms during charging under grid only mode. Multiplication factors: DC link voltage (100V/Unit), Grid current (17A/Unit), Grid voltage (100V/Unit), Battery reference current (40A/Unit). (b) Near unity power factor achieved.

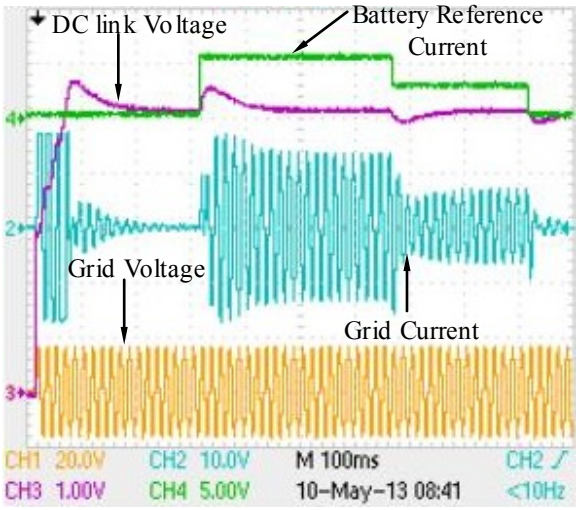

(a)

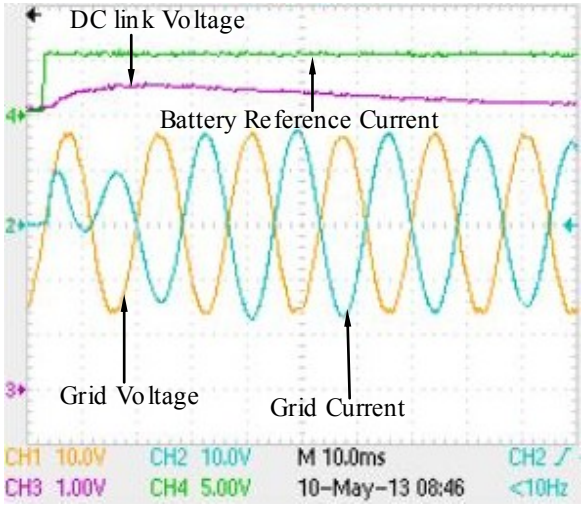

(b)

Figure 4-23. (a) Measured current and voltage waveforms under vehicle to grid condition. Multiplication factors: DC link voltage (100V/Unit), Grid current (28A/Unit), Grid voltage (100V/Unit), Solar PV reference current (20A/Unit). (b) Near unity power factor achieved.

In this study, a voltage level of 200 V during V2G operation is considered. Comprehensive testing of the designed charging system has been performed using a real-time environment setup consisting of an FPGA based Opal-RT real-time control platform and Tektronix Digital Oscilloscope. Figure 4-22(a) and (b) show measured results obtained from the Tektronix Oscilloscope under such a situation. As it can be seen in Figure 4-22(a), initially, it was assumed that the DC link capacitor is in a completely uncharged state and it was charged from the grid once the station was powered on. The

DC link voltage reference of 500 V DC is given to the controller so that the switching of the IGBTs in the VSC start and the DC link capacitor voltage starts boosting. This is considered as 'time=0' instant in the presented waveforms in this section.

Around 0.3 seconds after the DC link voltage has reached a steady state voltage, the car battery is connected to the DC charging station for charging. The battery consumes around 80 A in a step at a battery pack voltage of 66 V. These conditions were chosen based on the specifications of the lead acid battery pack present in the in-house electric vehicle which is rated at 72 V and 100 Ah. A charging current of 80 A is provided to the battery at a voltage of 66 V. Around 0.3 seconds it can be seen that the grid current increases due to the load demand and stabilizes to a value around 14.7 A rms as the DC link voltage stabilizes. The charging was stopped around 0.75 seconds and the grid current reaches zero. In Figure 4-22(b) current that flows out of the grid is considered positive and it can be seen that almost near-unity power factor is also achieved even under loading conditions with minimal perturbation in the power factor.

Similar to Figure 4-22, here also the DC link capacitor is assumed to be uncharged and then charged to around 500 V. Once the DC link voltage has reached steady state the intermittent vehicle to grid power flow is initiated. At around 0.3 seconds, high battery discharging was emulated as a result of which around 28 A rms of current was fed back to the grid. At this condition the battery side voltage and current were found to be 210 V and 47.6 A. Again at around 0.75 seconds the battery power input reduced and the grid current decreased to around 14 A rms. At this condition the vehicle side voltage and current were found to be 105 V and 24 A. In all cases, from Figure 4-23(a), it can be seen that the grid voltage remained a constant and the DC link voltage and the grid current link stabilized to reference values within a short period of time. Moreover, it can be seen from Figure 4-23(a) and (b) that regardless of the direction of power flow, unity power factor is ensured in a few milliseconds post perturbation. All these waveforms prove the soundness of the implemented vector control strategy of the battery charger.

4.6 Conclusion

In this chapter a three-phase bidirectional charging strategy was introduced using the existing traction components of an electrified vehicle, which include power electronic converters and the electric motor. The unbalanced condition caused by the buried magnets can be mitigated by the damper in the rotor and therefore, the machine windings can be used as line inductors for grid side converter. Both V2G and G2V operations are considered in this study. Modeling of the power stage of the converters during charging and discharging is discussed and the control strategy is developed while maintaining satisfactory ripple voltage and current on the battery side as well as unity power factor and low THD of the grid current. Experiments were performed using an in-house battery electric vehicle for reference purpose. Real-time simulation studies were done to verify the performance of the integrated charger.

Chapter 5

Conclusions and Suggested Future Work

5.1 Conclusions

PMSMs are generally chosen as the traction motor for EVs because of their high torque density, high power density, compact size and high efficiency. In this research, an interior permanent magnet synchronous machine with a special damper is proposed for this purpose. A dynamic model based on reference frame theory of the proposed machine is developed and validated. Parameter determination methods are additionally proposed, established and verified to experimentally measure the equivalent circuit parameters. A comparative study of a PMSM and the proposed machine of similar size/rating with a special damper is conducted under a square wave self-controlled inverter driven condition. It is shown that the machine with a damper has faster dynamic performance than the original machine especially in the high speed region. Under a three-phase symmetrical fault, the damper contributes to the fast rising and falling of the phase current, thereby, decreases the protective relay or contactor response time and lowers the risk of demagnetization of the machine. Furthermore, the machine is considered for integrated charging. For this purpose, the damper is effective in mitigating the problems caused by the saliency due to the buried magnets. It ensures that the machine offers three-phase balanced impedances during both V2G and G2V operations. The existing inverter power stage in the vehicle can be retained for charging purposes and control strategies involving balanced cases may be sufficient. The findings in this study are supported through simulations and experimental results.

The contribution of this work can be summarized as follows:

- A comprehensive experimental and theoretical investigation of the EV and HEV load profile and charging profile was completed [4, 11, 75];

- The effects of adding a damper to interior PMSM to improve dynamic performance and short circuit response were analyzed in detail;
- A model and a novel parameter determination method for its parameters was developed for an PMSM with a non-symmetrical damper. This model was validated through simulation and experiment [64-66, 98];
- A bi-directional integrated charger for both vehicle-to-grid and grid-to-vehicle operations was developed using an IPMSM with a damper [68, 69].

5.2 Suggested Future Work

Some ideas are presented in this section highlighting suggested extensions of the work in this research area. Key elements are described as follows:

Further performance analysis of the proposed machine with its damper are to be performed. An investigation of the space harmonics caused by the machine, ripple components, detailed efficiency mapping and other machine characteristics is needed.

It is assumed that under steady state, the total torque is developed only by the PMs. However, the total torque under dynamic conditions is the combination of the PM torque and the cage torque. A control method to maximize the developed torque for the proposed machine with damper will be of great value.

It is shown in this study that by adding a damper, the IPMSM can be used for integrated charging. The damper parameters are chosen through numerical investigation based on a *dq* axis model. The optimized design of such a machine to maintain satisfactory efficiency during both motoring and integrated charging is of paramount importance for future study. Moreover, practical design of the damper to achieve the required parameters needs to be initiated.

It is seen that during charging conditions, the currents in the machine windings result in the development of torque in the machine. The torque is significantly smaller than the starting torque, and hence the machine does not rotate. However, this developed torque

causes small noise and vibrations. It is advised to further investigate this issue to reduce the resultant torque of the machine at this standstill condition.

For any grid connected system, it is necessary to provide power quality monitoring and fault detection capability to ensure the healthy operation of the system such that it does not influence the stability of the grid. Moreover, as the number of vehicles that are connected to the grid increases, the load optimization at the grid level needs to be considered.

BIBLIOGRAPHY

[1] "CO2 Emissions from Fuel Combusion Highlights," International Energy Agency, France, 2013.

[2] "2013 World Oil Outlook," Organization of the Petroleum Exporting Countries (OPEC) Secretariat, Austria, 2013.

[3] "Global EV Outlook Understanding the Electric Vehicle Landscape to 2020," International Energy Agency, France, 2013.

[4] Y. Li, X. Lu, and N. C. Kar, "Rule-based Control Strategy with Novel Parameters Optimization Using NSGA-II for Power Split PHEV Operation Cost Minimization," *IEEE Transactions on Vehicular Technology,* 2014.

[5] C. C. Chan and K. T. Chau, *Modern Electric Vehicle Technology*. New York, USA: Oxford University Press, 2001.

[6] K. Kamiev, J. Montonen, M. P. Ragavendra, J. Pyrhonen, J. A. Tapia, and M. Niemela, "Design Principles of Permanent Magnet Synchronous Machines for Parallel Hybrid or Traction Applications," *IEEE Transactions on Industrial Electronics,* vol. 60, pp. 4881-4890, 2013.

[7] A. Emadi, "Handbook of automotive power electronics and motor drives," ed Florida, USA: Taylor & Francis, 2005.

[8] C. C. Chan, "The State of the Art of Electric, Hybrid, and Fuel Cell Vehicles," *Proceedings of the IEEE,* vol. 95, pp. 704-718, 2007.

[9] I. Husain, *Electric and Hybrid Vehicles: Design Fundamentals*. Florida, USA: CRC Press, 2003.

[10] Z. Q. Zhu and D. Howe, "Electrical Machines and Drives for Electric, Hybrid, and Fuel Cell Vehicles," *Proceedings of the IEEE,* vol. 95, pp. 746-765, 2007.

[11] N. C. Kar, K. L. V. Iyer, A. Labak, X. Lu, C. Lai, A. Balamurali, *et al.*, "Courting and Sparking: Wooing Consumers Interest in the EV Market," *IEEE Electrification Magazine,* vol. 1, pp. 21-31, 2013.

[12] R. Krishnan, *Permanent Magnet Synchronous and Brushless DC Motor Drives*. Florida, USA: Taylor & Francis, 2010.

[13] V. T. Buyukdegirmenci, A. M. Bazzi, and P. T. Krein, "Evaluation of Induction and Permanent-Magnet Synchronous Machines Using Drive-Cycle Energy and Loss Minimization in Traction Applications," *IEEE Transactions on Industry Applications,* vol. 50, pp. 395-403, 2014.

[14] *FOCUS Specifications* [Online]. Available: http://www.ford.com/cars/focus/specifications/view-all/

[15] *Compare 2014 Nissan Leaf® Versions & Specs* [Online]. Available: http://www.nissanusa.com/electric-cars/leaf/

[16] *Features & Specs: Mechanical/Performance* [Online]. Available: http://www.toyota.com/prius/features.html#!/mechanical_performance/1223/1225/1227/1229

[17] J. K. Tangudu, "On Modeling and Design of Fractional-slot Concentrated-winding Interior Permanent Magnet Machines," Electrical Engineering, University of Wisconsin-Madison, United States, 2011.

[18] G. Pellegrino, A. Vagati, P. Guglielmi, and B. Boazzo, "Performance Comparison Between Surface-Mounted and Interior PM Motor Drives for Electric Vehicle Application," *IEEE Transactions on Industrial Electronics,* vol. 59, pp. 803-811, 2012.

[19] A. Vagati, G. Pellegrino, and P. Guglielmi, "Comparison between SPM and IPM motor drives for EV application," in *Proceedings of International Conference on Electrical Machines (ICEM)*, 2010, pp. 1-6.
[20] P. S. Bimbhra, *Electrical Machinery*. New Delhi, India: Khanna Publishers, 2003.
[21] U. A. Bakshi and V. Bakshi, *Electrical Machines - II*. Pune, India: Technical Publications, 2009.
[22] M. Azizur Rahman and R. Qin, "A permanent magnet hysteresis hybrid synchronous motor for electric vehicles," *IEEE Transactions on Industrial Electronics,* vol. 44, pp. 46-53, 1997.
[23] Y. Honda, T. Higaki, S. Morimoto, and Y. Takeda, "Rotor design optimisation of a multi-layer interior permanent-magnet synchronous motor," *IEE Proceedings on Electric Power Applications,* vol. 145, pp. 119-124, 1998.
[24] J. Nerg, M. Rilla, V. Ruuskanen, J. Pyrhonen, and S. Ruotsalainen, "Direct-Driven Interior Magnet Permanent-Magnet Synchronous Motors for a Full Electric Sports Car," *IEEE Transactions on Industrial Electronics,* vol. 61, pp. 4286-4294, 2014.
[25] K. T. Chau, J. Z. Jiang, and W. Yong, "A novel stator doubly fed doubly salient permanent magnet brushless machine," *IEEE Transactions on Magnetics,* vol. 39, pp. 3001-3003, 2003.
[26] B. Stumberger, A. Hamler, M. Trlep, and M. Jesenik, "Analysis of interior permanent magnet synchronous motor designed for flux weakening operation," *IEEE Transactions on Magnetics,* vol. 37, pp. 3644-3647, 2001.
[27] R. Dutta and M. F. Rahman, "A segmented magnet interior permanent magnet machine with wide constant power range for application in hybrid vehicles," in *Proceedings of IEEE Conference on Vehicle Power and Propulsion*, 2005, p. 6 pp.
[28] L. Parsa and H. A. Toliyat, "Fault-Tolerant Interior-Permanent-Magnet Machines for Hybrid Electric Vehicle Applications," *IEEE Transactions on Vehicular Technology,* vol. 56, pp. 1546-1552, 2007.
[29] Z. Ping, S. Yi, Z. Jing, T. Chengde, T. A. Lipo, and W. Aimeng, "Investigation of a Novel Five-Phase Modular Permanent-Magnet In-Wheel Motor," *IEEE Transactions on Magnetics,* vol. 47, pp. 4084-4087, 2011.
[30] S. S. Maroufian and K. Abbaszadeh, "Design and torque optimization of a PM Synchronous Motor, using an auxiliary winding," in *Proceedings of Power Electronics, Drive Systems and Technologies Conference (PEDSTC)*, 2014, pp. 574-578.
[31] Y. Pang, Z. Q. Zhu, and D. Howe, "Analytical determination of optimal split ratio for permanent magnet brushless motors," *IEE Proceedings on Electric Power Applications,* vol. 153, pp. 7-13, 2006.
[32] F. Chai, J. Xia, H. Gong, B. Guo, and S. Cheng, "Torque analysis of Double-Stator Permanent Magnet Synchronous for Hybrid Electric Vehicle," in *Proceedings of IEEE Vehicle Power and Propulsion Conference (VPPC)*, 2008, pp. 1-5.
[33] T. Arakawa, M. Takemoto, S. Ogasawara, K. Inoue, O. Ozaki, H. Hojo*, et al.*, "Examination of an Interior Permanent Magnet Type Axial Gap Motor for the Hybrid Electric Vehicle," *IEEE Transactions on Magnetics,* vol. 47, pp. 3602-3605, 2011.
[34] L. Yong, T. Chengde, B. Jingang, Y. Shuang, T. Weiming, and F. Weinong, "Optimization of an 80 kW Radial-Radial Flux Compound-Structure Permanent-Magnet Synchronous Machine Used for HEVs," *IEEE Transactions on Magnetics,* vol. 47, pp. 2399-2402, 2011.
[35] D. G. Dorrell, H. Min-Fu, and A. M. Knight, "Alternative Rotor Designs for High Performance Brushless Permanent Magnet Machines for Hybrid Electric Vehicles," *IEEE Transactions on Magnetics,* vol. 48, pp. 835-838, 2012.

[36] S. Schey, "Canadian EV Infrastructure Development Guideline," Ceati International Inc., Strategic Optionas for Sustainable Power Generation Interest Group (SOIG), Quebec, Canada No. T112700-0536, January 2013.
[37] M. Yilmaz and P. T. Krein, "Review of Battery Charger Topologies, Charging Power Levels, and Infrastructure for Plug-In Electric and Hybrid Vehicles," *IEEE Transactions on Power Electronics,* vol. 28, pp. 2151-2169, 2013.
[38] S. Haghbin, S. Lundmark, M. Alakula, and O. Carlson, "Grid-Connected Integrated Battery Chargers in Vehicle Applications: Review and New Solution," *IEEE Transactions on Industrial Electronics,* vol. 60, pp. 459-473, 2013.
[39] S. Lacroix, E. Laboure, and M. Hilairet, "An integrated fast battery charger for Electric Vehicle," in *Proceedings of IEEE Vehicle Power and Propulsion Conference (VPPC)*, 2010, pp. 1-6.
[40] W. E. Rippel, "Integrated traction inverter and battery charger apparatus," US 07/164,868.
[41] A. G. Cocconi, "Combined motor drive and battery recharge system," US 08/028,998.
[42] (2008). *AC Propulsion EV Drive System Specifications* [Online]. Available: http://www.acpropulsion.com/products-reductive.html
[43] F. Lacressonniere and B. Cassoret, "Converter used as a battery charger and a motor speed controller in an industrial truck," in *Proceedings of European Conference on Power Electronics and Applications*, 2005, pp. 7 pp.-P.7.
[44] S. Seung-Ki and L. Sang-Joon, "An integral battery charger for four-wheel drive electric vehicle," *IEEE Transactions on Industry Applications,* vol. 31, pp. 1096-1099, 1995.
[45] T. Lixin and S. Gui-Jia, "A low-cost, digitally-controlled charger for plug-in hybrid electric vehicles," in *Proceedings of IEEE Energy Conversion Congress and Exposition (ECCE)*, 2009, pp. 3923-3929.
[46] T. Lixin and S. Gui-Jia, "Control scheme optimization for a low-cost, digitally-controlled charger for plug-in hybrid electric vehicles," in *Proceedings of IEEE Energy Conversion Congress and Exposition (ECCE)*, 2010, pp. 3604-3610.
[47] S. Gui-Jia and T. Lixin, "Control of plug-in hybrid electric vehicles for mobile power generation and grid support applications," in *Proceedings of IEEE Applied Power Electronics Conference and Exposition (APEC)*, 2010, pp. 1152-1157.
[48] S. Gui-Jia and T. Lixin, "An integrated onboard charger and accessory power converter for plug-in electric vehicles," in *Proceedings of Energy Conversion Congress and Exposition (ECCE)*, 2013, pp. 1592-1597.
[49] Bruye, x, A. re, L. De Sousa, B. Bouchez, P. Sandulescu, *et al.*, "A multiphase traction/fast-battery-charger drive for electric or plug-in hybrid vehicles: Solutions for control in traction mode," in *Proceedings of IEEE Vehicle Power and Propulsion Conference (VPPC)*, 2010, pp. 1-7.
[50] L. De Sousa, B. Silvestre, and B. Bouchez, "A combined multiphase electric drive and fast battery charger for Electric Vehicles," in *Proceedings of IEEE Vehicle Power and Propulsion Conference (VPPC)*, 2010, pp. 1-6.
[51] L. De Sousa and B. Bouchez, "Combined electric device for powering and charging," ed: Google Patents, 2011.
[52] L. De Sousa and B. Bouchez, "Method and electric combined device for powering and charging with compensation means," US 13/128,925, Jan 26, 2012.
[53] A. P. Sandulescu, F. Meinguet, X. Kestelyn, E. Semail, and A. Bruyere, "Flux-weakening operation of open-end winding drive integrating a cost-effective high-power charger," *IET Jounal on Electrical Systems in Transportation,* vol. 3, pp. 10-21, 2013.
[54] S. Haghbin, T. Thiringer, and O. Carlson, "An integrated split-phase dual-inverter permanent magnet motor drive and battery charger for grid-connected electric or hybrid vehicles," in *Proceedings of IEEE International Conference on Electrical Machines (ICEM)*, 2012, pp. 1941-1947.

[55] S. Haghbin, K. Khan, Z. Shuang, M. Alakula, S. Lundmark, and O. Carlson, "An Integrated 20-kW Motor Drive and Isolated Battery Charger for Plug-In Vehicles," *IEEE Transactions on Power Electronics,* vol. 28, pp. 4013-4029, 2013.
[56] I. Subotic, E. Levi, M. Jones, and D. Graovac, "An integrated battery charger for EVs based on an asymmetrical six-phase machine," in *Proceedings of 39th Annual Conference of the IEEE Industrial Electronics Society (IECON)*, 2013, pp. 7244-7249.
[57] S. Haghbin, M. Alakula, K. Khan, S. Lundmark, M. Leksell, O. Wallmark*, et al.*, "An integrated charger for plug-in hybrid electric vehicles based on a special interior permanent magnet motor," in *Proceedings of IEEE Vehicle Power and Propulsion Conference (VPPC)*, 2010, pp. 1-6.
[58] S. Haghbin, S. Lundmark, M. Alakula, and O. Carlson, "An Isolated High-Power Integrated Charger in Electrified-Vehicle Applications," *IEEE Transactions on Vehicular Technology,* vol. 60, pp. 4115-4126, 2011.
[59] S. Haghbin, S. Lundmark, O. Carlson, and M. Alakula, "A combined motor/drive/battery charger based on a split-windings PMSM," in *Proceedings of IEEE Vehicle Power and Propulsion Conference (VPPC)*, 2011, pp. 1-6.
[60] K. Kurihara, "Effects of Damper Bars on Steady-State and Transient Performance of Interior Permanent-Magnet Synchronous Generators," *IEEE Transactions on Industry Applications,* vol. 49, pp. 42-49, 2013.
[61] T. Hosoi, H. Watanabe, K. Shima, T. Fukami, R. Hanaoka, and S. Takata, "Demagnetization Analysis of Additional Permanent Magnets in Salient-Pole Synchronous Machines With Damper Bars Under Sudden Short Circuits," *IEEE Transactions on Industrial Electronics,* vol. 59, pp. 2448-2456, 2012.
[62] T. A. Burress, S. L. Campbell, C. L. Coomer, C. W. Ayers, A. A. Wereszczak, J. P. Cunningham*, et al.*, "Evaluation of The 2010 Toyota Prius Hybrid Synergy Drive System," Oak Ridge National Laboratory, Washington D.C. , USA, 2011.
[63] L. Xiaomin, K. L. V. Iyer, and N. C. Kar, "Mathematical modeling and comprehensive analysis of induction assisted permanent magnet synchronous AC motor," in *Electric Drives Production Conference (EDPC), 2011 1st International*, 2011, pp. 147-152.
[64] K. L. V. Iyer, L. Xiaomin, K. Mukherjee, and N. C. Kar, "A Novel Two-Axis Theory-Based Approach Towards Parameter Determination of Line-Start Permanent Magnet Synchronous Machines," *IEEE Transactions on Magnetics,* vol. 48, pp. 4208-4211, 2012.
[65] L. Xiaomin, K. L. V. Iyer, K. Mukherjee, and N. C. Kar, "A Novel Two-Axis Theory-Based Experimental Approach Towards Determination of Magnetization Characteristics of Line-Start Permanent Magnet Synchronous Machines," *IEEE Transactions on Magnetics,* vol. 49, pp. 4733-4737, 2013.
[66] K. Mukherjee, K. L. V. Iyer, L. Xiaomin, and N. C. Kar, "A Novel and Fundamental Approach Toward Field and Damper Circuit Parameter Determination of Synchronous Machine," *IEEE Transactions on Industry Applications,* vol. 49, pp. 2097-2105, 2013.
[67] K. Mukherjee, K. L. V. Iyer, L. Xiaomin, and N. C. Kar, "A novel and fundamental approach towards field and damper circuit parameter determination of synchronous machine," in *Electrical Machines (ICEM), 2012 XXth International Conference on*, 2012, pp. 41-46.
[68] L. Xiaomin, K. L. V. Iyer, K. Mukherjee, and N. C. Kar, "Development of a bi-directional off-board level-3 quick charging station for electric bus," in *Proceedings of Transportation Electrification Conference and Expo (ITEC), IEEE*, 2012, pp. 1-6.
[69] L. Xiaomin, K. L. V. Iyer, K. Mukherjee, and N. C. Kar, "A Dual Purpose Triangular Neural Network Based Module for Monitoring and Protection in Bi-Directional Off-Board Level-3 Charging of EV/PHEV," *IEEE Transactions on Smart Grid,* vol. 3, pp. 1670-1678, 2012.

[70] P. Kundur, N. J. Balu, and M. G. Lauby, *Power system stability and control*. New York, USA: McGraw-Hill, 1994.
[71] P. C. Krause, O. Wasynczuk, and S. D. Sudhoff, *Analysis of Electric Machinery*. Danvers, USA: Wiley-Interscience, 1995.
[72] S. Chapman, *Electric Machinery Fundamentals*. New York, USA: McGraw-Hill Companies,Incorporated, 2005.
[73] "IEEE Standard Test Procedure for Polyphase Induction Motors and Generators," *IEEE Std 112-1996,* 1997.
[74] A. H. Isfahani and S. Vaez-Zadeh, "Effects of Magnetizing Inductance on Start-Up and Synchronization of Line-Start Permanent-Magnet Synchronous Motors," *IEEE Transactions on Magnetics,* vol. 47, pp. 823-829, 2011.
[75] C. Sen, Y. Usama, T. Carciumaru, L. Xiaomin, and N. C. Kar, "Design of a Novel Wavelet Based Transient Detection Unit for In-Vehicle Fault Determination and Hybrid Energy Storage Utilization," *IEEE Transactions on Smart Grid,* vol. 3, pp. 422-433, 2012.
[76] M. Ehsani, *Modern Electric, Hybrid Electric, And Fuel Cell Vehicles: Fundamentals, Theory, And Design*. Florida, USA: Taylor & Francis Group, 2005.
[77] B. K. Bose, *Power electronics and motor drives*. San Diego, USA: Academic Press, 1986.
[78] G. K. Dubey, *Power semiconductor controlled drives*. New Jersey, USA: Prentice Hall PTR, 1989.
[79] T. M. Hijazi and N. A. Demerdash, "Computer-aided modeling and experimental verification of the performance of power conditioner operated permanent magnet brushless DC motors including rotor damping effects," *IEEE Transactions on Energy Conversion,* vol. 3, pp. 714-721, 1988.
[80] T. M. Hijazi and N. A. Demerdash, "Impact of the addition of a rotor-mounted damper bar cage on the performance of samarium-cobalt permanent magnet brushless DC motor systems," *IEEE Transactions on Energy Conversion,* vol. 3, pp. 890-898, 1988.
[81] A. Darabi and C. Tindall, "Damper cages in genset alternators: FE simulation and measurement," *IEEE Transactions on Energy Conversion,* vol. 19, pp. 73-80, 2004.
[82] K. Kamiev, J. Nerg, and J. Pyrhonen, "Design of damper windings for direct-on-line permanent magnet synchronous generators," in *Proceedings of IEEE EUROCON*, 2009, pp. 783-790.
[83] *Toyota's Eco-Friendly Car is Here* [Online]. Available: http://www.toyota.co.jp/en/tech/environment/ths2/
[84] R. H. Staunton, C. W. Ayers, L. D. Marlino, J. N. Chiasson, and T. A. Burress, "Evaluation of 2004 Toyota Prius Hybrid Electric Drive System," Oak Ridge National Laboratory, Washington D.C., USA, 2006.
[85] N. Mohan, T. M. Undeland, and W. P. Robbins, *Power Electronics: Converters, Applications, and Design*, 3 ed. Danver, USA: John Wiley & Sons, 2003.
[86] L. Yanhe and N. C. Kar, "Advanced design approach of power split device of plug-in hybrid electric vehicles using Dynamic Programming," in *Proceedings of Vehicle Power and Propulsion Conference (VPPC), IEEE*, 2011, pp. 1-6.
[87] "IEEE Standard Service Conditions and Definitions for High-Voltage Fuses, Distribution Enclosed Single-Pole Air Switches, Fuse Disconnecting Switches, and Accessories," *IEEE Std C37.40-2003 (Revision of IEEE Std C37.40-1993),* pp. 1-34, 2004.
[88] M. K. a. N. C. Kar, "Hybrid Electric Vehicles for Sustainable Transportation: A Canadian Perspective," *World Electric Vehicle Journal,* vol. 3, 2009.
[89] K. Clement-Nyns, E. Haesen, and J. Driesen, "The Impact of Charging Plug-In Hybrid Electric Vehicles on a Residential Distribution Grid," *IEEE Transactions on Power Systems,* vol. 25, pp. 371-380, 2010.
[90] J. C. Gomez and M. M. Morcos, "Impact of EV battery chargers on the power quality of distribution systems," *IEEE Transactions on Power Delivery,* vol. 18, pp. 975-981, 2003.

[91] N. A. Ninad and L. A. C. Lopes, "Unbalanced operation of per-phase vector controlled four-leg grid forming inverter for stand-alone hybrid systems," in *Proceedings of 38th Annual Conference on IEEE Industrial Electronics Society (IECON)*, 2012, pp. 3500-3505.

[92] J. P. Gegner and C. Q. Lee, "Linear peak current mode control: a simple active power factor correction control technique for continuous conduction mode," in *Proceedings of IEEE Power Electronics Specialists Conference (PESC)*, 1996, pp. 196-202 vol.1.

[93] F. Blaschke, "The principles of field orientation as applied to the new TRANSVEKTOR closed-loop control system for rotating field machines," *Siemens Review,* pp. 217–220, 1972.

[94] R. W. Erickson and D. Maksimovic, *Fundamentals of Power Electronics*, 2 ed. New York, USA: Kluwer Academic Publishers, 2004.

[95] D. Aggeler, F. Canales, H. Zelaya-De La Parra, A. Coccia, N. Butcher, and O. Apeldoorn, "Ultra-fast DC-charge infrastructures for EV-mobility and future smart grids," in *Proceedings of Innovative Smart Grid Technologies Conference Europe (ISGT Europe)*, 2010, pp. 1-8.

[96] C. Schauder and H. Mehta, "Vector analysis and control of advanced static VAr compensators," *IEE Proceedings on Generation, Transmission and Distribution,,* vol. 140, pp. 299-306, 1993.

[97] V. Kaura and V. Blasko, "Operation of a phase locked loop system under distorted utility conditions," *IEEE Transactions on Industry Applications,* vol. 33, pp. 58-63, 1997.

[98] K. Mukherjee, K. L. V. Iyer, L. Xiaomin, and N. C. Kar, "A novel and fundamental approach towards field and damper circuit parameter determination of synchronous machine," in *Proceedings of International Conference on Electrical Machines (ICEM)*, 2012, pp. 41-46.

APPENDICES

Appendix A
Nameplate Rating of the Machines with Damper under Test

TABLE A-1. NAMEPLATE RATINGS OF MACHINE I (LSPMSM)

Hz	V	kW	A	cos θ	r/min	Nm
20	85	1.13	11.13	0.20	600	18
50	200	2.83	11.40	0.80	1500	18
100	400	5.66	11.68	0.76	3000	18

TABLE A-2. NAMEPLATE RATINGS OF THE WOUND-FIELD ROTOR SYNCHRONOUS MACHINE WITH DAMPER

r/min	Volts AC	Hz	EXCIT (V DC)
1800	120/208	60	120
kW	AMP. AC	cos φ	AMP. DC
2	11.8/6.8	1	1

Appendix B
Electrical and Mechanical Characteristics of the EV Studied

TABLE B-1. VEHICLE OVERALL AND MAJOR POWER COMPONENTS RATINGS

Vehicle Overall		
Vehicle Mass [kg]	Coefficient of Aerodynamic Drag	Frontal Area of Vehicle [m^2]
1,250	0.30	2.52
Wheel Radius [m]	Coefficient of Rolling Resistance	Air Density [kg/m^3]
0.287	0.015	1.184
ICE		
Max Power [kW]	Max torque [Nm]	Max Speed [r/min]
57 @ 4,500 r/min	111 @ 4,200 r/min	5,000
MG1		
Rated Power [kW]	Rated Torque [Nm]	Max Speed [r/min]
15	60	11,000
MG2		
Rated Power [kW]	Rated Torque [Nm]	Max Speed [r/min]
35@940 to 2,000 r/min	305 @ 0 to 940 r/min	7,000
Battery		
Voltage [V]	Capacity [Ah]	
312	13	

Appendix C
Case Study of the Traction Motor for Toyota Prius

TABLE C-1. MECHANICAL AND ELECTRICAL DATA FROM THE PRIUS PERFORMANCE-MAPPING TEST

	Mechanical Conditions		Inverter DC link side (rms)		Inverter AC side per phase (rms)	
Test #	Speed (r/min)	Torque (Nm)	Voltage (V)	Current (A)	Voltage (V)	Current (A)
1-1	304	71.0	504.0	7.70	92.0	38.5
1-2	302	179.2	504.0	21.32	108.0	87.3
1-3	297	269.7	498.1	46.72	212.3	129.8
2-1	703	30.2	504.0	6.74	112.3	20.2
2-2	700	129.6	503.8	24.29	141.3	64.4
2-3	702	228.8	500.9	47.99	220.2	110.1
3-1	1303	20.4	503.8	7.83	141.7	14.7
3-2	1303	69.6	503.7	22.47	166.1	38.2
3-3	1302	228.9	500.4	77.18	232.8	111.5
4-1	2106	20.4	504.4	11.54	177.9	14.8
4-2	2104	70.4	504.4	34.83	204.5	38.8
4-3	2105	168.2	503.8	81.51	232.0	82.5
5-1	3805	20.4	499.7	19.87	240.7	17.1
5-2	3804	49.8	499.5	45.43	236.3	44.7
5-3	3804	98.6	499.0	91.37	241.0	95.6
6-1	5006	20.2	500.0	26.43	240.8	92.3
6-2	5003	40.1	499.5	49.05	240.3	99.8
6-3	5004	59.8	499.4	73.17	239.7	113.7
7-1	6005	20.3	500.1	32.10	241.8	31.0
7-2	6005	40.1	499.7	59.79	239.6	53.9
7-3	6005	49.4	499.6	73.60	240.7	68.2

Appendix D
Machine Equivalent Circuit Parameters

TABLE D-1. PARAMETERS OF THE TOYOTA PRIUS IPMSM WITH DESIGNED DAMPER.

Parameters	r_s (Ω)	L_{ls} (mH)	L_d (mH)	L_q (mH)	λ' (Wb.t)
Values	0.0065	0.15	1.598	2.057	0.1757
Parameters	r'_{kd} (Ω)	r'_{kq} (Ω)	L'_{lkd} (mH)	L'_{lkq} (mH)	
Values	0.0195	0.005	2.1	1.6	

Appendix E
Permissions for Using Publication

RightsLink®

Home | Account Info | Help

IEEE
Requesting permission to reuse content from an IEEE publication

Title: Rule-based Control Strategy with Novel Parameters Optimization Using NSGA-II for Power Split PHEV Operation Cost Minimization
Author: Li, Y.; Lu, X.; Kar, N.C.
Publication: Vehicular Technology, IEEE Transactions on
Publisher: IEEE
Copyright © 1969, IEEE

Logged in as:
Xiaomin Lu
Account #:
3000796628
LOGOUT

Thesis / Dissertation Reuse

The IEEE does not require individuals working on a thesis to obtain a formal reuse license, however, you may print out this statement to be used as a permission grant:

Requirements to be followed when using any portion (e.g., figure, graph, table, or textual material) of an IEEE copyrighted paper in a thesis:

1) In the case of textual material (e.g., using short quotes or referring to the work within these papers) users must give full credit to the original source (author, paper, publication) followed by the IEEE copyright line © 2011 IEEE.
2) In the case of illustrations or tabular material, we require that the copyright line © [Year of original publication] IEEE appear prominently with each reprinted figure and/or table.
3) If a substantial portion of the original paper is to be used, and if you are not the senior author, also obtain the senior author's approval.

Requirements to be followed when using an entire IEEE copyrighted paper in a thesis:

1) The following IEEE copyright/ credit notice should be placed prominently in the references: © [year of original publication] IEEE. Reprinted, with permission, from [author names, paper title, IEEE publication title, and month/year of publication]
2) Only the accepted version of an IEEE copyrighted paper can be used when posting the paper or your thesis on-line.
3) In placing the thesis on the author's university website, please display the following message in a prominent place on the website: In reference to IEEE copyrighted material which is used with permission in this thesis, the IEEE does not endorse any of [university/educational entity's name goes here]'s products or services. Internal or personal use of this material is permitted. If interested in reprinting/republishing IEEE copyrighted material for advertising or promotional purposes or for creating new collective works for resale or redistribution, please go to http://www.ieee.org/publications_standards/publications/rights/rights_link.html to learn how to obtain a License from RightsLink.

If applicable, University Microfilms and/or ProQuest Library, or the Archives of Canada may supply single copies of the dissertation.

BACK | CLOSE WINDOW

VITA AUCTORIS

NAME:	Xiaomin Lu
PLACE OF BIRTH	Hainan, China
YEAR OF BIRT	1987
EDUCATION:	Sun Yat-sen University, B. Eng in Automation, Guangzhou, Guangdong, China, 2010
	University of Windsor, Ph.D. in Electrical Engineering, Windsor, Ontario, Canada, 2014